TESTING PROTOCOLS FOR GRADING INDUSTRIAL CARBON NANOTUBE MATERIALS

by

Elizabeth Anne York

A thesis submitted to the faculty of
The University of Utah
in partial fulfillment of the requirements for the degree of

Master of Science

Department of Chemical Engineering

The University of Utah

May 2015

The University of Utah Graduate School

STATEMENT OF THESIS APPROVAL

The thesis of Elizabeth Anne York has been approved by the following supervisory committee members.

_____Terry Ring_____, Chair __8/4/2014_____
Date Approved

_____Jules Magda _____, Member __8/4/2014_____
Date Approved

_____Eric Eddings _____, Member __8/4/2014_____
Date Approved

and by__Milind Deo _____, Chair of the Department of _____Chemical Engineering _____

and by David B. Kieda, Dean of The Graduate School.

ABSTRACT

Since the discovery of carbon nanotubes in the 1950s, scientists and engineers have been working on applications that utilize their unique properties. Carbon nanotubes possess extreme conductivity, strength and stiffness which can be used to provide composite materials with improved properties. Cost effective large-scale production is a major challenge for the widespread adoption of carbon nanotubes. A Utah pilot industrial plant has been built to make industrial grade carbon nanotubes. This work seeks to develop appropriate methods for this testing these industrial grade carbon nanotubes.

Carbon nanotubes can be studied using a scanning electron microscope (SEM), which is an incredibly powerful tool, however, SEM analysis struggles to provide properties that can be attributed to the bulk powder properties due to the small number observed. The carbon nanotube testing protocols developed in this thesis are devoted to bulk powder methods including: bulk, tap and particle density by helium pyncometry, Brunauer-Emmett-Teller, BET, surface area, temperature programmed oxidation to determine the oxidation temperatures of different types of carbon and the percentage of impurities after oxidation, bulk heat capacity, Raman spectroscopy and Fourier transform infrared spectroscopy, and viscosity. The results of these analytical methods are provided for various types of industrial carbon materials including carbon nanotubes. The

analytical results demonstrate that these bulk analytical methods can be used to differentiate various qualities of carbon nanotubes from other types of carbon.

Carbon nanotubes show hybridized sp^2 bonds with an open p orbital similar to that of graphene. However, the curvature of the nanotube structure allows an analytical distinction between the two using spectroscopy. This curvature and bonding gives the carbon nanotubes a higher level of structure which results in a higher temperature of oxidation, a larger specific heat capacity, and a higher surface area to volume ratio than other carbon species. Carbon nanotubes have an extremely large aspect ratio, the ratio of their length to their diameter. This will cause a unique distortion in the viscosity measurements at a particular volume fraction.

TABLE OF CONTENTS

LIST OF TABLES

LIST OF FIGURES

CHAPTER I

MATERIALS

Overview

In order to differentiate between carbon nanotubes and other highly structured carbon materials, a control group of different materials was selected. The group chosen for this study is described in this chapter.

Carbon Properties and Bonding

The carbon atom has four electrons available for bonding resulting in a full inner shell and a half full outer shell which has a ground state electron configuration of $1s^2 2s^2 2p^2$. This allows carbon to form many different covalent bonded structures. The bonding of carbon is so varied that an entire area of study is devoted to it. Besides the organic structures that are present when carbon bonds to oxygen, hydrogen, nitrogen, and many other elements, there is a unique bonding that occurs when carbon binds to itself. These carbon structures will have hybridized bonds, which create added strength to the carbon structure. The properties of these carbon allotropes depend on the unit cells that are produced when the bonds form under different circumstances. The first discovered allotropes of carbon include graphite, graphene, and diamonds. These unit cells can be seen in Figure 1.

The bond length of diamond with sp^3 hybridization type bonding is 0.154 nm. It is compared to the graphene with sp^2 hybridization bond length of 0.142 nm. The graphene bond is shorter and is also stronger because each carbon is only bonded to three other atoms and still shares all four electrons, while the diamond structure carbon atoms are bound to four other carbon atoms in a tetrahedral structure,

The sp^3 structure "mixes" an s orbital with three p orbitals to produce four bond of equal energy, strength, and distance. These bonds have 25% s character and 75% p character showing the following wave functions, where the sign changes refer to a change in phase of the wave function.

$$\psi_{sp^3 hybrid} = \frac{1}{2}\left(\psi_{2s} + \psi_{2p_x} + \psi_{2p_y} + \psi_{2p_z}\right) = \frac{1}{2}\left(\psi_{2s} + \psi_{2p_x} - \psi_{2p_y} - \psi_{2p_z}\right) \quad (1.1)$$

$$= \frac{1}{2}\left(\psi_{2s} - \psi_{2p_x} + \psi_{2p_y} - \psi_{2p_z}\right) = \frac{1}{2}\left(\psi_{2s} - \psi_{2p_x} - \psi_{2p_y} + \psi_{2p_z}\right)$$

Since the carbon atom has four free electrons, each electron from one carbon atom can pair with an electron from a neighboring carbon atom in a tetrahedral structure. This creates an electronically stable unit cell which explains why the diamond allotrope of carbon is stable and does not seek interactions with other species.

Alternatively the sp^2 bonding shown in the graphene unit cell leaves an unmixed p orbital. This is seen in Figure 2, which shows the ethene molecule that has similar C-C bonding seen in the graphene unit cell. This shows the three equal bond that the carbon atom is making, two with hydrogen and one with the other carbon atom. This allows for three of the free electrons to be occupied with bonds. These bonds have 33% s characteristic and 67% p characteristic, which results in the following wave functions.

$$\psi_{sp^2 hybrid} = \frac{1}{\sqrt{3}}\psi_{2s} + \frac{2}{\sqrt{3}}\psi_{2p_x} = \frac{1}{\sqrt{3}}\psi_{2s} - \frac{1}{\sqrt{6}}\psi_{2p_x} + \frac{1}{\sqrt{2}}\psi_{2p_y}$$
$$= \frac{1}{\sqrt{3}}\psi_{2s} - \frac{1}{\sqrt{6}}\psi_{2p_x} - \frac{1}{\sqrt{2}}\psi_{2p_y} \quad (1.2)$$

This bonding structure is planar, which is why the graphene allotrope forms sheets. The fourth electron will occupy the unhybridized p orbital, as seen on the right in Figure 2. This extra p orbital sticks out of the plane of the atoms. In ethene these electrons find each other to form a π bond that branches above and below the σ bond. In graphene, there are not just two carbon atoms with these half-filled p orbitals, there are a whole network along the plane. These electrons are free to move along the plane, which explains the high electrical conductivity of graphene sheets. The electrons can move above or below the plane of C atoms. Graphite also takes advantage of this property by forming bonds between graphene sheets. So the graphite bonding will sandwich the p orbitals with the carbon atom planes. The distance between these planes measures 0.335 nm, almost twice the distance of the carbon bonds within the graphene sheet. This is due to the lack of s character in these bonds. As these sheets stack together, electrons and phonons can move along the sheets easily and between the sheets with some added difficulty. This material will show added stability.

In 1985 at Rice University Richard Smalley and others discovered a new carbon allotrope group they called fullerenes, the first being buckminsterfullerene, which is a 60 atom allotrope that forms a sphere (see Figure 3). This study led to the discovery of carbon nanotubes. The bonding structure of these carbon species is the same sp^2 hybridization as graphene, with the multiwalled tubes behaving with a graphitic nature by layering the graphene tubes.

The single walled nanotubes (SWNT) can have three different structures: armchair, zigzag, or chiral. These differences are typically described by rolling a graphene sheet in three different ways. Figure 4 shows how the axis by which the graphene sheet is rolled will give the different types that determines their electronic behavior. The armchair variety occur when the bonds are connected from (0,0) to around (11,9), following the dotted line in Figure 4. These tubes exhibit no band gap, making them very conductive. As the rolling axis moves to connecting (0.0) to (11,7) the carbon nanotubes become chiral. This increases the band gap to 1.7 eV, which allows these nanotubes to behave as semiconductors. As the chiral angle, marked as ϕ in Figure 4, increases to 30° the zigzag variety is formed. These possess an even larger band gap of 1.9 eV, which is 70% larger than the band gap of silicon.

Since their discovery, much research has been performed to explore and quantify the properties that these unique bonding structures possess. The following work will investigate methods to determine impurities and classify nanotube fullerenes made through an industrial process in a bulk sample.

Laboratory Carbon Allotropes

For this work the control species are carbon allotropes that have been grown on a small scale in a laboratory. The SEM images in Figure 5 show a high grade graphene sheet grown on a SiO_2/Si substrate, and a natural graphite sample. The sheets of graphene can be seen as scales on the graphite sample.

The initial studies of carbon nanotubes began by growing them in a very controlled manner. Four different methods arose, arc discharge synthesis, laser abalation,

plasma torch, and chemical vapor deposition. Early arc discharge synthesis used two graphitic rods that were charged in an inert gas. As they moved closer together there was an arc that formed and produced a plasma. The CNT material is then deposited on to one of the rods. [11] More recently catalysts are used with reactive gases to facilitate the growth. An image of the tubes that are made through this process in a laboratory are shown here. [12] As in Figure 6, this process can produce single and double walled tubes with little catalyst residue.

A laser ablation process was developed to increase the carbon consumption. In this process, a quartz reactor is heated to 1200 °C and a laser is pulsed onto the catalytic material and graphite powder simultaneously. [13] As with the arc discharge synthesis, there is a high purity and multiwalled tubes with few layers that are produced in this process.

Looking for a method to produce high purity macroscopic strands directly, Chen et al. have developed a method using a plasma torch at atmospheric pressure to produce nanotubes. In this process a stream of carbon monoxide was passed over an iron carbide to produce an iron carbonyl that was then sent through a microwave generated argon plasma. [14] The CNT material seen in Figure 7 was made. Here bundles of SWNT are made with threads of smaller tubes wrapped around each other bound by van der Waals interactions.

As progress was made on purity and carbon consumptions with the previously discused methods, all of these processes are difficult to implement in a large scale. An alternative method called chemical vapor deposition has the most promise for an industrial synthesis of CNT material. This method uses a carbon-rich feed gas which

passes over a transition metal based catalyst at a high temperature. This method can be controlled by catalyst development, conditions of the reactor, and feed stock. In a laboratory this process is controlled and gives way to the growth of MWNT and SWNT (see Figure 7). This growth is commonly known in literature as forest growth.

Industrial Carbon Allotropes

As these species are produced on a large scale in a process that is suitable for industry there are inevitable changes that occur. The first and foremost being the impurities in the sample. As a sample is taken from a reactor, the catalyst will remain with the sample unless there is a purification process. The catalyst remaining is not the only impurity. As the process moves to industrial equipment stray pieces of insulation and welding debris will inevitably end up in the sample. Also, in a high temperature process with a catalyst and using feed gases that cannot be 100% pure, there are many undesirable side reactions that occur in the reactor, as well as reactions that occur in other parts of the process which are not held at the same conditions. These reactions will produce various carbon allotropes along with hydrocarbons, carbides, etc.

The following industrial samples can be compared to the ideal laboratory samples. The graphene images in Figure 8 show sheets that are very thin, shown as white lines on the right figure, along with larger structures. The thicker sections are likely graphite sheets that are formed due to the free electrons in the p orbitals of the graphene sheet. The industrial graphite samples shown in Figure 9 are relatively large sheets. These images show the scales that are broken sheets of graphene layers. The brighter spots on the SEM images show areas of higher density. These spots are likely remnants of

catalyst particles or other impurities.

Industrial SWNT are likely to be larger than the ideal laboratory tubes and will contain bundles and multiwalled growth, see Figure 10. This is due partially to the chaos that occurs in an industrial reactor, and also to single walled nanotubes forming bundles due to van der Waals forces. The images from high purity industrial SWNT samples are seen to have tubular structures as large as 94 nm, whereas the diameter for these species are 1 nm. This confirms the conclusion of multiwalled structures being present as well and is inevitable due to the growth mechanism of the tubes.

Multiwalled nanotubes, in Figure 11, are seen as these clouds forming around the catalyst. It should be noticed that the nanotubes are not the straight soldiers that are seen in the CVD laboratory samples. They twist and turn due to bonding impurities and defects in the walls. You can also see that the diameters and the lengths, thus the aspect ratios, are highly variable. The catalysts are again seen as bright spots on the SEM images.

A fifth industrial sample that will be used in this study, due to its availability and structural differences from the other carbon allotropes is petroleum coke, pet coke, shown in Figure 12. Pet coke is an industrial by product from the cracking of heavy hydrocarbons to lighter species. There are many different grades of pet coke, but all have a very high carbon content. Pet coke is a disorganized allotrope that has no repeated unit cell and is amorphous in structure. The carbon bonding in these samples will range over an entire spectra which will allow a comparison for these testing methods.

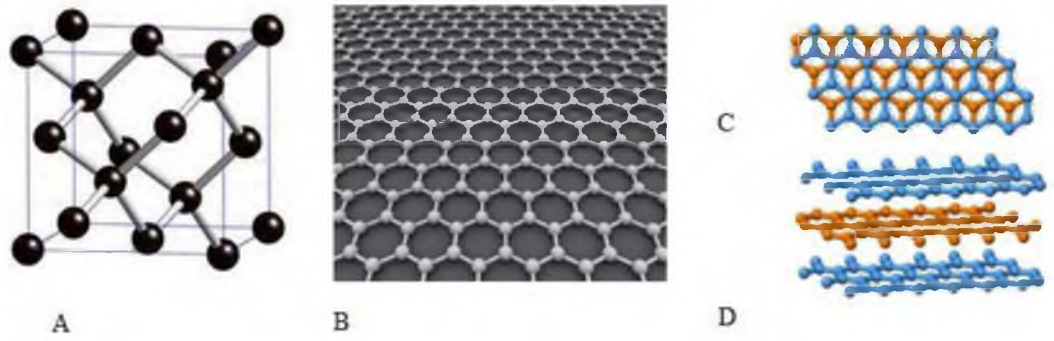

Figure 1: Different bonding structures of carbon. A) Diamond bonding (modified from ref. 1). B) Graphene sheet (modified from ref. 2). C) Graphite sheet (modified from ref. 3). D) Stacking of graphene sheets to form graphite (modified from ref. 4).

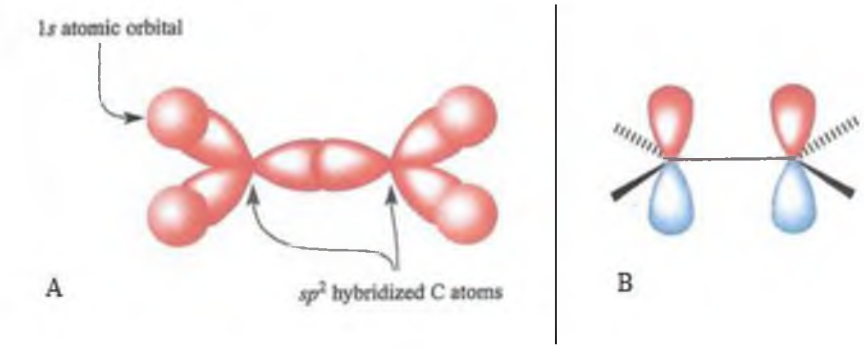

Figure 2: sp^2 carbon bonding. A) Hybridization in the plane of the molecules. B) The free p orbitals that are perpendicular to the plane of the molecules. (Modified from ref. 5.)

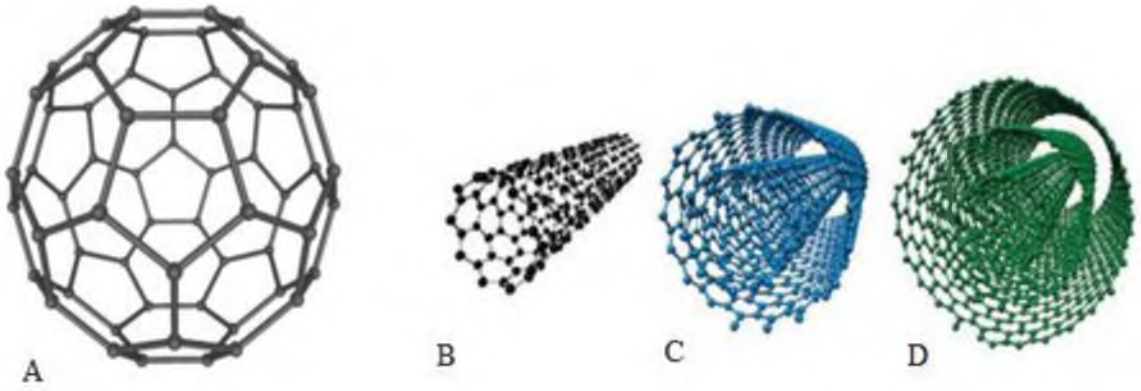

Figure 3: Models of different carbon allotropes. A) Buckminsterfullerene (modified from ref. 6). B) Single walled carbon nanotube (modified from ref. 7). C) Double walled carbon nanotube (modified from ref. 7). D) Multiwalled carbon nanotube (modified from ref. 7).

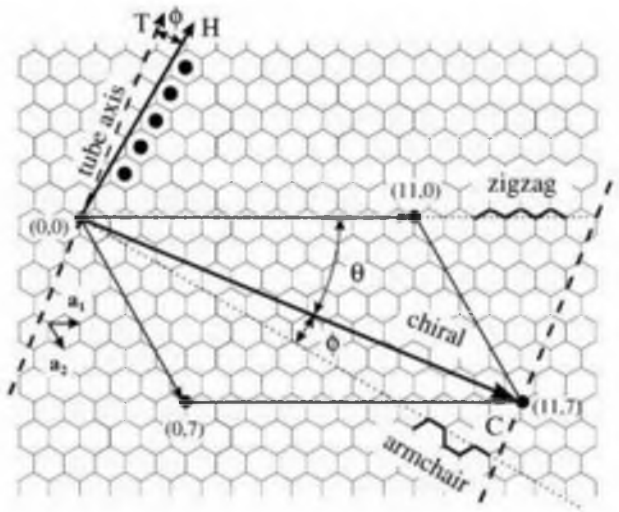

Figure 4: A pictorial explanation of the different types of single walled carbon nanotubes. The rolling axes of the zigzag, chiral, and armchair are shown by the arrows (modified from ref. 8).

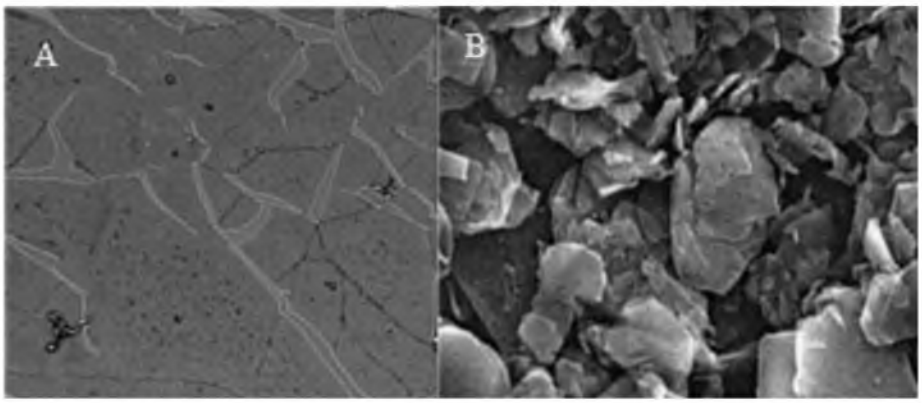

Figure 5: SEM images of graphene and graphite. A) A graphene sample (modified from ref. 9). B) A natural graphite sample (modified from ref. 10).

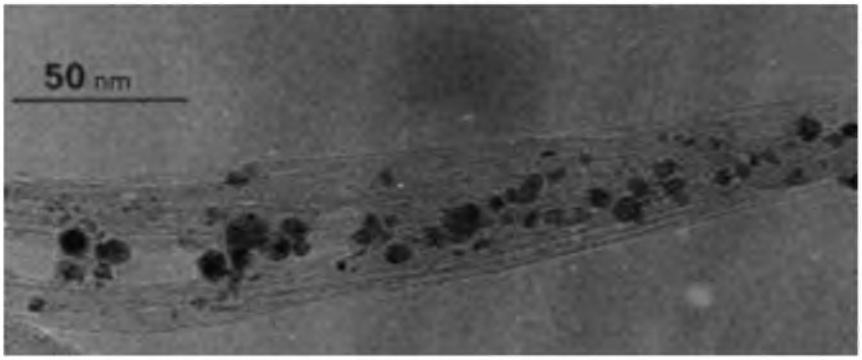

Figure 6: SEM image of multiwalled carbon nanotubes formed by the arc discharge method (modified from ref. 12).

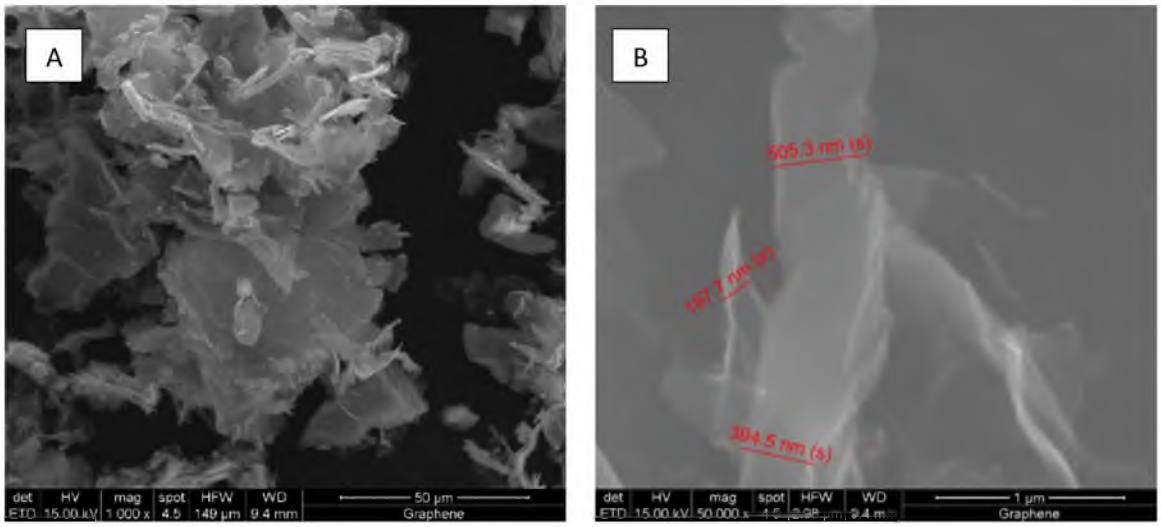

Figure 7: SEM images of industrial grade graphene taken at the University of Utah Nanolab. A) 1000 X magnification. B) 50,000 X magnification.

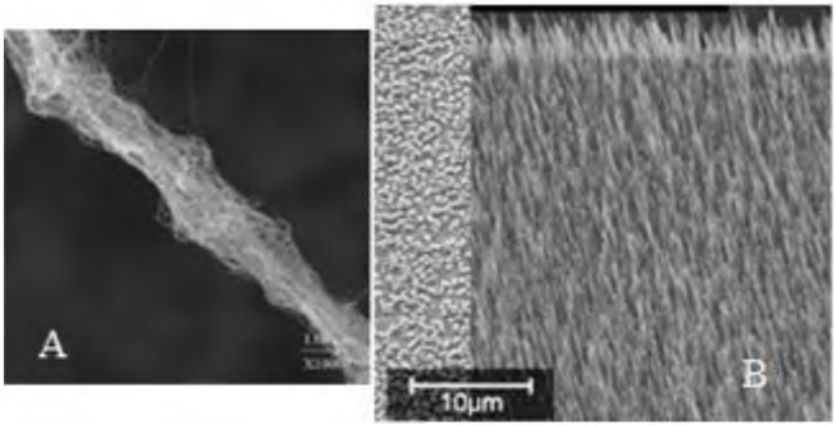

Figure 8: SEM images of laboratory grown carbon nanotube. A) A sample made through the plasma torch method, modified from ref. 13. B) Forest growth through chemical vapor deposition (modified from ref. 14.)

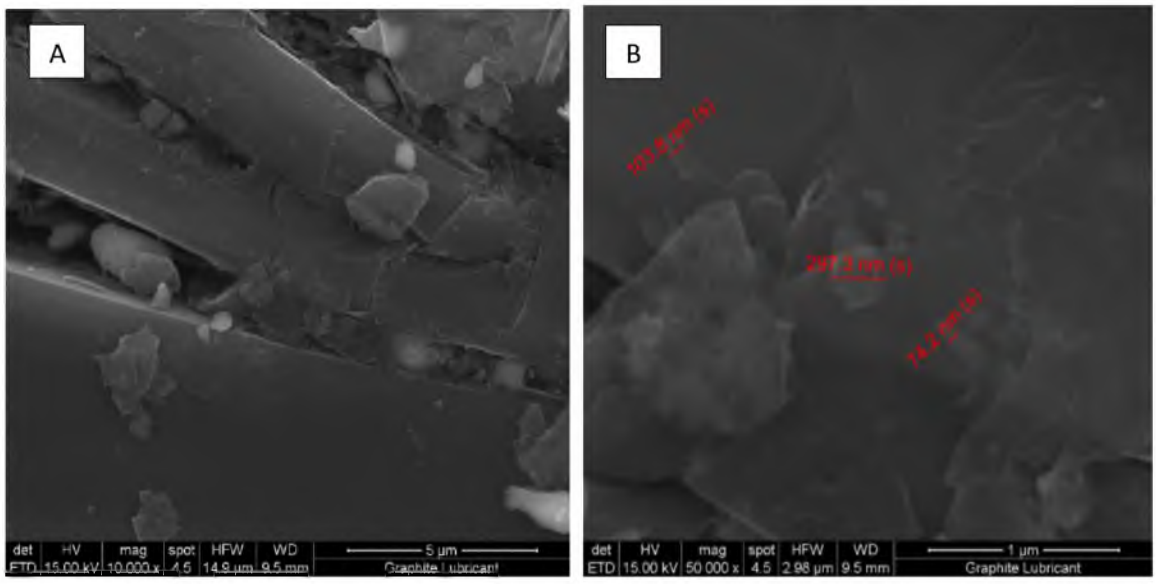

Figure 9: SEM images of industrial graphite lubricant taken at the University of Utah Nanolab. A) 10,000 X magnification. B) 50,000 X magnification.

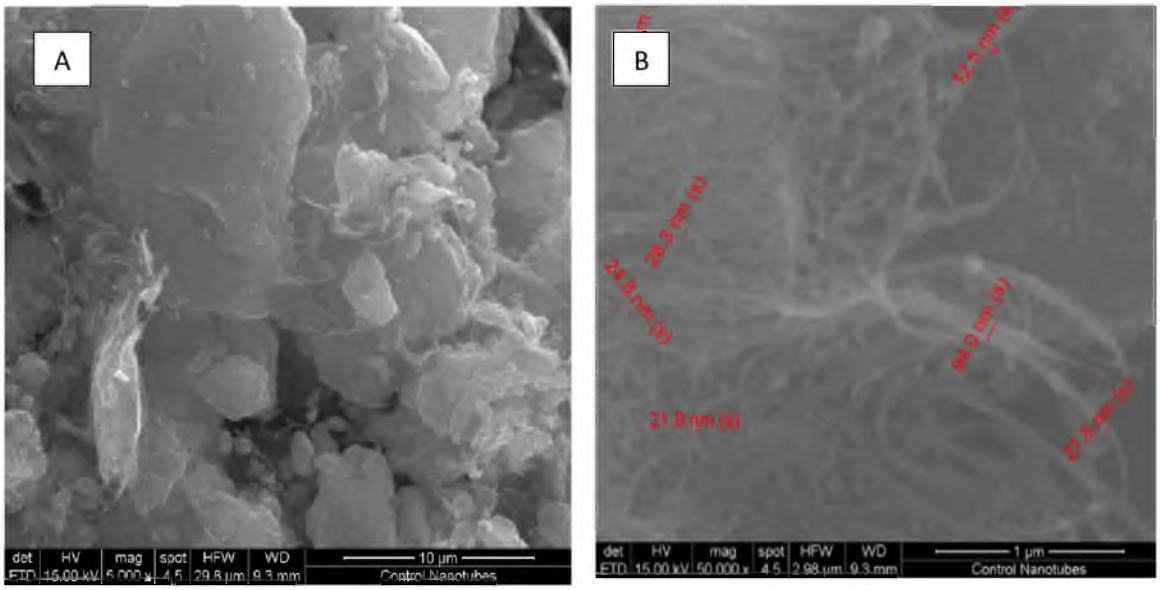

Figure 10: SEM images of industrial single and double walled carbon nanotubes obtained from cheaptubes.com, images taken at University of Utah Nanolab. A) 5000 X magnification. B) 50,000 X magnification.

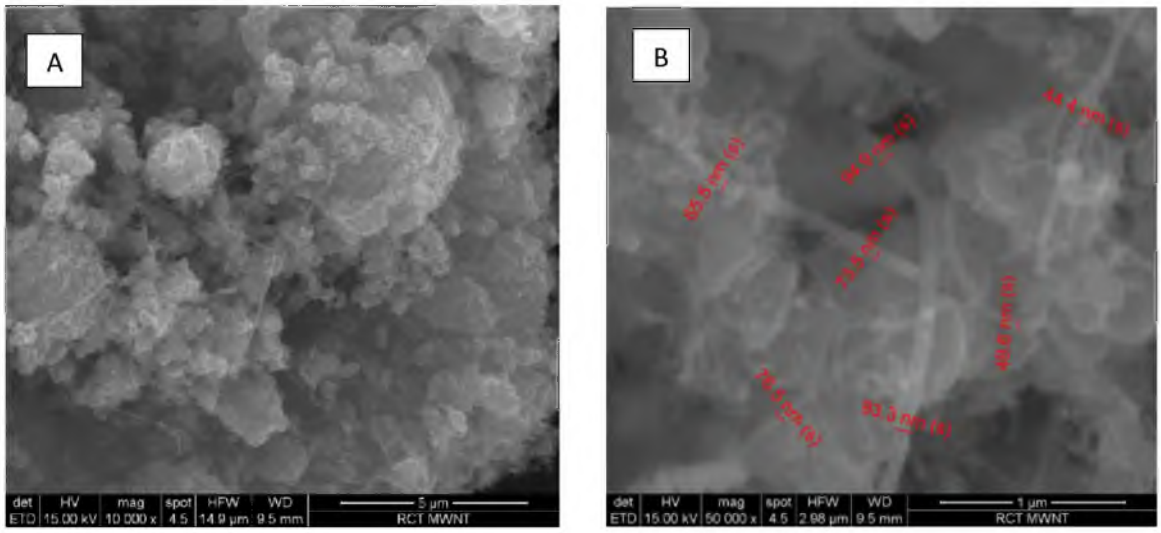

Figure 11: SEM images of industrial grade multiwalled carbon nanotubes obtained from REX, images produced at the University of Utah Nanolab. A) 10,000 X magnification. B) 50,000 X magnification.

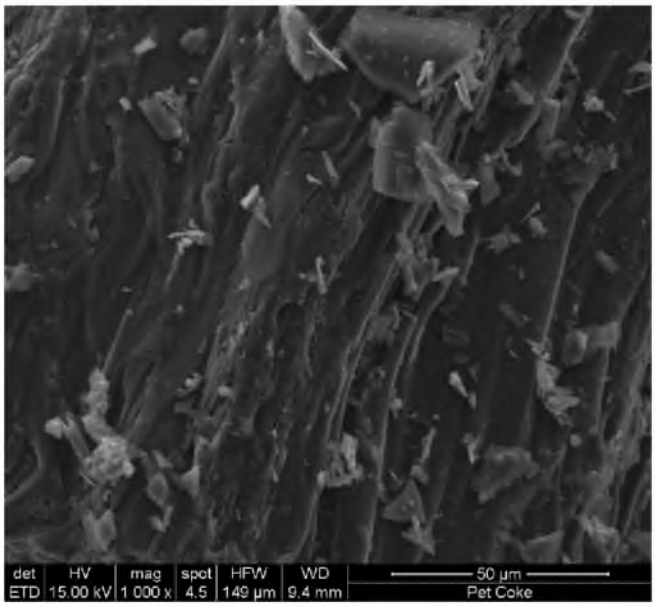

Figure 12: SEM image of pet coke taken at the University of Utah Nanolab, magnified 1000 X.

References

[1] American Physical Society, "Diamond planets are a girls' best friend," 2014. [Online]. Available: http://physicscentral.com/explore/action/diamond.cfm. [Accessed 4, December 2014]

[2] AlexanderAIUS, "Wikipedia: The Free Encyclopedia," 26 August 2010. [Online]. Available: http://en.wikipedia.org/wiki/File:Graphen.jpg. [Accessed 6 March 2014].

[3] Benjah-bmm27, "Wikipedia: The Free Encyclopedia," 19 May 2007. [Online]. Available: http://en.wikipedia.org/wiki/File:Graphite-layers-side-3D-balls.png. [Accessed 6 March 2014].

[4] Benjah-bmm27, "Wikipedia: The Free Encyclopedia," 19 May 2007. [Online]. Available: http://en.wikipedia.org/wiki/File:Graphite-layers-top-3D-balls.png. [Accessed 6 March 2014].

[5] C. E. H. A. A. G. Sharpe, Inorganic Chemistry, Essex: Pearson Education Limited, 2008.

[6] Soroush83, "Wikipedia: The Free Encyclopedia," 21 July 2007. [Online]. Available: http://en.wikipedia.org/wiki/File:C60a.png. [Accessed 6 March 2014].

[7] B. Dumé, "Scientists delve deeper into carbon nanotubes," Physics World, 19 February 2013. [Online]. Available: http://physicsworld.com/cws/article/news/2013/feb/19/scientists-delve-deeper-into-carbon-nanotubes. [Accessed 6 March 2014].

[8] J. Xie and J. P. Spallas, "Different Contrast Mechanisms in SEM Imaging of Graphene," Agilent Technologies, USA, 2012.

[9] T. Ong and H. Yang, "Effect of atmosphere on the mechanical milling of natural graphite," *Carbon,* vol. 38, p. 2077–2085, 2000.

[10] T. W. Ebbesen and P. M. Ajayan, "Large-scale synthesis of carbon nanotubes," *Nature,* vol. 358, pp. 220-222, 1992.

[11] J. Hutchisona, N. Kiselevb, E. Krinichnayac, A. Krestininc, R. Loutfyd, A. Morawsky, V. Muradyan, E. Obraztsova, J. Sloan, S. Terekhov and D. Zakharov, "Double-walled carbon nanotubes fabricated by a hydrogen arc discharge method," *Carbon,* vol. 39, pp. 761-770, 2001.

[12] M. Yudasaka, T. Komatsu, T. Ichihashi and S. Iijima, "Single-wall carbon nanotube formation by laser ablation using double-targets of carbon and metal," *Chemical Physics Letters,* vol. 278, pp. 102-106, 1997.

[13] C.-K. Chen, W. L. Perry, H. Xu, Y. Jiang and J. Phillips, "Plasma torch production of macroscopic carbon nanotube structures," *Carbon,* vol. 41, pp. 2555-2560, 2003.

[14] M. Chhowalla, K. B. K. Teo, C. Ducati, N. L. Rupesinghe and G. A. J. Amaratunga, "Growth process conditions of vertically aligned carbon nanotubes using plasma enhanced chemical vapor deposition," *Journal of Applied Physics,* vol. 90, no. 10, pp. 5308-5317, 2001.

[15] J. W. G. Wildoer, L. C. Venema, A. G. Rinzler, R. E. Smalley and C. Dekker, "Electronic structure of atomically resolved carbon nanotubes," *Nature,* vol. 391, pp. 59-62, 1 October 1998.

CHAPTER II

DENSITY AND SURFACE AREA

Density Overview

The density of a powder is an elementary property of the amount a substance weighs in proportion to its volume. This is essential in analysis of bulk behavior. In industrial samples all products should be viewed as mixtures of the desired and the undesired. Along with the carbon nanotubes, unreacted catalyst and by products will be included in the sample. For industrial samples there are three important densities that are measured, bulk, tap, and skeletal. Bulk density, also known as pour density, tells us how it will behave as it is coming out of the reactor. Tap density uses a designated pressure to tap down the powder which packs the particles closer together removing some air in the volume measured. Skeletal density is the density of the powder alone using specialized equipment.

Density Method

Bulk density is measured by pouring the powder into a known volume and measuring the weight. The accuracy and precision of this measurement can be altered by the operator. A Scott volumeter can be used to get a more accurate and consistent measurement, but this property is typically given an error to describe the inaccuracies.

These tests are done in accordance with ASTM C838: Standard Test Method for Bulk Density of As-Manufactured CNT Powder. For this report, the bulk densities were measured simply using a graduated cylinder and measuring 8 mL of dried powder.

The tap density measures a compressed density. To avoid operator discrepancies an Quantachrome Instruments Autotap is used for this measurement and performs 1000 taps to the powder in the cylinder. The final volume is then recorded. With the bulk density known the Carr's index (also known as the compressibility index or CI) and the Hausner ratio, HR, can be found using the two following equations, where ρ_t is the tapped density and ρ_b is the bulk denstiy.

$$CI = 100 * \frac{\rho_t - \rho_b}{\rho_t} \tag{2.1}$$

$$HR = \frac{\rho_t}{\rho_b} \tag{2.2}$$

Skeletal density is measured using a helium pyncometer. Pyncometers work by using the relationship of pressure to measure the volume displaced by the solid sample. Two containers are connected through a valve. The gas, helium, fills one container and the pressure is measured. Then the valve is opened allowing the gas to settle in both volumes and the pressure is measured again. Assuming there is no change in the number of moles, no adsorption, and the process is isothermal at moderate temperature, the following equation is true

$$P_1 V_1 = P_2 V_2 \tag{2.3}$$

where $P_1$is the initial pressure in V_1 the initial volume and P_2 is the final pressure when the gas has settled into the larger volume V_2. Notice that since

$$V_2 = V_1 + V_s + V_c \tag{2.4}$$

where V_s is the volume of the sample and V_c is a known control volume of the container that holds the sample. This can be rearranged such that

$$V_s = V_c + \frac{V_1}{1 - \frac{P_1}{P_2}} \quad (2.5)$$

By measuring the mass and dividing that by the volume you can find the density. [1] For this measurement, the lab uses the Accupync II 1340 by Micromeritics. This is an automated system that uses helium. The internal pressure used for these samples is 19.5 psig and this test uses approximately 1 gm of the bulk sample.

Density Results

The results of these tests are summarized in Table 1. The samples labeled C are samples from the production plant, and the Rex MWNT are nanotubes from another vendor. The bulk density measurement shows that the production samples are larger than the purchased but consistent to each other. The pet coke is the most dense of the samples in the bulk and tap test. The graphene shows the highest compressibility in the CI and HR measurements although all samples are similar. The skeletal density measurements show that the carbon nanotubes produced by the plant have this highest skeletal density. The pet coke also has a high skeletal density but a comparison of the skeletal density to the tap density shows that the sample packs closely and has uniform spherical shapes. The production samples show a large increase in density when using pyncometry. This tells us that the packing of loose powder leaves many pockets of air. This is attributed to the empty centers of the carbon nanotubes.

Surface Area Overview

Along with density the surface area of powders it is important to learn how they will behave, especially in the presence of gas adsorption and chemical reactions. Unlike a solid geometry the surface area of powders includes measuring around pores of various sizes. Like the skeletal density measurements, gas is used to find this value.

Surface Area Method

The surface area is found by adsorbing a gas, in this case nitrogen, onto the surface of the powder. There are two pieces of information needed to find the surface area. One is the number of gas molecules that adhere to the surface of the powder to cover the surface. The second is the cross-sectional area of the gas adsorbed.

To describe the number of molecules needed for the monolayer, a kinetic theory of adsorption is used, in particular the Brunauer, Emmett and Teller (BET) theory. This theory states that at equilibrium the number of molecules adsorbed to the surface of the solid will equal the amount of molecules desorbed from that same surface. However, unlike the earlier Langmuir theory, BET theory recognizes that with nonflat surfaces and nonhomogenous materials there are going to be sites that the gas prefer. This means there may be areas that are covered with more than one molecule before other areas have a monolayer. BET states that each layer will be in equilibrium with the layer above it, with the top layer being in equilibrium with the bulk fluid. The number of layers on any given site may not be uniform over the surface of the molecule, but the number of molecules in each layer will be in equilibrium.

The basic Langmuir equation is used to describe the first layer of molecules

shown below.

$$N_m\theta_1\nu_1 e^{-E_1/RT} = kP\theta_0 A_1 \quad (2.6)$$

The left hand side is the rate of desorption. N_m is the number of gas molecules adsorbed on the monolayer, θ_1 is the fraction of the surface occupied by said molecules, ν_1 is the frequency that the surface vibrates normal to the gas adsorbed, and $e^{-E_1/RT}$ is how likely the gas molecule will have enough energy to leave the surface. The right hand side is the rate of adsorption. The variable k the rate of adsorption that is dependent on the temperature, pressure, size of the gas particle, P is the pressure of the gas, θ_0 is the fraction of the unoccupied sites on the surface, and A_1 is the probability of adsorption in event of a collision between the gas and the solid. This same equation can be adapted to the nth layer of gas molecules.

$$N_m\theta_n\nu e^{-L/RT} = kP\theta_{n-1}A \quad (2.7)$$

The vibrational frequency,ν, and the probability of adsorbption, A, are assumed constant for the subsequent layers. Also the energy of desorption, E_1, is replaces by the heat of liquification. L.

These equations allow for a constant relationship between θ_n and θ_{n-1} with slight differences for the first layer.

$$\frac{\theta_1}{\theta_0} = \frac{kPA_1}{N_m\nu_1 e^{-E_1/RT}} = \alpha \quad (2.8)$$

$$\frac{\theta_n}{\theta_{n-1}} = \frac{kPA}{N_m\nu e^{-L/RT}} = \beta \quad (2.9)$$

Then recognizing that two constants are always proportional to each other and that the summation of the fraction of sites is unity, the number of molecules at equilibrium, N, can be written as:

(2.10)

$$\frac{N}{N_m} = \frac{C\beta}{(1-\beta)(1-\beta+C\beta)}$$

In this equation C is the proportionality constant relating α and β. Looking at this equation it becomes apparent that when $\beta = 1, \frac{N}{N_m} = \infty$. This can only occur when the surface is completely saturated. This would occur when the pressure is increased until it reaches a saturation pressure labeled, P_0.

$$\frac{N}{N_m} = \frac{C\left(\frac{P}{P_0}\right)}{(1-\left(\frac{P}{P_0}\right))(1-\left(\frac{P}{P_0}\right)+C\left(\frac{P}{P_0}\right))} \tag{2.11}$$

Relating the number of molecules to the weight of the adsorbed molecules and rearranging the equation we have the final form of the BET equation. [1]

$$\frac{1}{W\left[\left(\frac{P}{P_0}\right)-1\right]} = \frac{1}{W_m C} + \left(\frac{C-1}{W_m C}\right)\left(\frac{P}{P_0}\right) \tag{2.12}$$

If we find the value for the weight of the monolayer, W_m, and the cross sectional area of the gas, A_x, then

$$SA = W_m A_x \frac{\bar{N}}{\bar{M}} \tag{2.13}$$

where $\bar{N}$ is Avogadro's number and $\bar{M}$ is the molecular weight of the gas. To find W_m plot of $\frac{1}{W\left[\left(\frac{P}{P_0}\right)-1\right]}$ versus $\left(\frac{P}{P_0}\right)$ is used. This will give a linear graph with the slope and intercept of

$$m = \left(\frac{C-1}{W_m C}\right) \tag{2.14}$$

$$b = \frac{1}{W_m C} \tag{2.15}$$

Such that

(2.16)

$$W_m = \frac{1}{m + b}$$

In practice this process is automated with the ASAP 2020 from Micromeritics. For these measurements the gas chosen is nitrogen in accordance with ASTM D6556.

Surface Area Results

The results for the samples tested are shown in Table 2. This table shows that the carbon nanotube samples have a much higher surface area than any other samples tested. The pet coke shows the lowest surface area per gram. This correlates well with the spherical structure. The graphene has an increased surface area indicating the sheet like structure of the graphene molecules.

Conclusions

The surface area and density measurements allow for bulk testing that can indicate the presences of nanotubes in the sample. A ratio of the tap density and the skeletal density is large then there is a large void fraction in the powder sample. If we compare the skeletal densities of graphite and diamond there is a difference of 1.25 g/mL. The sp^3 bonding of diamond allows for the carbon atoms to pack closer together than the sp^2 bonding in graphite. The graphene skeletal density is even smaller, 2.72 g/mL less than diamond, showing the lack of bonding between sheets. The carbon nanotubes show a density that is intermediate to these values which can be related to a combination of sp^2 and sp^3 bonds.

The surface area to volume ratio can theoretically provide the radius of the carbon material. However, the structure of the sample must be assumed. If we look at the ratio of the surface area to volume for spheres and open ended cylinders we see that:

$$\frac{SA_{sphere}}{V_{sphere}} = \frac{4\pi r^2}{\frac{4}{3}\pi r^3} = \frac{3}{r} \tag{2.17}$$

$$\frac{SA_{cyl}}{V_{cyl}} = \frac{2\pi rL}{\pi r^2 L} = \frac{2}{r} \tag{2.18}$$

Figure 13 shows a graph of these equations using radii that range from 1 to 10 nm. From the inverse ratio, graphed in Figure 14, it is seen that a volume to surface area ratio of 2 nm would correspond to a 4 nm radius cylinder or a 6 nm radius sphere. A cylinder with the same radius as a sphere in a laboratory setting is likely to show the same surface area to volume measurement. By itself the surface area can indicate the size of the molecule but cannot discriminate the shape. If we also take our data and divide the surface area found with the BET analysis and divide by the skeletal density, the carbon nanotube samples show a value between 60 and 90 m^2/mL (see Table 3).

Table 1: Different density measurements of various samples.

	Bulk Den.	**Tap Den.**	**Carr's Index, CI**	**Hausner Ratio, HR**	**Skel. Den.**
	g/ml	g/ml			g/ml
Rex MWNT	0.09	0.13	31%	1.44	0.84
Graphene	0.08	0.14	43%	1.75	0.80
Pet Coke	0.70	1.09	36%	1.56	1.73
C-001	0.17	0.23	26%	1.35	2.25
C-002	0.27	0.40	33%	1.48	1.97
C-003	0.28	0.38	26%	1.36	1.81
Amorphous C [2]					1.95
Diamond [2]					3.51
Graphite [2]					2.27
SW/DW/MWNT [3]					2.1

Table 2: Surface area analysis for various samples.

	Instrument BET SA
	m^2/g
Rex MWNT	65.39
Graphene	15.85
Pet Coke	2.42
C-001	87.18
C-002	111.76
C-003	163.69

Table 3: The ratio of surface area to volume using the density measurement.

	SA/V
	m^2/mL
Rex MWNT	77.85
Graphene	19.81
Pet Coke	1.40
C-002	56.73
C-003	90.44

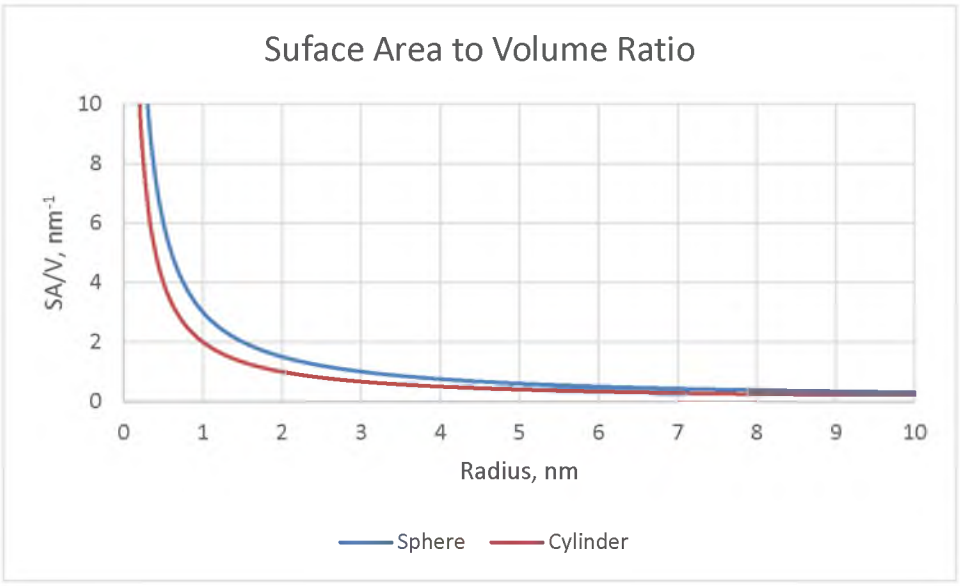

Figure 13: Graph of surface area to volume ratio for various radii.

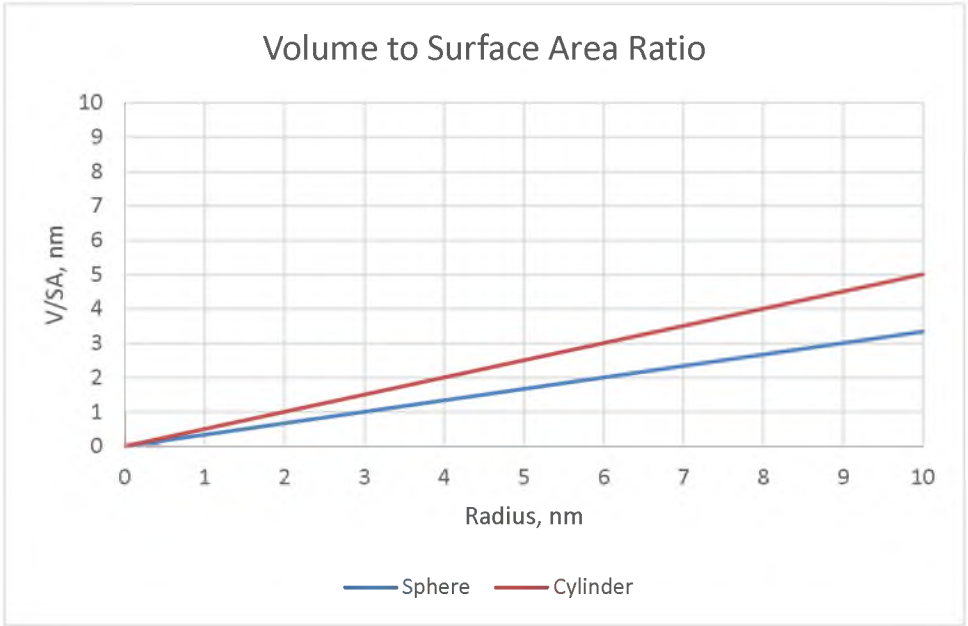

Figure 14: Volume to surface area ratio.

References

[1] S. Lowell, J. E. Shields, M. A. Thomas and M. Thommes, Characterization of Porous Solids and Powders: Surface Area, Pore Size and Density, Norwell: Kluwer Academic Publishers, 2004.

[2] D. R. Lide, CRC Handbook of Chemistry and Physics, 86th ed., Boca Raton: CRC Press, 2005.

[3] CheapTubes.com, "Cheaptubes.com," 14 March 2014. [Online]. Available: http://www.cheaptubesinc.com/swnts.htm. [Accessed 2 April 2014].

CHAPTER III

TEMPERATURE PROGRAMMED OXIDATION

Overview

Temperature programmed oxidation, TPO, tests the weight loss due to oxidation of the carbon material. Air is flowed over the sample as the temperature is ramped to 800 °C. The weight loss due to this oxidation is measured along with the CO_2 signal on a mass spectrometer (MS). The shape of these peaks and the temperature at which they occur tells how many carbon species are in the sample and points to the bonding characteristics of these species. The thermogravametric analyzer (TGA) weighs the sample as the oxidation process is occurring. The derivative of the mass loss during the heating provides peaks that correspond with the CO_2 signal from the MS. This added step increases the accuracy of the temperature where the peak occurs as opposed to using the MS data only due to the turbo pump of the MS having a variable and unmonitored pressure. Furthermore, using just the GA data eliminates an iterative step. A demonstration of these data being used as a substitution for the MS signal is shown in this work. The TPO test also allows for a glimpse into the purity of a sample. As the temperature is ramped past the decomposition of the carbon material the remaining material is the remaining catalyst. This is seen visually from a red brown powder that remains which is indicative of iron oxides. The homogeneity of the powders can be

shown by testing multiple samples and comparing the results.

Method

There are no ASTMS currently for this type of testing. ISO/TR 10929 and ISO/TR 11308 address characterization of nanotubes using thermogravimetric analysis. To accurately find the temperature of the oxidation and to avoid combustion, the sample is heated slowly at 5 °C/min. The analysis occurs with air running past the sample at 100 mL/min, while being weighed simultaneously. This gas flow rate prevents the build-up of CO and CO_2 that slows the reaction kinetics. To minimize the effect of mass transfer through the powder a thin layer of the sample was placed in the crucible. The amount varies with the density of the material but is limited between 3 to 10 mg as to minimize any mass transfer effects. Care was taken to eliminate any clumps of powder to minimize discrepancies. A MS was attached to the output of the TGA to collect data pertaining to the peak of CO_2 partial pressure coming off of the sample. Some delay is seen from the mass loss to the MS CO_2 signal peak that time delay is around 5 minutes. This is directly attributed to the travel time of the gas through the capillary that runs from the TGA to the MS. Multiple runs were used to assess homogeneity within the sample. Since there is no temperature measurement directly from the MS data, the temperature from the TGA with a time stamp is used. Then the time of the MS signal is converted to the temperature of the sample from the TGA data. Although not perfect, the consistancy of the temperature ramp of the TGA is such that it is a viable correlation. Figure 15 demonstates the linear relationship between time and temperature.

Results

The TGA produces graphs that show the mass loss and the derivative of that signal with respect to temperature (see Figure 16). Here the peak can be found for this sample at 571 °C. The derivative signal can be superimposed with the MS CO_2 with a time vs temperature correlation shown in the method section to produce the second graph.

The peak on the MS CO_2 signal is at 590 °C (see Figure 17). This 19 °C difference correlates to a time delay of 3.23 minutes. The MS peak is shifted to make up for this delay, resulting in identical peak shape for the CO_2 MS signal and the derivative of the mass loss signal from the TGA. This allows for the TPO data to be used instead of the MS data, which is helpful because it eliminates one piece of equipment and one sequence of calculations. The derivative of the mass loss will hereafter be known as the TGA signal.

Carbon Nanotube Samples

Two runs of the TPO testing were performed on powder samples from the same source. Figure 18 shows the TGA runs for the MWNT and the SW/DWNT. The MWNT samples show a strong single peak at 570 °C. The SW/DW NT powder has a different shape to its curve. There is a very narrow peak at 575 °C, followed by a shoulder on the high temperature side. This shoulder is prominent in the TGA data but also exists in the MS CO_2 signal. This shoulder indicates that this peak is a combination of at least three peaks. This is a notable difference between the MWNT and the SW/DWNT because it indicates that there is more variety seen in the types of carbon bonds in the SW/DWNT sample. Peak decomposition is performed and discussed later in this work. The MS CO_2

signals are all adjusted so that the background is at 0, since these units are arbitrary.

Other Carbon Species

Both the graphene and pet coke samples were tested with identical testing conditions to the NT samples. The same adjustments were made for the MS signal. The graphene samples show a lot of noise in the MS CO_2 signal, and shorter peaks for the TPO as well (see Figure 19). As the purity results shown later will confirm, this sample had the most noncarbon material, so there was not as much carbon to decompose as the other samples. There is a large broad peak at 580°C, with a second peak at 650°C. The pet coke decomposition was incomplete because it initiated at a much higher temperature. This shows that this carbon species has different bonding structures then the rest of the samples.

Along with the standards, samples from a production facility were tested for comparison. They are labeled C1-C3 and shown in Figure 20. The plant samples are compiled in Figure 21 to show how similar different aliquots of the same batch of powder perform. Not only are the peaks at about the same place, the width of the peaks are very similar. The peak seen is broader than the SW/DWNT peak but tracks well with the MWNT sample tested.

Table 4 summarizes the data and calculations performed. The data from each sample tested for all carbon species is shown followed by the average and standard deviation. The first column shows the temperature value associated with the peak of the derivative of the mass loss, the TGA signal. The largest standard deviation is 4 °C. This speaks to high sample homogeneity and the excellent reproducibility of this test using the

Q600. The next column, shows how much metal catalyst is in each sample by a percentage of mass remaining after each sample was heated to the 800 °C. This value has a range of 2% to 25%. The final column shows the width in degrees C of the peak at half of the maximum intensity. A narrow peak shows that the carbon that is being oxidized at that particular temperature is highly uniform. Defects and carbon impurities will cause a peak to have a broader profile. A visual representation of this data is shown in Figure 22.

Using Origin (version 8.6.0 Sr3 made by OriginLab Corporation), the peaks shown above can be decomposed to show the peaks that are obscured. First looking at the nanotube samples, we see that they have three peaks represented in the si (3.1) ık seen. All are fitted to be Gaussian curves; fitting the equation:

$$y = y_o + \frac{A}{w * \sqrt{\frac{\pi}{4 \ln 2}}} * e^{-\frac{4*\ln 2*(x-x_c)^2}{w^2}}$$

Origin provides the fitting variables for each curve. To ensure a good fit the software minimizes the reduced chi square value, to obtain the optimal parameter values. Although typically the reduced chi squared value will be close to 1 to determine a good fit, this value is scaled with the y axis, that is, if you multiplied the y values by a scaling factor the reduced chi squared value would scale as well. The goodness of fit is determined by the adjusted R^2 value, which takes into account the degrees of freedom of the data. This is given by the following equation:

$$\bar{R}^2 = 1 - \frac{RSS/df_{error}}{TSS/df_{total}} \qquad (3.2)$$

Here *RSS* is the residual sum of squares, that is, the sum of squares of the measured point minus the predicted point by the fitting parameters. *TSS* is the total sum of squares, that is, the summation of the squares of the difference between the measured y value and the

mean of the y values. df_{error} and df_{total} are the degrees of freedom for the error and the total, respectively. Figures 23 through Figure 25 and Table 5 summarize the findings.

The fitting curves perform well in revealing the hidden peaks below the curve. The adjusted R^2 value shows a remarkable goodness of fit for the combined curve values. From sample to sample of the same species there is good uniformity of the data. The SW/DWNT samples show the narrowest peaks, speaking more to their high purity while the industrial samples show wider peaks. Graphene has the clearest three peaks of any of the samples. There is one peak at around 655 °C, one at 580 °C and one at 525 °C, with the largest peak being the center one. The SW/DWNT and the MWNT samples show two common peaks, one at 575 °C and one at 560 °C. There is a peak at 560 °C in the C samples at about this same temperature corresponding to about 30-40% of the sample. This indicates that the same carbon species, carbon nanotubes are present in all three samples. The additional peak seen in the SW/DWNT samples at 645°C shows the destruction of the single walled tubes which needs more energy to break the stronger bonding. The pet coke peaks are at a much higher temperature indicating a very different form of carbon bonding.

Literature Discussion

Kitiyanan et al. have proposed that amorphous carbon will show a CO_2 peak at 330 °C, with a SWNT peak at 510 °C, and graphite having a broad peak that starts at 700 °C. [1] These peaks were also produced in work done by Alvarez et al. Here the amorphous peak was the same, with the graphite peak centered at 620 °C and the addition of a MWNT peak at 590 °C.[2] They went further to decompose broad peaks using

Gaussian-Lorentzian mixture of curves to assign more particular peaks when the signal is broad, shown in Figure 26. This decomposition shows very broad peaks that hold five peaks at 350, 450, 490, 550, and 600 °C. These results were obtained with a heating rate of 12 °C/min. This methodology shows that a faster heating rate will result in broad peaks that may force the CO_2 signal to peak early if the powder is consumed before the true peak temperature is met. The signal at 350 °C shows some amorphous carbon in the sample.

Conclusions

The broadening of a peak speaks to how pure the carbon material is and if there are any defects in the structure. Looking at the peaks shown in Figure 24, the graphene signal is a good example of at least three peaks compiled into one. The primary peak occurs at 580 °C, with the other two peaks at 500 °C and 660 °C. The literature values do not correlate very well to the peaks seen in this research. There are no samples that show a peak at 330 °C, which was attributed to amorphous carbon. The SW/DWNT peak shows a broadening from 615 °C to 715°C, while both the MWNT and the industrial samples have visually balanced peaks. The pet coke peak is a clear outlier of this group of species peaking at 770 °C.

Table 4: Summary of TPO data, including the temperature of the peak, the residue percent, and the width of the peak at half height.

	TPO Temperature , °C	Residue Percent	Width at half height, °C
MWNT -001	566.51	8.35%	63.82
MWNT 005	570.30	5.19%	55.50
MWNT-AVE	568.40	6.77%	59.66
MWNT-STD	2.68	2.24%	5.88
Pet Coke -001	774.23	2.87%	54.15
Pet Coke - 003	772.79	0.03%	57.02
Pet Coke-AVE	773.51	1.45%	55.58
Pet Coke-STD	1.02	2.01%	2.03
Graphene -001	580.91	15.75%	86.36
Graphene -003	576.09	25.39%	81.01
Graphene-AVE	578.50	20.57%	83.68
Graphene-STD	3.41	6.82%	3.78
SW/DWNT -001	574.39	3.58%	31.04
SW/DWNT -002	578.45	3.70%	34.57
SW/DWNT-AVE	576.42	3.64%	32.80
SW/DWNT-STD	2.87	0.09%	2.50
C -001	605.03	4.95%	75.65
C - 002	597.15	7.11%	56.93
C - 003	601.85	4.41%	73.77
C-AVE	601.34	5.49%	68.78
C-STD	3.96	1.43%	10.31

Table 5: Summary of the peak decomposition for all samples.

		Peak temperature, x_c, °C	Peak maximum, y(x_c), %/°C	Width at half height, w, °C	Percent of total area	R^2 value
MWNT 001	y1	577.7	0.611	31.7	28.8%	0.999
	y2	554.4	0.795	50.0	52.5%	
	y3	518.8	0.260	86.3	31.9%	
MWNT 005	y1	574.8	0.761	26.0	28.0%	0.999
	y2	554.7	0.834	46.1	48.8%	
	y3	522.5	0.319	83.9	35.3%	
SW/DWNT 001	y3	642.3	0.134	71.0	18.0%	0.997
	y1	574.4	1.250	20.4	36.3%	
	y2	558.6	0.764	62.1	62.1%	
SW/DWNT 002	y3	647.9	0.132	64.7	17.3%	0.996
	y1	578.5	1.159	21.5	36.1%	
	y2	560.3	0.792	63.5	63.6%	
Pet Coke 001	y1	773.9	1.001	30.5	36.7%	0.994
	y2	746.8	0.823	74.8	68.1%	
Pet Coke 003	y1	772.4	1.045	32.1	40.3%	0.994
	y2	741.5	0.799	70.6	64.4%	
Graphene 001	y3	658.2	0.082	29.8	17.4%	0.994
	y1	582.6	0.584	50.0	51.3%	
	y2	529.3	0.380	100.0	61.2%	
Graphene 003	y3	655.6	0.074	31.3	13.7%	0.994
	y1	577.8	0.563	50.4	50.9%	
	y2	521.5	0.326	102.0	57.0%	
C 001	y1	607.1	0.906	64.3	66.4%	0.998
	y2	558.8	0.288	104.9	34.9%	
C 002	y1	599.1	0.850	48.9	46.8%	0.995
	y2	573.8	0.408	113.7	52.4%	
C 003	y1	604.2	0.934	64.9	67.4%	0.998
	y2	555.3	0.270	108.5	32.3%	

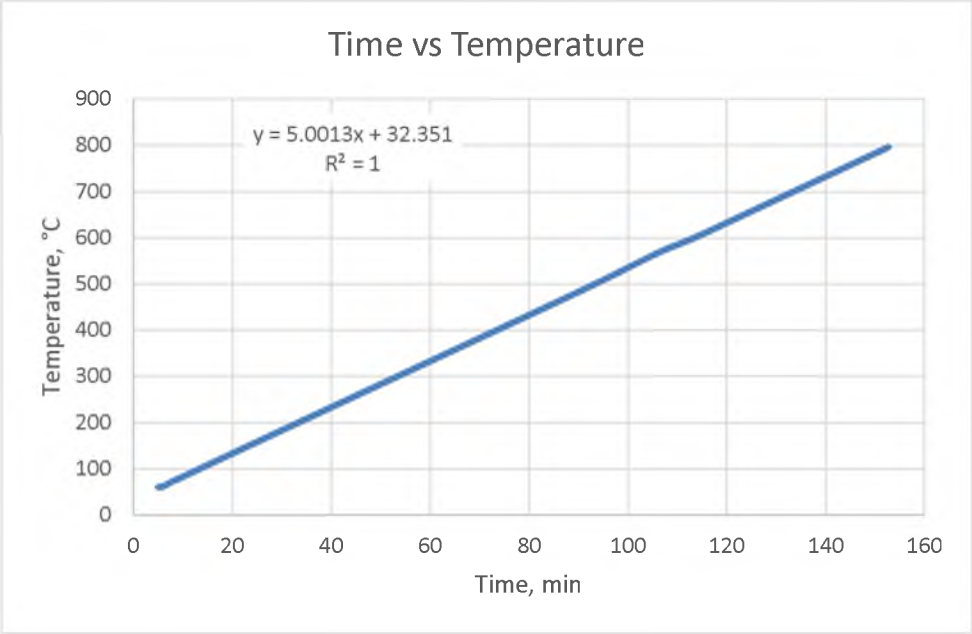

Figure 15: Graph showing the linear relationship between temperature and time in the TGA.

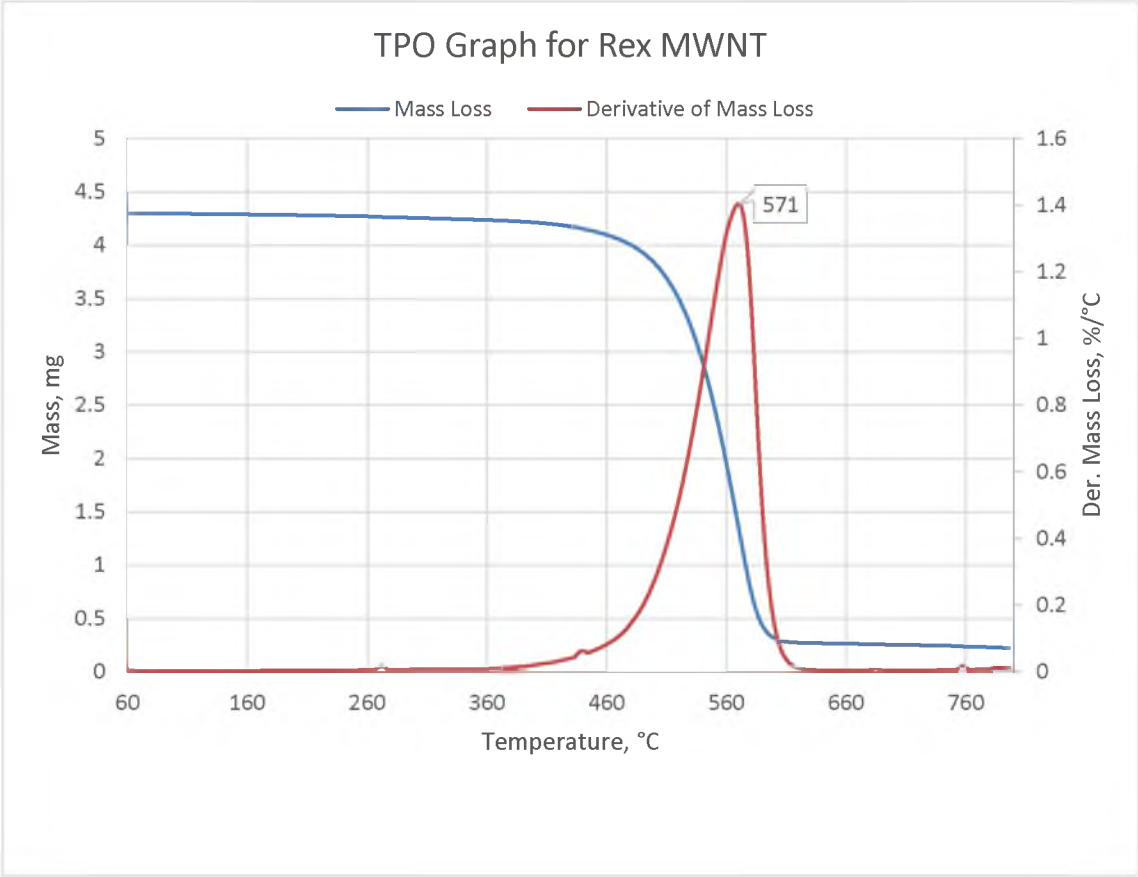

Figure 16: TPO data for REX MWNT sample. This test was performed with air flowing over the sample at 100 mL/min and a temperature ramp of 5°C/ min.

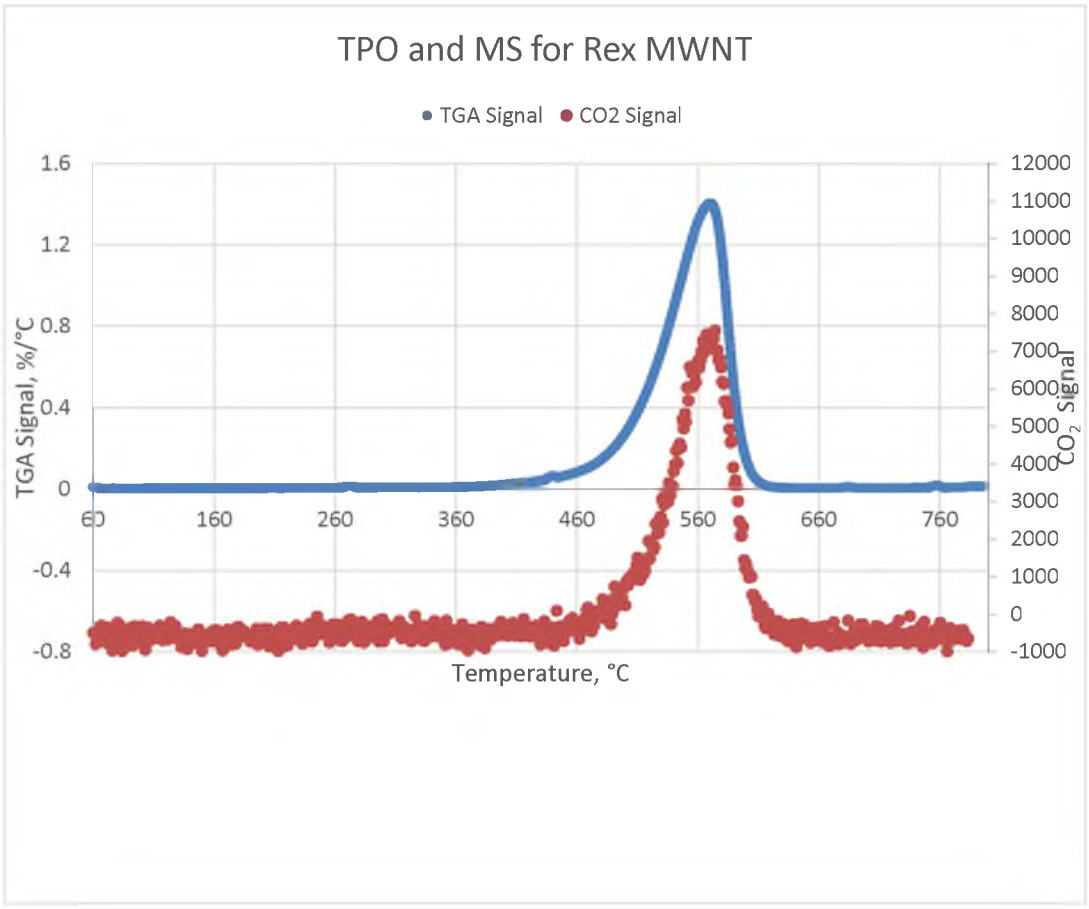

Figure 17: An overlay of the MS CO2 signal and the derivative weight loss signal from the TGA. The MS signal is adjusted on the Y axis to allow the background to be zero and is adjusted on the X axis to have the peak occur at the same temperature.

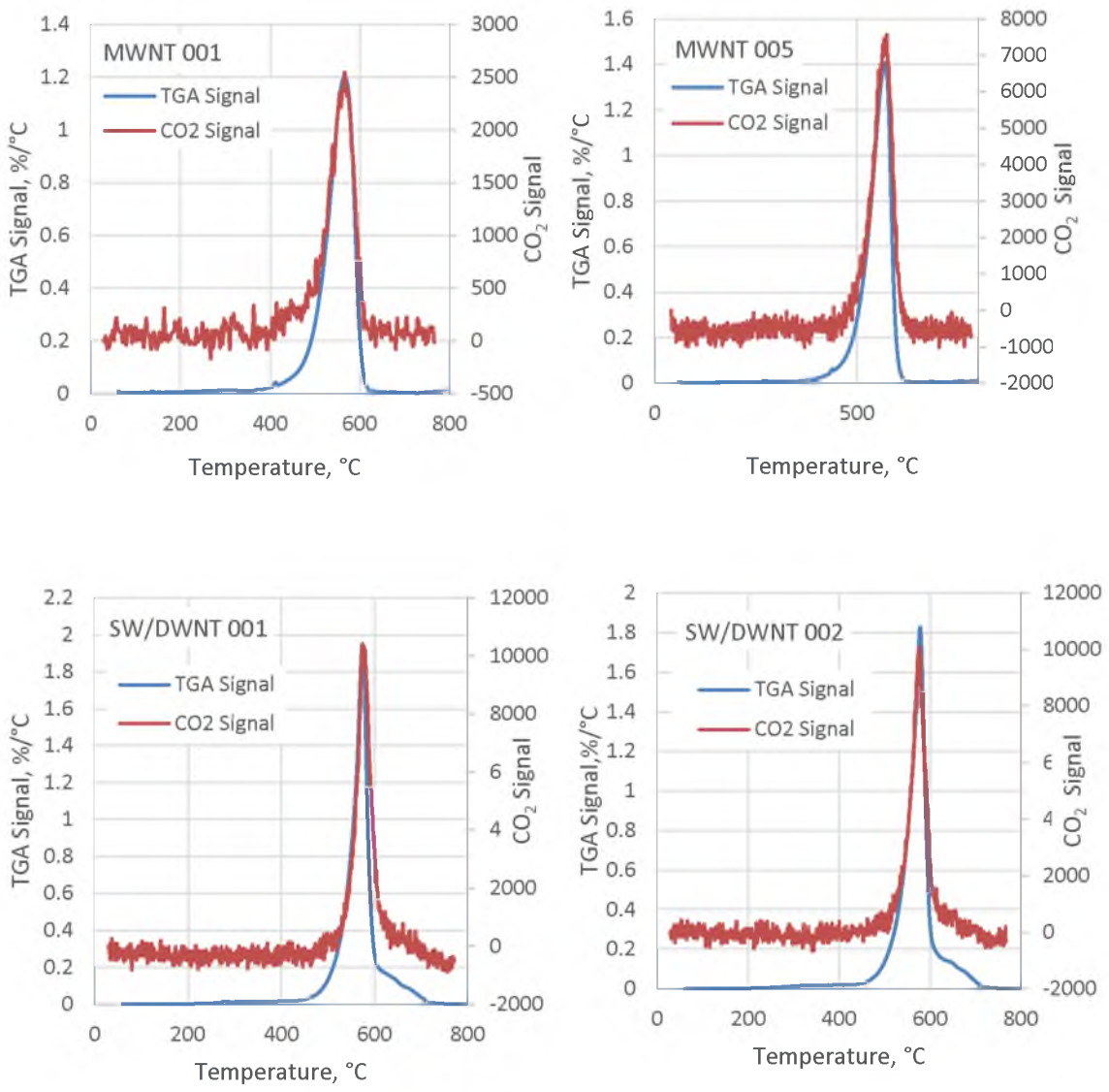

Figure 18: TGA and MS signals overlaid for MWNT and SW/DWNT samples. The MS signal is adjusted on the X axis to incorporate the time delay and is adjusted on the Y axis so the background is set to 0.

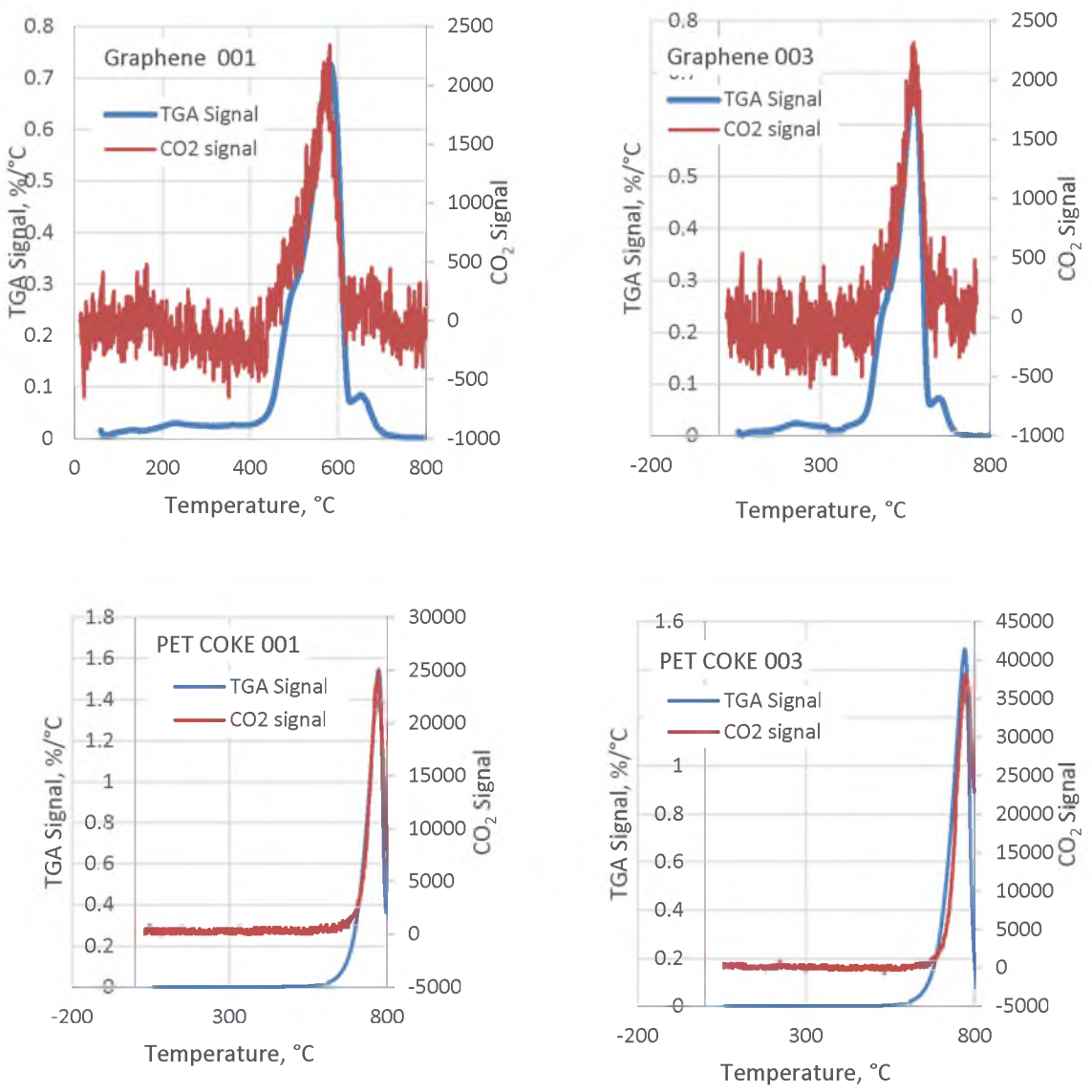

Figure 19: TGA and MS signals overlaid for graphene and pet coke samples. The MS signal is adjusted on the X axis to incorporate the time delay and is adjusted on the Y axis so the background is set to 0.

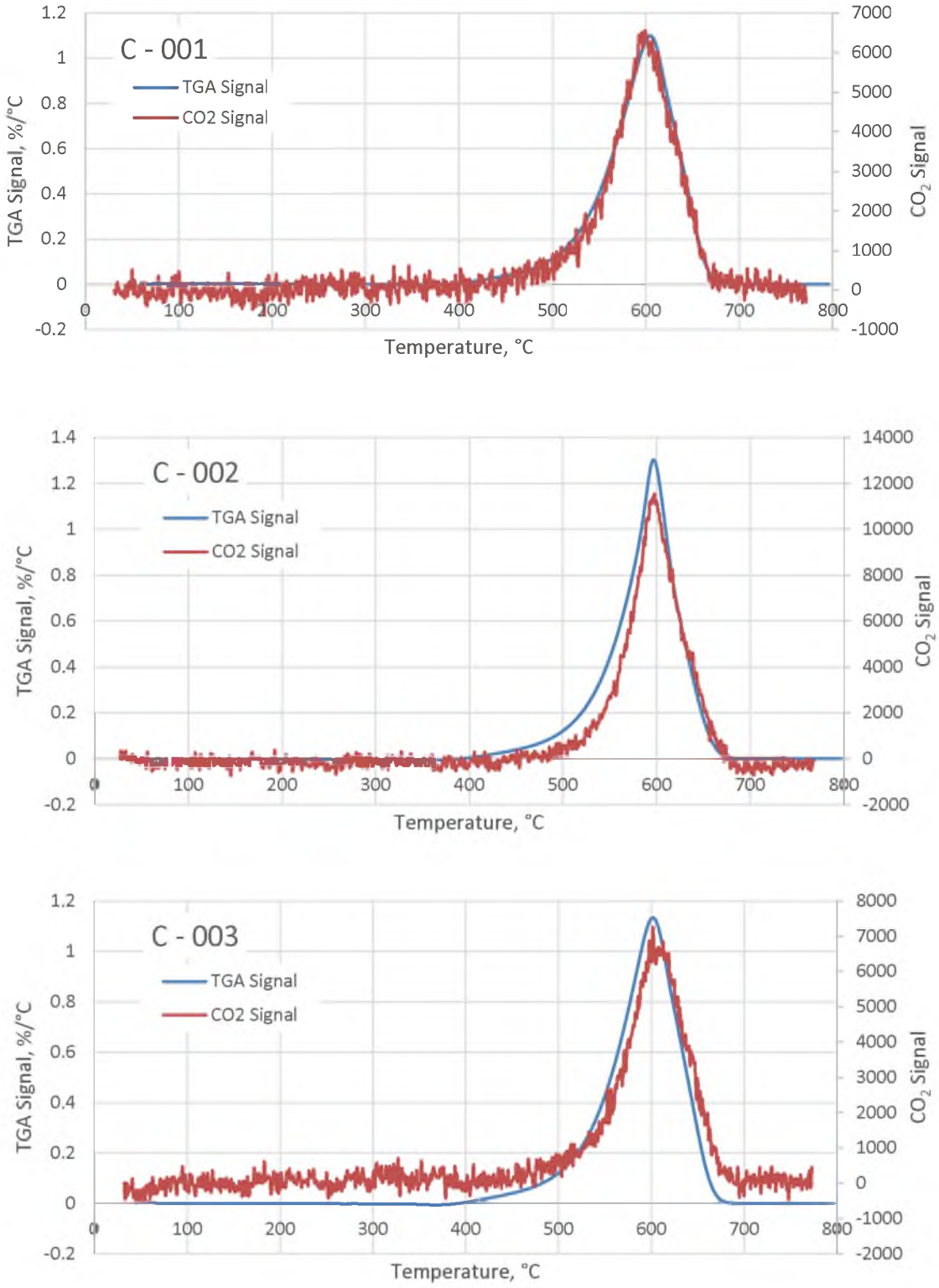

Figure 20: TGA and MS signals overlaid for production plant samples. The MS signal is adjusted on the X axis to incorporate the time delay and is adjusted on the Y axis so the background is set to 0.

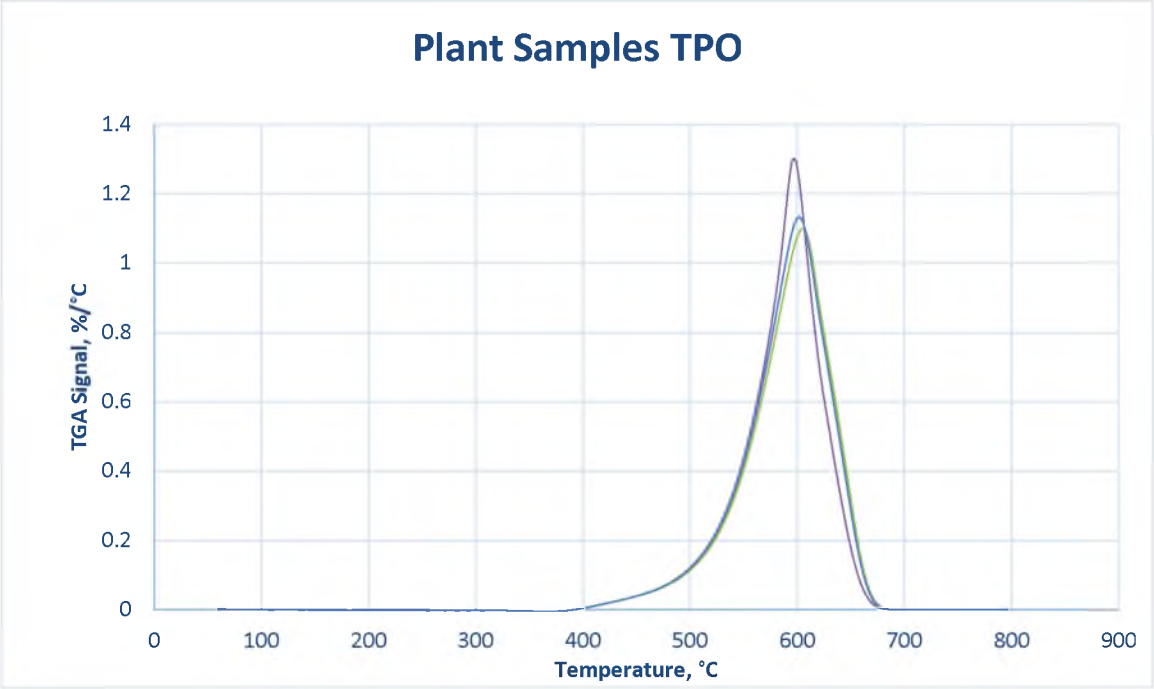

Figure 21: A graph showing the production samples overlaid on top of each other. This shows a high repeatability in the experimental procedure.

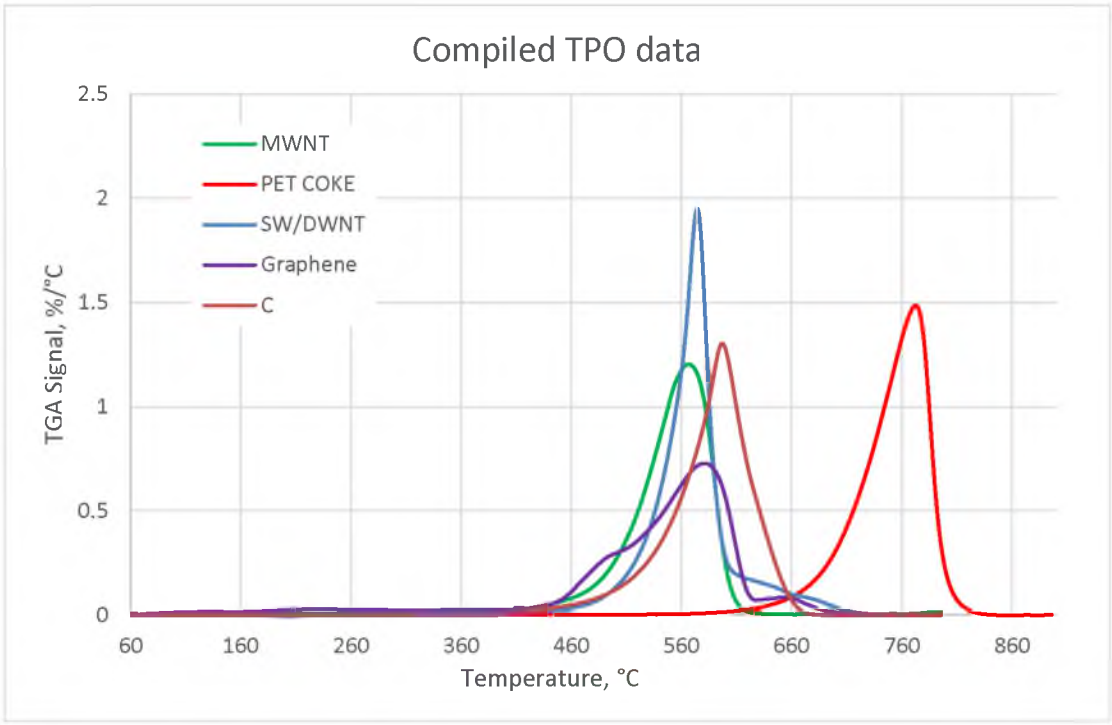

Figure 22: Compilation of TPO data.

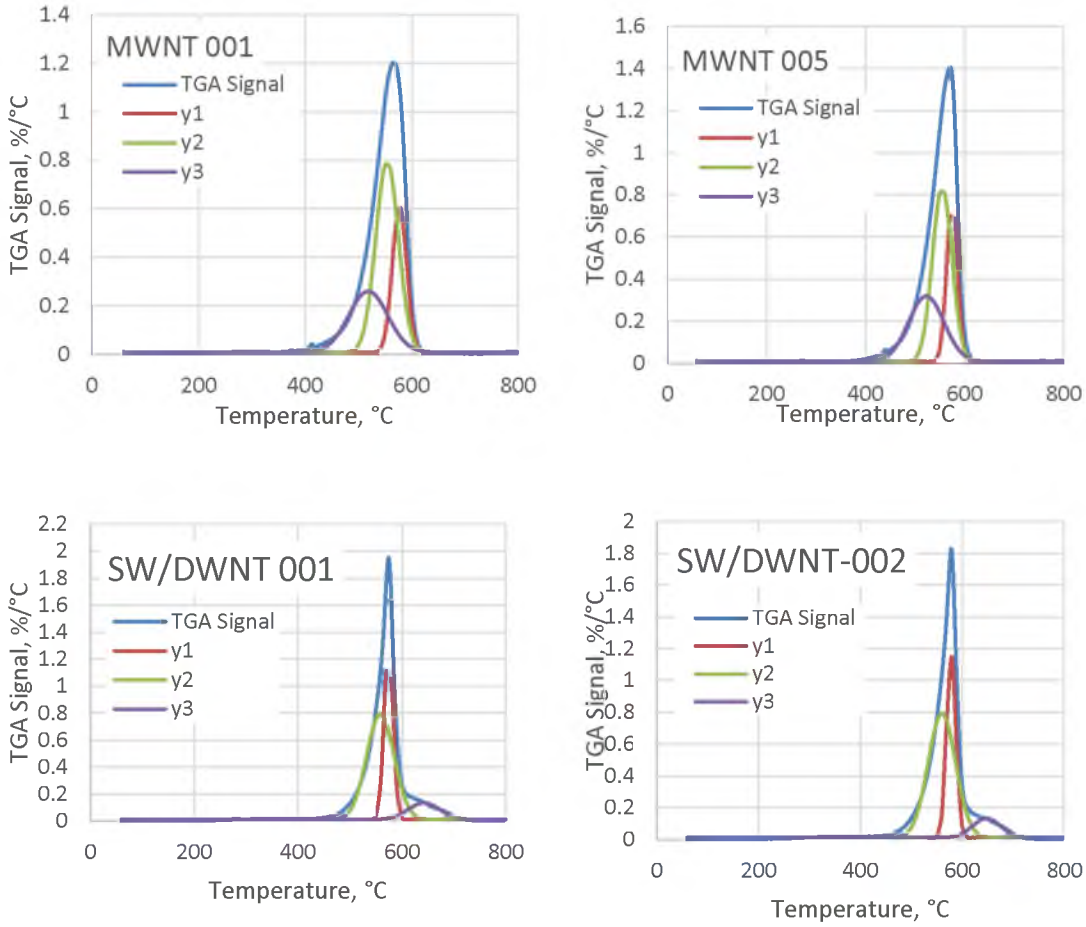

Figure 23: Peak decomposition graphs for the MWNT and SW/DWNT samples.

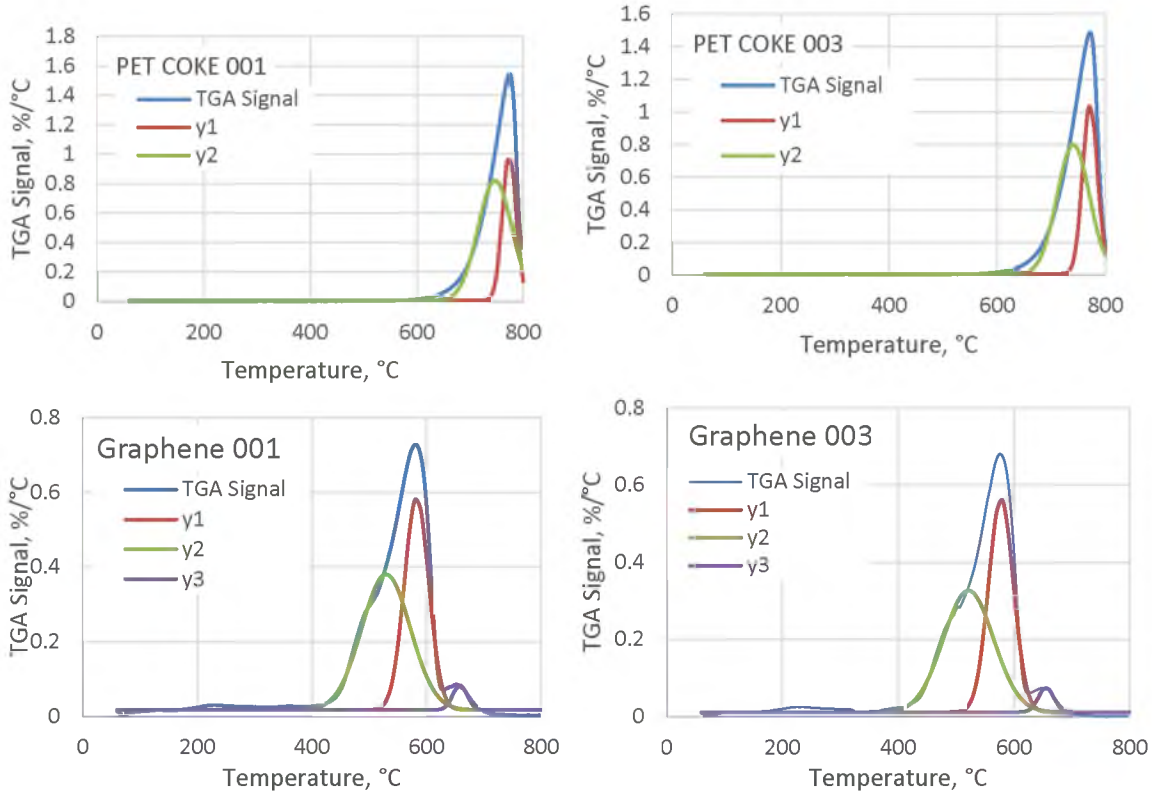

Figure 24: Peak decomposition graphs for graphene and pet coke.

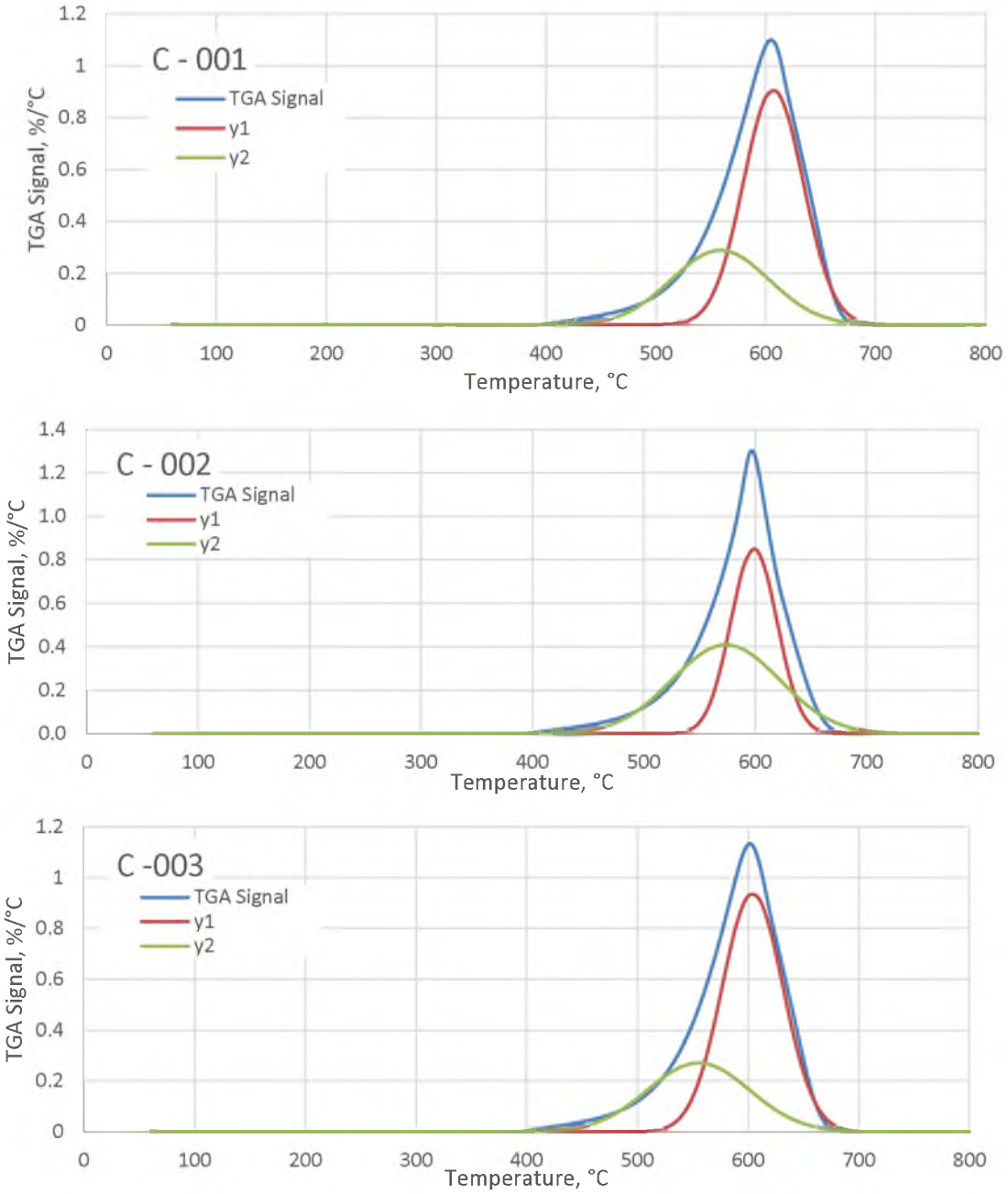

Figure 25: Peak decomposition for the industrial plant samples.

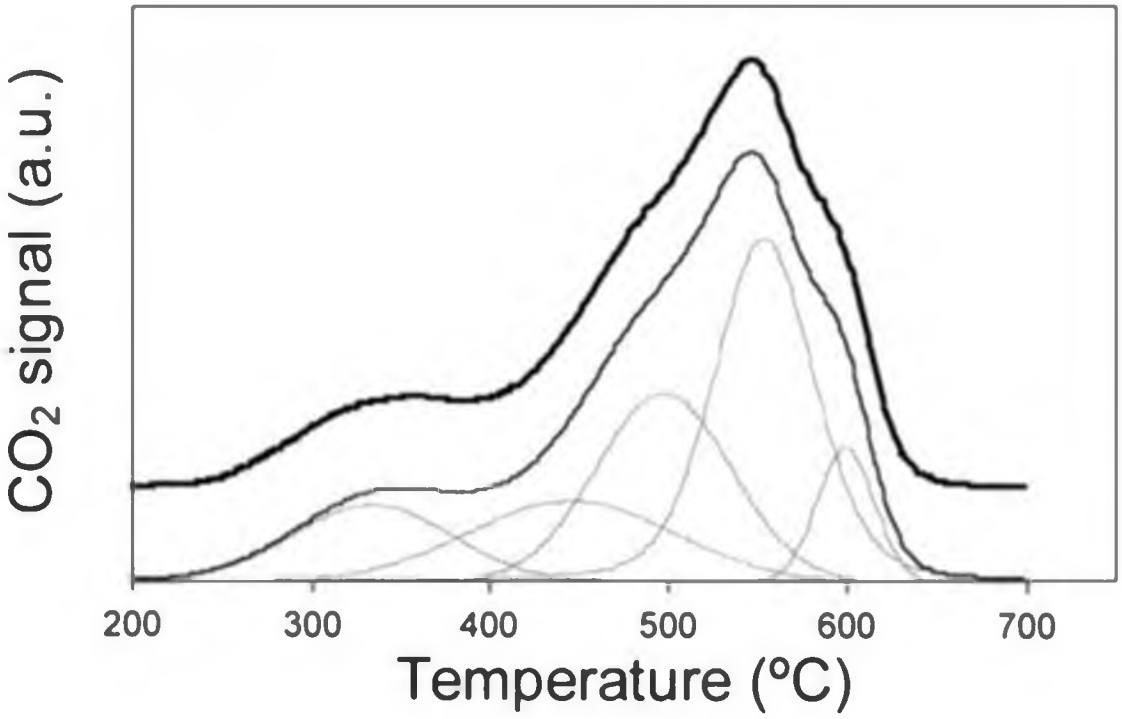

Figure 26: TPO results from previous study on SWNT. (Modified from ref. 2.)

References

[1] B. Kitiyanan, W. Alvarez, J. Harwell and D. Resasco, "Controlled production of single-wall carbon nanotubes by catalytic decomposition of CO on bimetallic Co–Mo catalysts," *Chemical Physics Letters,* vol. 317, pp. 497-503, 2000.

[2] W. Alvarez, B. Kitiyanan, A. Borgna and D. Resasco, "Synergism of Co and Mo in the catalytic production of single-wall carbon nanotubes by decomposition of CO," *Carbon,* vol. 39, pp. 547-558, 2001.

CHAPTER IV

SPECIFIC HEAT CAPACITY

Overview

The specific heat capacity of a substance describes how quickly the material changes temperature when thermal energy is supplied. Typical units for this property are J/mol*K. A high specific heat means that it will take more energy to raise the temperature of the material and more energy can be stored within in the molecular vibrations in the material. Energy storage is done by several mechanisms; the most important for carbon nanotube classifications is the storage of energy through phonons. Phonons are vibrations within the structure of a molecule. The more complicated the molecular structure, the more phonons or modes of vibration are available, so the more heat can be stored in these vibrations giving higher heat capacity. There is an additional electronic contribution to the specific heat capacity, when the density of electronic states is not zero at the Fermi energy, i.e., a poor electrical conductor. The electronic contribution is small compared to the phonon contribution at these temperatures. [1] When the density of filled electronic states in the conduction band is large, i.e., with a good electrical conductor the electronic contribution to the heat capacity is larger than the phonon contribution for nonmetallic materials. [2]

Method

The method used to determine the specific heat capacity is ASTM E1269. This uses a thermogravemetric analyzer (TGA) from TA Instruments model Q600. This instrument consists of a furnace and two arms to hold samples. Incorporated in these arms are very sensitive thermocouples and scales, so as the sample is heated, the temperature change and weight loss can be measured. Simultaneously knowing the amount of energy being put into the sample and the effects on the temperature on the sample will allows the specific heat capacity to be determined. This can be done directly or by comparison with the specific heat capacity of a sapphire standard. In either situation it is important to know the accuracy of the results. ASTM E1269 provides a means of calculating the calorimetric sensitivity, E, by running the TGA with an empty specimen holder, and with the sapphire standard. Then the difference in the heat flows is used in the following equation to find the sensitivity, E;

$$E = \left(\frac{b}{60 * D_{st}}\right) * \left(W_{st} * C_p(st)\right) \tag{4.1}$$

In this equation, b is the heating rate in °C/min, D_{st} is the vertical displacement between the empty specimen holder heat flow curve and the sapphire heat flow curve at a given temperature (shown in Figure 27), W_{st} is the mass of the sapphire, and $C_p(st)$ is the specific heat capacity of sapphire, a function of temperature tabulated by a polynomial fit of the data that is given in the ASTM standard, 60 is a conversion factor for seconds to minutes. It is important to note that this sensitivity, E, has no dependence on the sample and is unitless. It is simply how well the measurements for specific heats match up to the literature values. As seen in Figure 27, this method leaves a temperature range from about 400 K to 650 K where a stable value for D_{st}, is observable. This is the range in

which further calculations are made. This translates to a window for the E values as well, which is shown in Figure 28.

With this information we can now calculate the specific heat capacity. As mentioned earlier, there are two methods listed in ASTM E1269. One uses the E value found and the other one compares the sample and the standard. In the following equations, D_s, and W_s, represent the distance between the sample and the empty specimen holder and the weight of the sample, respectively.

$$C_p = \frac{60 * E * D_s}{W_s * b} \tag{4.2}$$

or

$$C_p = C_p(st) * \frac{D_s W_{st}}{D_{st} W_s} \tag{4.3}$$

The second method is recommended only when the TGA is calibrated before every run, which was not usually done. However, a comparison of the two methods results in the same number for C_p. This allows for either method to be used for our calculations. Since E and b are independent of the sample, if we choose the first method the only term that is a function of temperature will be D_s. This allows for an easier calculation to be developed to quickly and efficiently analyze multiple runs.

Results

Multiple runs of an early pilot plant sample, J2011, with known carbon nanotube content were performed and shown in Figure 29. There are three groups of values in the J2011 graph, ranging from 11 to 18 J/mol K. Group 1 has a value of 18 J/mol K at 390 K; group 2 has values ranging from 13 to 16 J/mol K; group 3 has a value of 12 J/mol K.

This can be attributed to the lack of homogeneity of powder sampling. This result is important to remember when attributing values to different samples. Testing of the current standards used through this text were performed. For a comparison these values were superimposed on a graph with NIST Chem Webbook numbers for other carbon materials and shown in Figure 30. There are two clear outliers seen, with the plant sample C-001 having the lowest specific heat and the pet coke having the highest value of heat capacity and the largest slope. As predicted, the MWNT show a higher specific heat capacity than the SWNT. This is due to the increase in complexity resulting in the increase in phonons. C60 and C70 are other nanoparticles, often called bucky-balls, which are spherical with the same type of carbon-carbon bonding.

The heat capacities of the pilot plant samples found through this method are consistent with the heat capacities of other complex carbon material. This speaks well to the accuracy of this experimental method. The temperature range is highly limited. However, when the temperature is lower than 370 K, there are large fluctuations in the heat flow measurement due to the initial heating of the sample. At higher temperatures, the calculation degrades due to the subtraction of the empty cup measurement from the sample. A larger temperature window is desired for a more conclusive results, but for these preliminary runs there is promise that the carbon structures in the pilot plant samples contain highly structured carbon bonding.

Error Analysis

Two methods are available for error analysis. The first is to propagate the manufacturer's errors in measurement, and the second is to use the data collected to find the error. Both methods of error analysis are performed and compared. When looking at the specific heat calculations there are four sources of error:

1. Error in calorimetric sensitivity, E
2. Error in vertical displacement, D_s
3. Error in sample weight, W_s
4. Error in heating rate, b

The manufacturer errors are listed on Table 6.

Using the Error Propagation Web Tool made by Tony Butterfield at the University of Utah, these errors can then be propagated into the calorimetric sensitivity,

Using the Error Propagation Web Tool made by Tony Butterfield at the University of Utah, these errors can then be propagated into the calorimetric sensitivity, E, and then into the specific heat capacity. This tool calculates the analytical, numerical and Monte Carlo error analysis methods with a confidence level of 95% at a specific temperature, 425 K. Figure 31, x_1 is the heating rate, b, in °C/min; x_2 is the weight of the sapphire standard, W_{st}, in mg; x_3 is the specific heat capacity of the sapphire standard, $C_p(st)$ in; x_4 is D_{st}, the difference in the heat flow of the empty cup and the sapphire standard at 425K. This analysis shows that using the manufacturer's specifications the largest source of error is due to the error in the heat flow measurements shown in theD_{st} value. This makes intuitive sense because the larger percentage the error in variables that show up in the denominator are magnified in any error propagation. The overall error for

E is 4.0%.

Finding the error in the calorimetric sensitivity allows us to find the error in the specific heat capacity itself, according to the manufacturer's specifications (see Figure 32). For this calculation, x_1 is E, x_2 is D_{st}, x_3 is b, and x_4 is W_s. This shows that the highest error in the specific heat, when using the manufacturer specifications is in the calorimetric sensitivity, E. This results in an error in the specific heat of 4.5%. Note that the specific heat capacity in this calculation is on a per gram basis, translated into a per mole of carbon basis results in a value of 11.25 ± 0.50 J/mol C *K.

However, there is an alternative error analysis that can be done by taking the raw data and finding an experimental data using Equation 4.3. For example, since we have a reading of temperature for every time value, we can determine the true heating rate that was obtained from the experiment. These values will differ from the manufacturer's specifications due to errors in calibration, controller issues, and a decrease in accuracy due to the wear and tear of frequent usage. Figure 33 shows the error for sample 111 at a temperature of 425 K, the same sample and temperature shown with the manufacturer's temperature of 425 K, which is the same sample and temperature shown with the manufacturer's error. The calorimetric sensitivity was determined by assuming a constant value over the temperature range. The error for this value is the standard deviation. This shows that the largest source of error for this sample is the error in b, which is the heating rate. The value of specific heat capacity using this analysis is 11.56 ± 0.51 J/mol C*K.

Literature Discussion

The specific heat of multiwalled carbon nanotubes has been modeled using an atomistic modeling technique, taking into account the structural mechanics. [3] After taking into account many variables, it is determined that there is a linear relationship between temperature and specific heat capacity of single and double walled nanotubes in the temperature range of 0-600 K, with a value of 9 J/mol K at 500 K. This model also determines that the primary dependence of specific heat is with temperature. There is negligible dependence on tube length and chirality at this temperature as well as the tube diameter and number of layers.

A lot of the work on the specific heat of carbon nanotubes has been performed at lower temperatures than this method can provide. The bulk of the research shows a linear relationship between specific heat capacity and temperature in a range of 0 to 300 K [4]. A comparison of ropes of single walled nanotubes, multiwalled nanotubes, and graphite was done in this same temperature range. Their results imply that there is very little difference in these three types of carbonaceous material with a value of 3.6 J/mol C * K at 150 K. This agrees with the theoretical model discussed above. These tests were also performed after some purification, since the tested nanotubes are formed on a metal catalyst, when testing the bulk properties the effect of the metal catalyst should be also observed experimentally. Hence the reason for the difference between theory and experiment observed in these results.

Table 6: Manufacturer error specifications.

Measurement	Error
Weight	0.1 µg
Thermocouple	0.001 °C
Heat Flow	2%

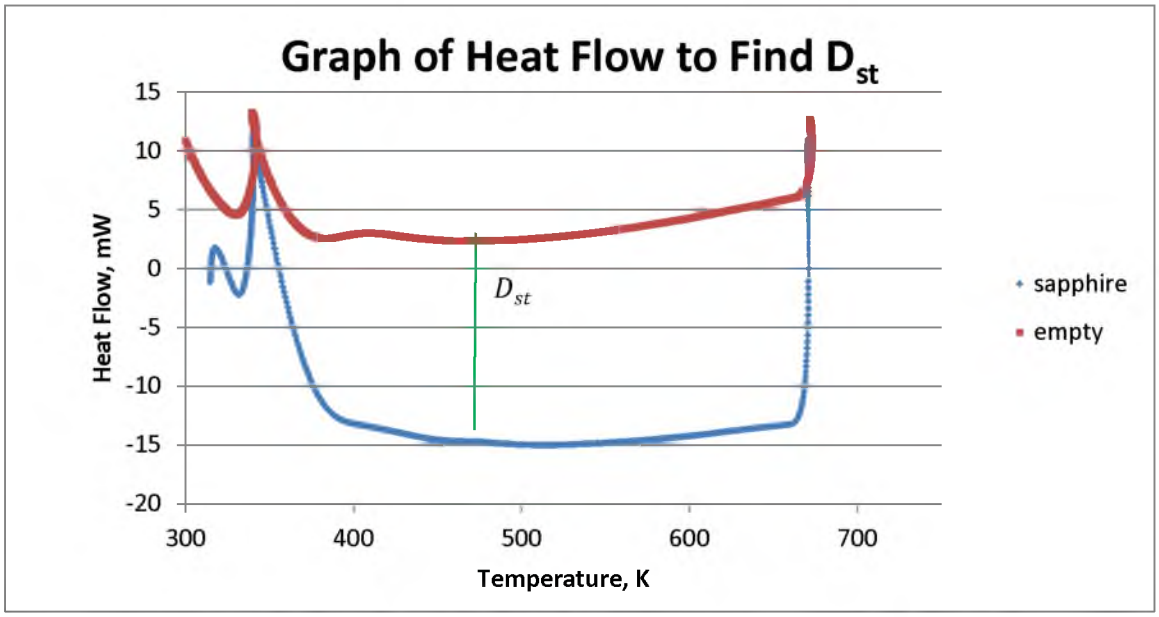

Figure 27: This graph shows how the D_{st} value is found by graphing the heat flows of the sapphire and empty sample holder.

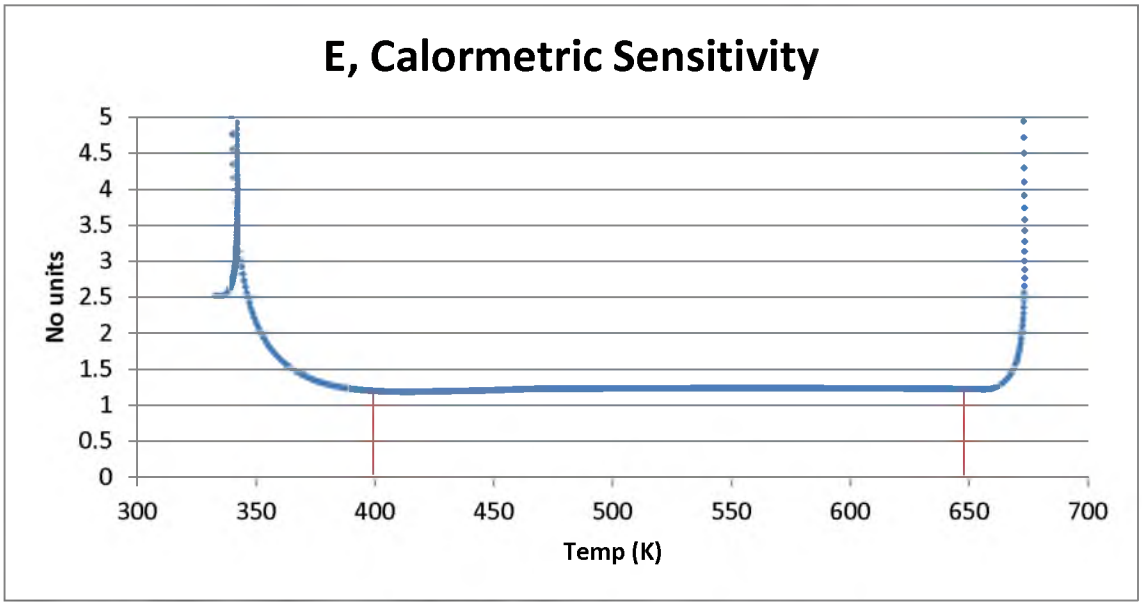

Figure 28: This graph shows calculations for E.

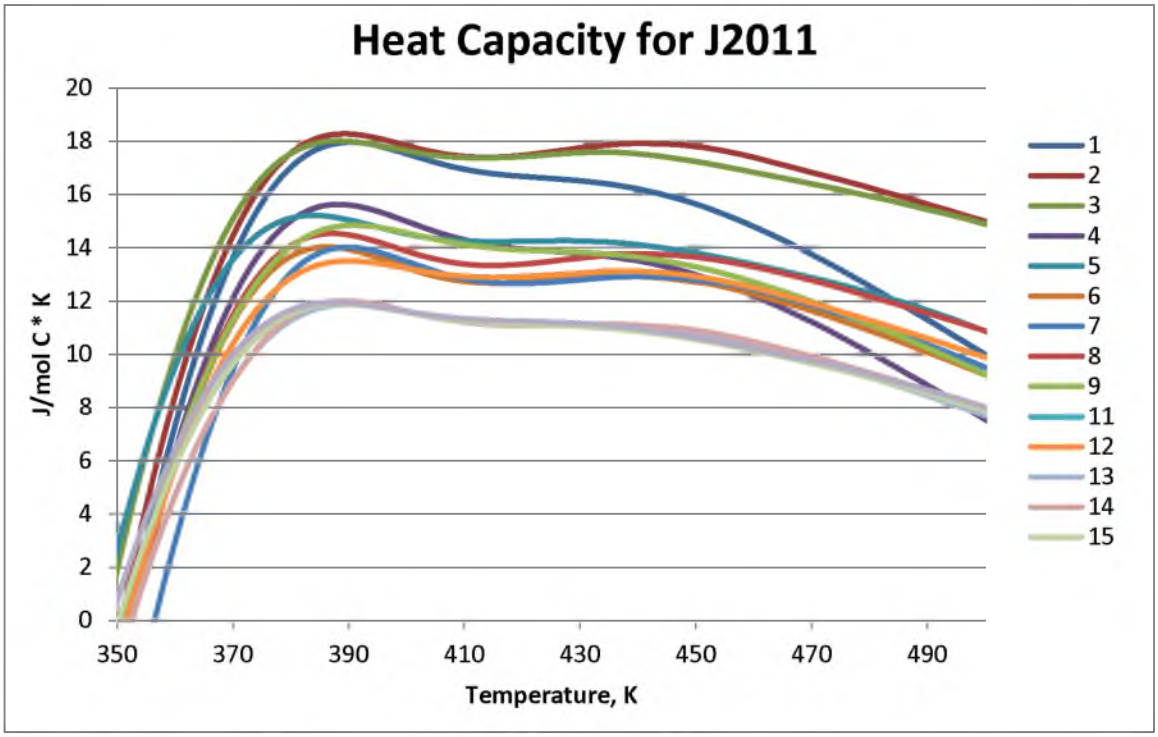

Figure 29: The specific heat capacity of J2011. Multiple runs performed to examine homogeneity.

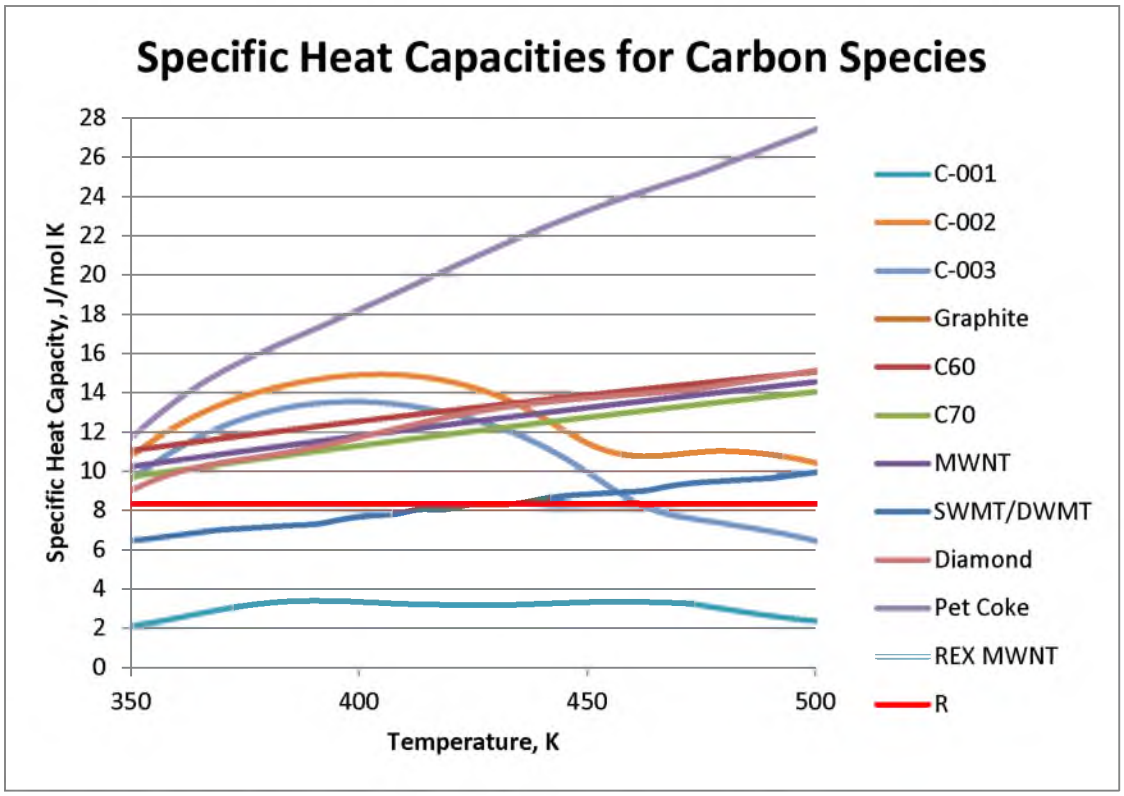

Figure 30: Specific heat capacities of various carbon species.

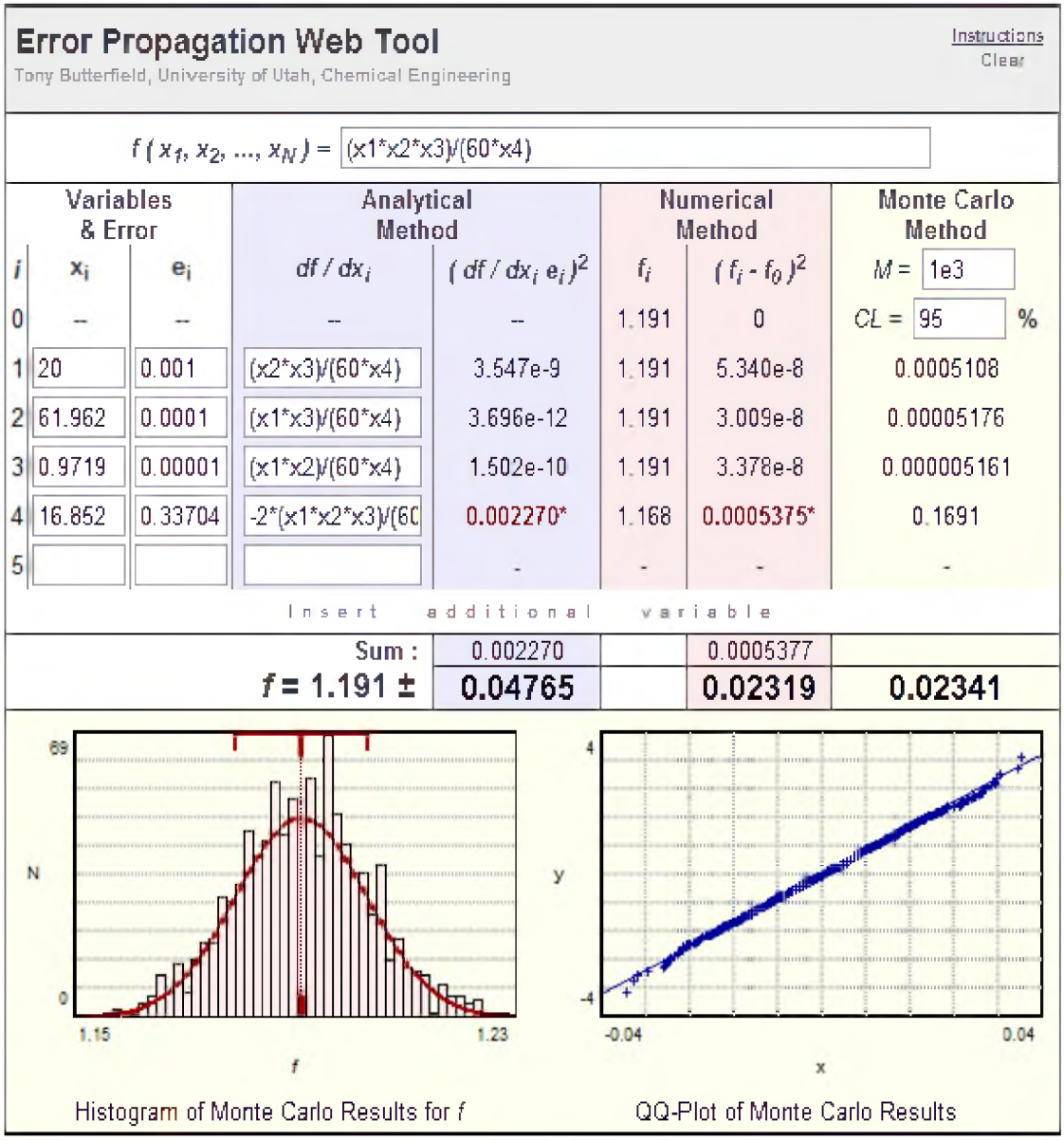

Figure 31: Error propagation for calorimetric sensitivity.

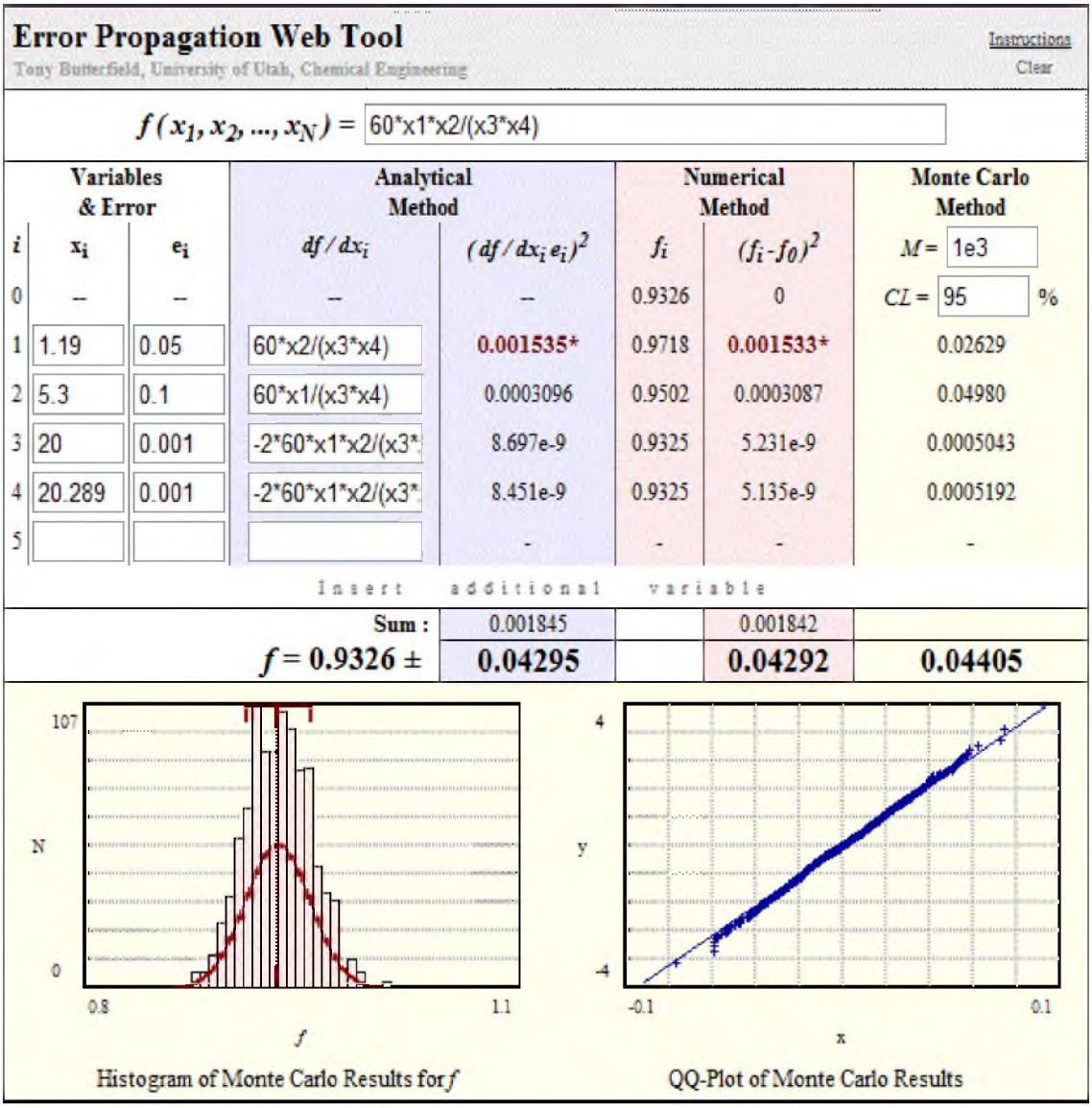

Figure 32: Error propagation for specific heat.

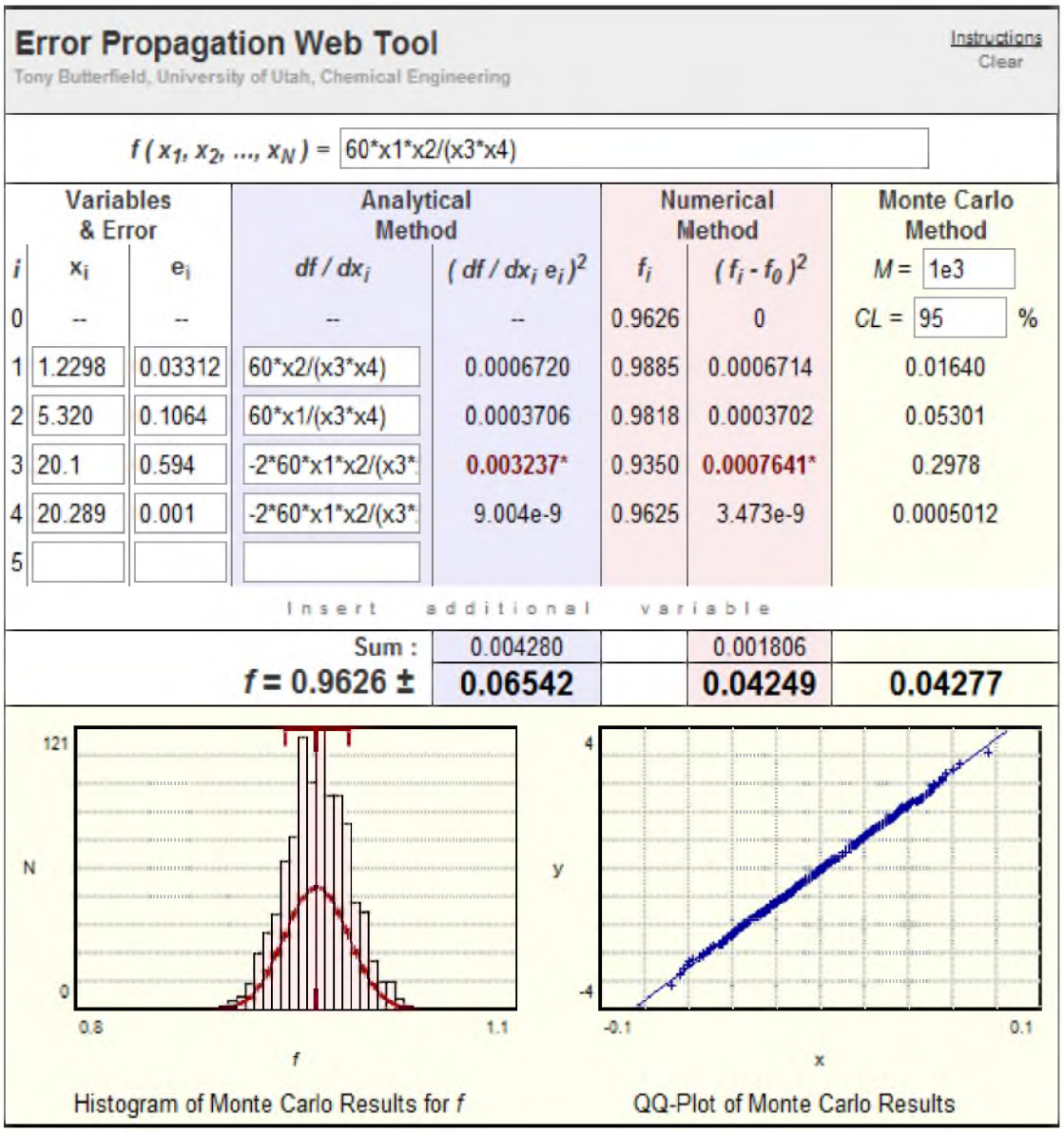

Figure 33: Error for specific heat capacity using measured error.

References

[1] A. Mizel, L. Benedict, M. Cohen, S. Louie, A. Zettl, N. Budraa and W. Beyermann, "Analysis of low-temperature specific heat of multiwalled carbon nanotubes and carbon nanotube ropes," *Physical Review B,* vol. 60, pp. 3264-3270, 1999.

[2] G. Tas and H. Maris, "Electron diffusion in metals studied by picosecond ultrasonics," *Physical Review B,* pp. 15046-15054, 1994.

[3] S. Li and T.-W. Chou, "Modeling of heat capacities of multiwalled carbon nanotubes by molecular structural mechanics," *Materials Science and Engineering A,* vol. 409, pp. 140-144, 2005.

[4] J. Hone, M. B. M. Llaguno, A. Johnson, B. Batlogg, Z. Benes and J. Fischer, "Thermal properties of carbon nanotubes and nanotube-based materials," *Appl. Phys. A,* vol. 74, pp. 339-343, 2002.

[5] W. Yi, L. Lu, Z. Dian-lin, Z. Pan and S. Xie, "Linear specific heat of carbon nanotubes," *Physical Review B,* vol. 59, no. 14, p. PRB 59, 1999.

CHAPTER V

VISCOSITY

Introduction

The viscosity of two phase systems involves many modes of stress distribution. The normal shear behavior of the solvent occurs along with unique behavior of the solid, including agglomeration and break up of aggregates, and the rotations of suspended particles in many directions. The simplest solution to these effects is to introduce an effective viscosity into the Newtonian equation and the velocity and stress quantities are averaged over a large volume.

Einstein started the study of the viscosity of suspensions by looking only at spheres that are so dilute that the movement of fluid around a single sphere does not affect the fluid around any other sphere. These additive fluid responses are shown in the Einstein equation:

$$\frac{\mu_{eff}}{\mu_0} = 1 + \frac{5}{2}\phi \qquad (5.1)$$

where μ_{eff} is the effective viscosity, μ_0 is the viscosity of the solvent alone, and ϕ is the volume fraction of particles.

As the need for specific solutions arose many modifications have been made to this equation. The study of suspensions of nonspherical particles has introduced shape

factors to replace the constant 5/2. However, when the particles, even when the suspension is dilute, have high aspect ratios and are flexible, non-Newtonian behavior occurs. Concentrated solutions have also brought modifications to the Einstein equation. The Kreiger-Doughtery equation has been used to describe the rheological behaviors of concentrated nonspherical particle suspensions:

$$\frac{\mu_{eff}}{\mu_0} = \left(1 - \frac{\phi}{\phi_{max}}\right)^{-A\phi_{max}}$$

Here A and ϕ_{max} are experimental values. [1] In experimental circumstances it is more practical to use the measure the low and high shear limit viscosities to asses the viscosity of the solution. This is done with the Cross equations, which uses viscosity as a function of the shear rate.

$$\mu(\dot{\gamma}) = \mu_\infty + \frac{\mu_0 + \mu_\infty}{1 + \left(\frac{\dot{\gamma}}{\dot{\gamma}_c}\right)^m} \tag{5.3}$$

In this equation the viscosity at the low and shear rate limits are used, μ_0 and μ_∞, respecitively, along with the shear rate, $\dot{\gamma}$, and two constants, $\dot{\gamma}_c$ and m. For polymers:

$$m = \left(\frac{\bar{M}_n}{\bar{M}_w}\right)^{\frac{1}{5}} \tag{5.4}$$

$$\dot{\gamma}_c = \left(\frac{k_e}{k_d}\right)^{1/m} \tau_s^{-1} \tag{5.5}$$

The m term uses the ratio of $\bar{M}_n$, the number average molecular weight, to $\bar{M}_w$, the weight average molecular weight of the suspended particles. The $\dot{\gamma}_c$ term relates this ratio and the ratio of k_e, the rate constant of entanglement, to k_d, the rate constant of disentanglement. τ_s^{-1} is the characteristic time constant for the rate of segment diffusion.

[2] The cross equation is also a good representation of slurry rheology, but $\dot{\gamma}_c$ and m have a different meaning.

The Cross equation is also written with respect to the translational Peclet number, such that:

$$\mu(\dot{\gamma}) = \mu_\infty + \frac{\mu_0 + \mu_\infty}{1 + \frac{Pe_t}{8}} \tag{5.6}$$

Experimental testing of the Cross equation in suspensions of hard spheres with varied volume fractions, ϕ, has led to the development of the following best fit equations for the low and high shear rate asymptotes of viscosity:

$$\frac{\mu_0}{\mu_s} = 1 + 2.5\phi + 4\phi^2 + 42\phi^3 + \cdots \approx \left(1 - \frac{\phi}{0.63}\right)^{-2} \tag{5.7}$$

$$\frac{\mu_\infty}{\mu_s} = 1 + 2.5\phi + 4\phi^2 + 25\phi^3 + \cdots \approx \left(1 - \frac{\phi}{0.71}\right)^{-2} \tag{5.8}$$

Looking at these equations the volume fraction for the low shear limit is in accordance with the maximum volume fraction in random close packing, 0.63. For the high shear limit the maximum volume fraction is a bit higher suggesting hexagonal packing, 0.71. This is very similar to Equation 5.2. This relationship is only true for hard spheres, a small modification is made to use this relationship to describe nonspherical particles. Testing of such particles shows that the maximum volume fraction is much lower than that for the spherical particle, such that

$$\phi_{max,ns} = \phi_{max} * \left(\frac{b}{a}\right) \tag{5.9}$$

where $\left(\frac{b}{a}\right)$ is the aspect ratio for the particle. The idea being that a nonspherical particle will rotate in shear. This gives an effective sphere of rotation with this new volume

fraction. In carbon nanotube studies, the aspect ratio, $\frac{b}{a}$, is a quantity that speaks to their quality as material toughner additives. This measurement is critical in finding the essential properties of CNT material.

Testing the viscosity of suspended particles with an increasing volume fraction will allow us to find the maximum volume fraction. Then using the hard sphere relationship we can find the aspect ratio. The zero viscosity and the infinite viscosities can both be used, which gives an immediate measure of variability in the $\frac{b}{a}$ parameter.

$$\frac{\mu_0}{\mu_s} = \left(1 - \frac{\phi}{0.63 * \left(\frac{b}{a}\right)}\right)^{-2} \tag{5.10}$$

$$\frac{\mu_\infty}{\mu_s} = \left(1 - \frac{\phi}{0.71 * \left(\frac{b}{a}\right)}\right)^{-2} \tag{5.11}$$

The combination of the infinite and zero viscosities as a function of viscosity should result in a divergence as the numerator approaches the denominator. The volume fractions are adjusted by a factor of $\frac{b}{a}$. So for a sample that has an aspect ratio of 45, the graph, shown in Figure 34, shows these divergences occuring at 0.0147 for the zero viscosity and 0.0153 for the infinite viscosity.

Method

To measure the high and low viscosity limits a rotational cylinder rheometer was used, specifically the Discovery Hybrid Rheometer from TA instruments with a Peltier concentric cylinder. In this system the fluid sits in the annulus of two cylinders. The inner cylinder spins at a set rate or a set stress as necessary with the outer cylinder being

stationary and the force applied is monitored. To avoid any discrepancies that would arise from increasing the temperature of the fluid a Peltier cooling system is used. This keeps the temperature at 25 °C. The method used is in accordance with ASTM D2556. The viscosity was tested by holding a shear rate of 1000 s^{-1} for 180 seconds. Then a logarithmic sweep down to 0.1 s^{-1} was performed. Each sample was tested three times to increase the reliability of the data. Due to the large amount of sample needed to make the solutions, only two types of carbon material were able to be tested, pet coke and an industrial MWNT sample labeled PolyOne3.

Carbon nanotubes are hydrophobic, so there were necessary preprocessing steps to get the solids suspended into a liquid solution. A 2% DBA solution was used for this testing due to results from other testing to get CNTs into suspension. An ultrasonic probe was used to mix the solution. The power to the probe was determined by testing the DBA solution alone and seeing how much sonication was needed to produce a milky white solution, which shows the presences of misceles needed to surround and stabilize the CNT suspension. Ultrasonication has been shown to have adverse effects on the structure of the CNTs themselves so the minimum amount of sonication is needed to have little damage on the solids. [3]

Results

The compiled viscosity measurements are shown in Figures 35 and 36. The pet coke sample shows no change in the zero rate viscosity as the volume fraction increases. With the inclusion of the errors in the infinite rate viscosity, there is little to no change in that measurement with increasing volume fraction as well.

The orange lines show the infinite rate viscosity and the blue lines show the 0 rate viscosity. The pet coke samples show a very smooth 0 rate viscosity at around $7 * 10^{-4}$ Pa*s, while the infinite rate viscosity looks like it is around $4 * 10^{-3}$ Pa*s. The PolyOne3 samples have a larger distribution of viscosities with no obvious trend. In order to get the data at the divergence point, larger concentrations are necessary. PolyOne samples were tested at higher concentrations with the results shown in Figure 37.

Here there is a large increase in the 0 rate viscosity at the 0.015 volume fraction followed by a decrease in the viscosity at a volume fraction of 0.021. This decrease has a very large uncertainty and it is unclear whether the maximum volume fraction has been reached or not.

Conclusions

The method of suspension for this test limits us to a maximum volume fraction of 0.021. If the viscosity diverged at this point it would mean that the aspect ratio would be 30 for the PolyOne3 sample. However, with the uncertainty seen in the figure the point of divergence is unclear. To ensure a viable measure of the aspect ratio, the solids must be able to be suspended at a higher volume fraction. Unfortunately the solvent that was used for these samples will not allow for a large enough volume fraction of solids in solution. The geometry of the cup is such that if the solids settle then the measurement will be of an unknown reduced level. So the data may be more unpredictable. This may also be the case for the large errors in the PolyOne3 solution. If there is not a consistent concentration in the solution then the viscosity data will vary.

Carbon nanotubes are highly hydrophobic. The solvent used in this trial was a

2% DBA in water solution. The theory being that a molecule that had a polar end and a nonpolar end would form miscelles around the solid when undergoing ultra sonification. However, it has been shown that the use of ultrasound mixing of CNT material damages the CNT themselves. [3] An alternative path could involve using an oil based solvent for this test and minimal sonification or just using a stir rod. Once the divergence point can be found then further analysis can be performed to determine whether this type of testing is valid in determining the aspect ratio of carbon nanotubes.

CNT suspension has been achieved in an epoxy resin by the Graphistrength company. Their research into viscosity changes with increased volume fraction yields a more expected result, as seen in Figure 38. [4] This image shows the expected increase in viscosity as the volume fraction increases signifying a high dispersion of the CNT material in the suspension.

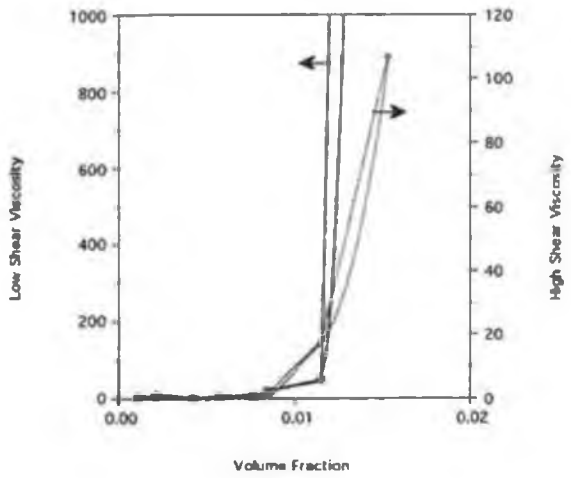

Figure 34: Divergent viscosity measurements as a function of volume fraction for hectorite platelets with an aspect ratio of 45. Modified from ref. 2.

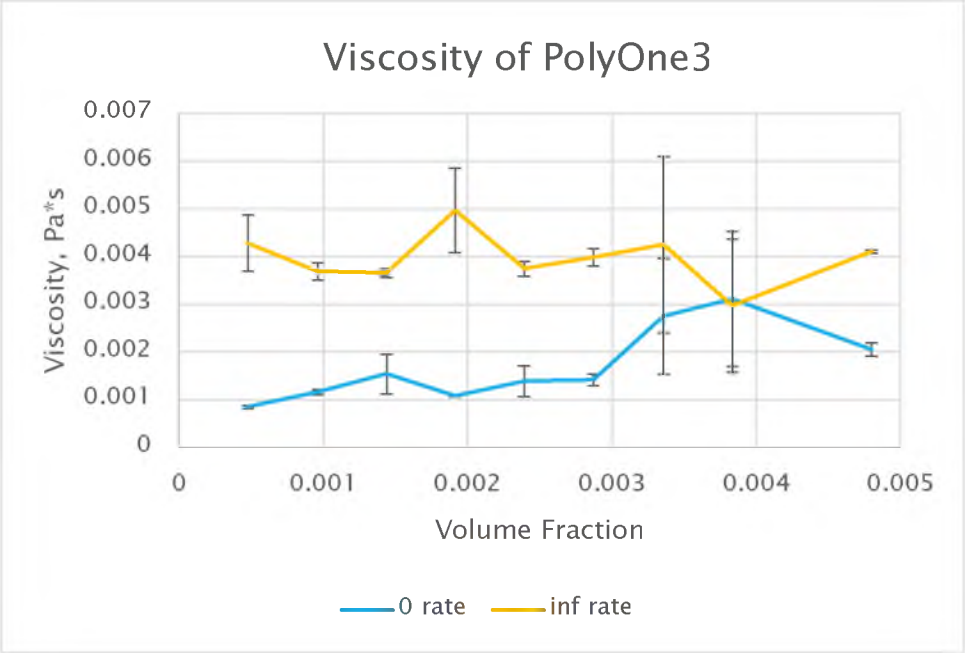

Figure 35: Viscosity as a function of volume fraction for PolyOne3.

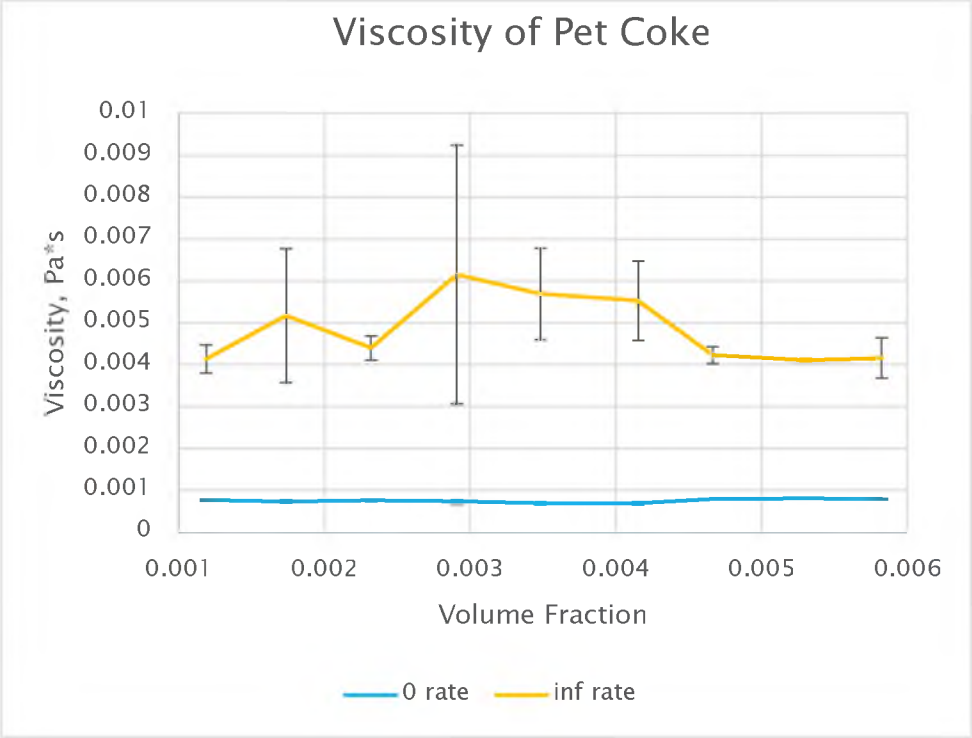

Figure 36: Viscosity as a function of volume fraction for pet coke.

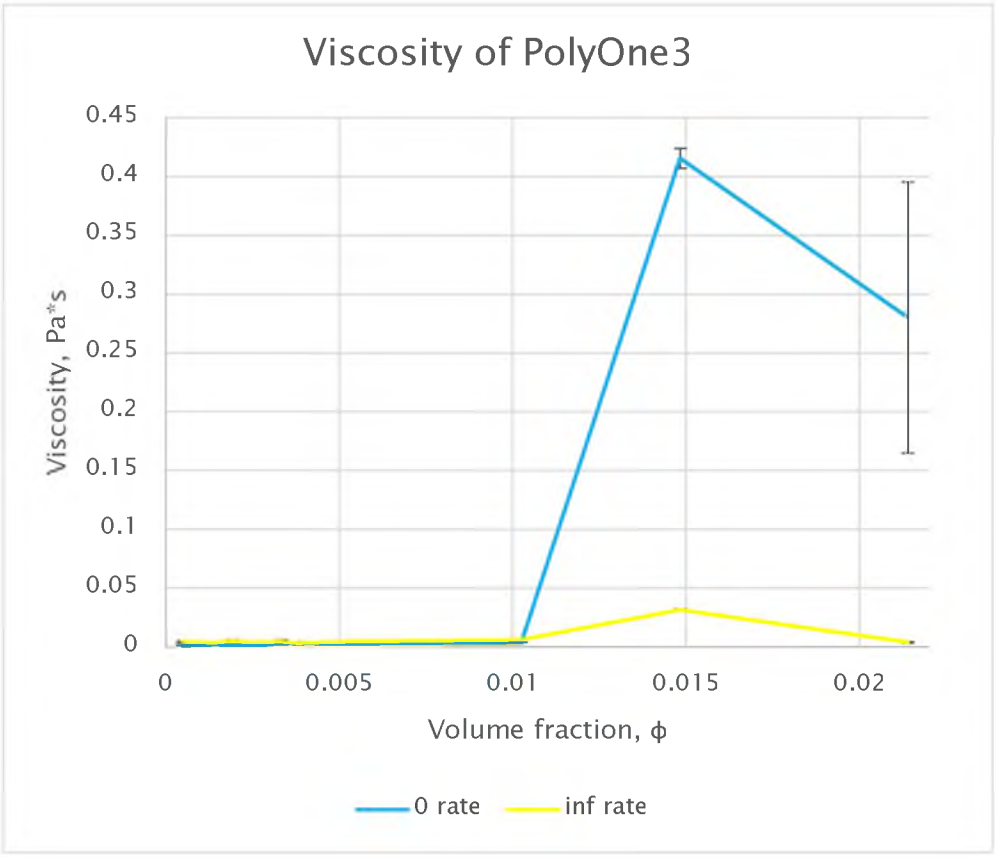

Figure 37: Viscosity as a function of volume fraction at high concentrations for PolyOne3.

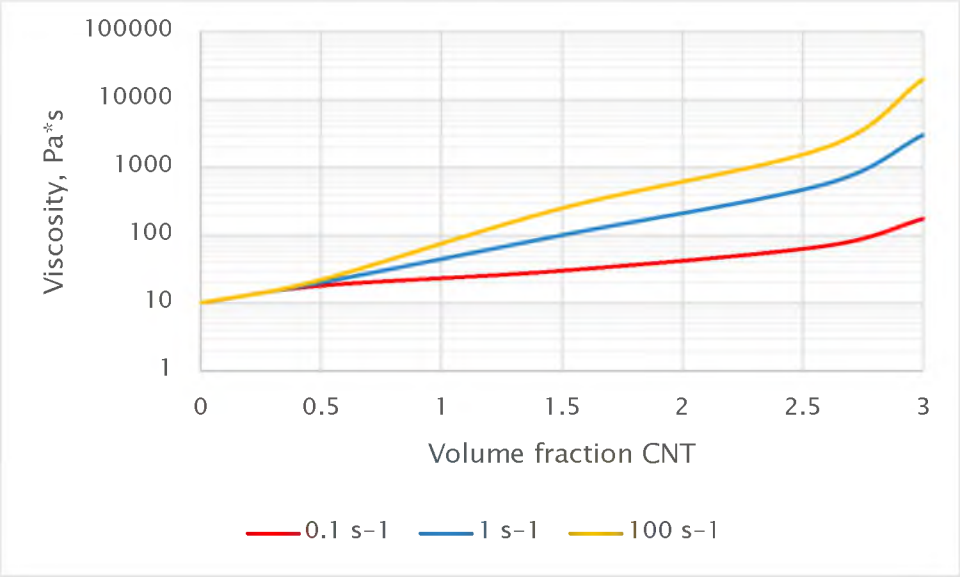

Figure 38: Viscosity as a function of volume fraction for CNT in an epoxy resin, data from ref. 4.

References

[1] R. B. Bird, W. E. Stewart and E. N. Lightfoot, Transport Phenomena, 2nd ed., New York City: John Wiley & Sons, Inc, 2007.

[2] T. A. Ring, Fundamentals of Ceramic Powder Processing and Synthesis, San Diego: Academic Press, Inc., 1996.

[3] K. Lu, R. M. Lago, Y. K. Chen, M. L. H. Green, P. J. F. Harris and S. Tsang, "Mechanical damage of carbon nanotubes by ultrasound," *Carbon,* vol. 34, no. 6, pp. 814-816, 1996.

[4] S. Bordere, J. Corpart, N. El Bounia, P. Gaillard, N. Passade-Boupat, P. Piccione and D. Plée, "Industrial production and application of carbon nanotubes," Akema, Lacq, 2007.

CHAPTER VI

SPECTROSCOPY

Overview

Spectroscopy studies bonding of materials by measuring how they respond to different sources of energy. The response of the molecule depends on its structure and the relationship of the structures to particular wavelengths of light. There are many types of spectroscopy available. For this study we will look at the spectrum of carbon species with Raman spectroscopy and Fourier transform infrared spectroscopy.

Raman spectroscopy shows the bonding structures in molecules by sending a laser of a specific wavelength of light into the sample. The energy in these photons excites both phonons and electrons into higher energy states. After being launched to this higher virtual energy state, the electrons then release the energy and transmit a signal as they transition to a lower energy state. The energy is released through different mechanisms. The Raman scattering results in a signal shift which is measured through a sensor and relayed as peaks on a Raman spectra. Figure 39 shows an energy diagram of this process. The IR band shows that infrared energy will excite an electron from E_0 to $E_{0,1}$. The next series, R, is the Rayleigh scattering. This scattering excites electrons to the higher virtual energy level, then the electron releases the same energy resulting in the electron returning to its previous position at E_0. The light absorbed is of the same energy of light emitted.

The next two series show the Raman scattering. These are labeled S and A for Stokes and anti-Stokes scattering. In Stokes scattering the electron is exciting from the ground level to the excited energy state then returns at a slightly higher energy state giving off light of a lower energy. Similarly, the anti-Stokes scattering takes an electron at the slightly elevated energy level and excites it further to the higher excited energy level. This electron then releases not only the energy that was used to elevate it to the excited energy level but also the energy it had in its previous state. So the electron moves all of the way down to the ground state giving off light with more energy than the incident light. Because the Raman scattering occurs far less often than Raleigh scattering, the intensity of this scattering has typically no more than 0.01% of the energy of the incident beam. [3]

This vibrational spectroscopy will give insight into how the added energy effects the molecule by stretching and bending bonds. In order for the energy to be shifted so that it is Raman active the polarizability of a molecule must be changed by the energy transfer from the photon to the phonon. [2] This means that the electron cloud surrounding the molecule is distorted as a result of the vibration. Polarizability is a proportionality constant that relates the induced dipole moment to the magnitude of the electric field. Polarizability is also dependent on the direction of the field relative to the molecular axes, [4] and the bond length. This is seen in stretching vibration modes where the electron cloud is effected even if the dipole moment is constant as in symmetric stretching. To show these different types of stretching, Figure 40 shows the tetrahedral stretching modes seen in methane. All of these modes are Raman active. The symmetric stretch shown in A_1 keeps the same dipole moment but will be Raman active due to the

change in the shape of the surrounding electron cloud resulting in an altered polarizability and a change in bond length. The triply degenerate modes, T_2, will produce a change in dipole moment and a changes in polarizaiblity. These are both IR active and Raman active bending modes.

When taking the Raman spectrum of carbon structures, there are two main bands that appear. They are labeled G and D bands and typically occur at 1580 cm^{-1} and 1350 cm^{-1}, respectively. The G band gets its name from graphite like structures. This mode is caused by the stretching of the sp^2 bonds in carbon rings or chains. In ring structures, the D band is a disorder band. It is seen in rings with graphitic sp^2 bonding. Figure 41 shows what these modes look like.

The peaks of common carbon types are summarized in Table 7. The use of Raman spectroscopy in the field of carbon classification is so common that many of the prominent peaks have been given the common names, G, D, and G'.

The peak seen at 150 cm^{-1} in the SWNT is due to a radial breathing mode (RBM) found in nanotubes. This excitation is the result of the tube stretching and compacting radially. These peaks are only seen when there are SWNT present. In the MWNT, this mode is stifled because the walls are thicker and less susceptible to expansion. RBMs can show the distribution of diameters in the SWNT samples.

The D band is amplified with the diamond type bonding notably having sp^3 bonding present since these bonds are disorder to the sp^2 carbon bonding seen in carbon rings. When a D band is present in other carbon species, it infers that there is damage in the ring structure. The ratio of the D and G bands is used for bond analysis as discussed later in this work.

The G band is a first order Raman feature that is seen for all sp^2 carbon bonds. The energy is related to the vibration of the carbon-carbon bond. Multiple G peaks are seen in SWNT due to the diameter and chirality of the tube. In MWNT this phenomena does not exist; the G is the same as it is in graphite with a single peak at 1580 cm^{-1}.

The G' band is linked to second-order scattering from the D band. It is present with or without defects to the structure in graphite, graphene, and nanotube species. The excitation seen with the G' band involves the energy of the phonons along the structure's length. This peak can be broadened due to two peaks combining if the laser energy closely matches the electronic structure of the carbon species. Amorphous carbon in mixtures with other carbon species will broaden the peaks, resulting in a smoother and wider spectra.

Fourier transform infrared spectroscopy (FTIR) uses an infrared spectrum to collect spectral data simultaneously over a wide range using the mathematical process of the Fourier transform to convert the data into an actual spectrum. The absorption works in the same manner as in the Raman spectroscopy where a light signal is transmitted to a sample and a meter monitors how much of that light is reflected and how much is absorbed at different wavelengths. In this particular spectroscopy method, instead of shining one wavelength at a time an entire range of wavelengths are sent to the sample at the same time. The signal is then analyzed. After analysis, the beam is modified to have a different series of wavelengths and a second data point is produced. This is repeated and then a backwards iteration is performed. [4]

For a vibrational mode to be Raman active, the vibration must lead to a change in polarizability. In contrast, the FTIR activity is produced when the light results in a

vibrational mode that changed the dipole moment of the molecule. Thus, while the symmetric vibration modes will be strongly seen in the Raman spectroscopy the FTIR spectroscopy will see asymmetrical vibrational modes and the vibrations due to polar groups.

Method

The Raman spectrometer used for this trial was a Witec Raman spectrometer, alpha300SNOM scanning near field optical microscopy. The spectroscopy was done with a 20X objective microscope lens. A 532 nm laser line with a 10 second CCD integration time was used for these tests. To calibrate the device, a silicon disk was placed on a glass slide and the spectra was taken. Silicon has a known single peak Raman spectra. To adjust for the offset due to environmental conditions and alignment the amount that the silicon reading alters from where the known peak occurs is subtracted from the experimental readings. For these tests is was determined that the spectrometer performed 42 wavenumbers above this standard. The data were then adjusted.

The tests were performed on unaltered powders. A small scoop of powder was placed on a clean glass slide. After the alignment and calibrations readings were taken, Raman spectra was performed on all of the various carbon bonded materials available.

The FTIR spectrometer used for this trial was the Bio-Rad FTS 6000 Spectrometer. The testing was performed by Xuming Wang with the Department of Metallurgical Engineering at the University of Utah. The range used was 500 to 4000 cm^{-1}, with a resolution of 4 cm^{-1}. The calibration scans were done using CO as the basis. From this calibration the spectra was adjusted 500 cm^{-1}.

Results

In order to determine the special bonding conditions of CNT material, Raman testing was performed on all of the different carbon structures described in the material section. FTIR was performed on these samples as well. The Raman spectra requires no further analysis once the offset is corrected. FTIR will show peaks on a sloped line. This baseline is subtracted from the raw data. The baselines are typically linear, however, non-linear baselines are used as well. Peaks between 500 cm^{-1} and 1500 cm^{-1} are usually ignored. These are the in the fingerprint region and have large baseline anomalies.

Industrial Samples

Pet Coke

The pet coke sample spectroscopy is shown in Figures 42 and 43. This sample shows a lot of noise associated with a weak signal strength. The D and G peaks are seen at 1331 and 1582, respectively. The G' peak is also shown at 2671 cm-1. The G' band is very broad. The G/D ratio is 1.125 and the G/G' ratio is 2.25. The FTIR spectra shows a double peak at 2300 and 2359 cm^{-1}. There is another small peak seen at 2940 cm^{-1}. The Raman spectra has a similar last peak.

Graphene

The graphene sample shows a similar Raman spectra in Figure 44. In the Raman spectra the D peak is larger than the G peak. The G/D is 0.904 and G/G' is 1.58. The G' peak is again broadened spanning around 400cm^{-1}. These two samples show how industrial samples can show many impurities. The weak signals and the broad peaks

make the analysis of these samples more difficult. The FTIR spectra (Figure 45) shows a small peak at 2351 cm^{-1} and a broader double peak at 3620 and 3688 cm^{-1}.

Single and Double Walled Nanotubes

When we compare these previous samples to a sample that contains high purity single and double walled nanotubes, the Raman spectra is very clear and strong seen in Figure 46. In the Raman spectra the first notable bands are at 154 and 265 cm^{-1}. These are the bands that correspond to the radial breathing modes of the carbon nanotubes. These are seen only in samples with few walled nanotubes because multiple walled nanotubes inhibit this vibration. The G peak signal is largely amplified showing a G/D ratio of 11.49, and a G/G' ratio of 2.27. The addition of multiple layers of graphene to the tube will stifle the bending vibrations that occur in tubes with thin walls. The G' peak shows a small amount of broadening on the left hand side of about 100 cm^{-1}. This is indicative of two or more peaks at about the same wavelength so they are combined to form one peak. This signifies that the sheets are not purely single walled. The number of walls will determine the number of peaks that are combined under the G' peak. These peaks can be deconstructed using the Origin 8.6.0 software. This shows that this peak is a combination of two peaks, one at 2596 cm^{-1} and the second at 2655 cm^{-1}. This analysis is shown in Figure 47.

The FTIR spectra, Figure 48, shows the double peak at 2334 cm^{-1} and 2367 cm^{-1}. There is a slight peak at 2967 cm^{-1} and two peaks in the upper range of wavenumbers 3742 cm^{-1} and 3852 cm^{-1}. There is a large noise to signal ratio in the FTIR spectra compared to the Raman spectra of the same sample.

Multiwalled Carbon Nanotubes

The ratios are altered with this bonding structure. The Raman spectra is seen in Figure 49. The G/D ratio is 2.26 while the G/G' ratio is 0.71. The RBM bands are almost entirely missing, as seen at 117cm^{-1}. This is expected for multiwalled samples. The FTIR shows the double peak at 2334 and 2359 cm^{-1}, which was seen in the SW/DWNT spectra, along with two peaks at 2872 and 2967 cm^{-1}. There is a broad peak at 3395 cm^{-1} which correlates with graphene peaks seen in Figure 50.

Industrial samples from the pilot plant were also tested. An FTIR spectra was performed on C-001 and is shown in Figure 51. There exists the indicative double peak at 2332 and 2361 cm^{-1}, along with a cluster of peaks at 2857, 2932, and 2961 cm^{-1} and two final peaks at 3742 and 3852 cm^{-1}. C-001 and two other production samples were tested with the Raman spectroscopy and are shown in Figures 52 through 54.

These industrial samples show a mixture of carbon structures due to the nature of bulk production. Table 8 shows a summary of the peak locations for these three samples. Ferrari and Prawer in a study of amorphous carbon developed a model in Figure 55 to classify the bonding structures. As you move from left to right, you go through different carbon bonds. The first stage moves from graphite to a nanocrystalline (NC) graphite. Stage 2 moves to an sp^2 bonded amorphous carbon, a-C, and stage 3 moves to the tetrahedral carbon bonding seen in diamonds, ta-C, with the sp^3 hybridization. The left hand side shows the position of the G band and the ratio of the D and G band intensities. This analysis clearly puts the C-002 and C-003 samples at the NC graphite stage with the G position near 1600 cm^{-1} and the I(D)/I(G) ratio at or near 2.0. The C-001 sample does not reflect any of these states. The G peak is similar to the tetrahedral carbon but the

I(D)/I(G) ratio is much larger indicating more sp^2 hybridization.

Tuinstra and Koenig developed an equation that relates the I(D)/I(G) ratio to a length scale with dependence on the wavelength of the laser used for Raman measurements. This length scale speaks to the aspect ratio of the graphene sheets in the sample.

$$L_a(nm) = \frac{560}{E_{laser}^4}\left(\frac{I_D}{I_G}\right)^{-1} = (2.4 * 10^{-10})\lambda_{laser}^4\left(\frac{I_D}{I_G}\right)^{-1} \qquad (6.1)$$

The Raman spectra produced here were done with a wavelength of 532 nm. The length scales can then be found for the production samples, C-001, C-002 and C-003, compared to the other carbon species as seen in Table 9. The comparison of sample C-001 with the graphene sample shows similar ratios, however, the other production samples do not seem to correlate to any of the carbon species tested.

The ratio of the G band and the D band can signify the level of disorder, to compare these values see Table 10. The D peak shows a combination of an inelastic and elastic stretching. This peak is indicative of sp^3 bonding, meaning that the carbon has lost its sp^2 stabilized bonding that occurs in the nanotube and has picked up another atom outside of the tube structure. The G band is indicative of the C-C stretching in the graphite structure, shown in Figure 41.

For the FTIR data only the peak position can be compared. Since every sample will have a unique baseline, dependent on how much of the energy is stored, a summary of the peaks are shown in Table 11. The number of peaks and their locations are similar for all species, but there is no underlying trend or conclusions that are clear from the FTIR data alone.

Conclusions

Raman scattering is a useful method to determine the carbon bonding in a powder sample. Through analyzing the peak wavelengths and the ratios of intensities, a picture of the structure of each sample is developed. Raman peaks at 1580 cm^{-1} and 1330 cm^{-1}; the G and D band, respectively, show the degree to which the carbon rings are complete. Single walled and double walled nanotubes are clearly seen with Raman peaks at wavelengths under 300 cm^{-1}, showing the radial breathing modes.

Further analysis can provide a length scale that is related to the aspect ratio of the carbon species. While these data are instructive, Raman alone can not distinguish between all carbon species or test all nanotube characteristics. FTIR spectroscopy is less useful. Although some peaks are clear, the noise and the baseline level make knowing where the peak is and the intensity of the peak difficult to analyze.

Table 7: Raman peaks for various carbon materials.

Carbon Type	Peak locations, cm^{-1}			
	RBM	D	G	G'
Diamond		1330		
Graphene			1580	2740
Graphite			1580	2720
Amorphous Carbon, Charcoal		1360	1580	
SWNT	150	1340	1580	2695
MWNT		1350	1580	2700

Table 8: Summary of Raman peaks for production samples.

Sample	**D Band**	**G Band**	**G' Band**	**D' Band**	**Overtone**	**I(D)/I(G)**	**I(G)/I(G')**
C-001	1339	1567	2688	2935	3209	1.062	0.907
C-002	1339	1587	2674	2912	3193	2.037	1.880
C-003	1343	1595	2674	2922	3193	1.732	2.292

Table 9: Intensity ratios and calculated length scales.

Sample	**I(D)/I(G)**	**L_a (nm)**
C-001	1.06	18.14
C-002	2.04	9.42
C-003	1.73	11.11
Pet Coke	0.89	21.63
Graphene	1.11	17.39
SW&DWNT	0.09	220.95
REX MWNT	0.44	43.46

Table 10: Ratios for all carbon species tested.

	G/D Ratio	G/G' Ratio
C-002	0.491	1.879
C-003	0.578	2.292
Graphene	0.904	1.583
C-001	0.942	0.036
Pet Coke	1.125	2.25
REX MWNT	2.261	0.712
SW&DW CNT	11.493	2.267

Table 11: Summary of FTIR peaks.

C-001	MWNT	SW/DWNT	Graphene	Pet Coke
2332	2334	2334	2351	2330
2361	2359	2367		2359
2857	2872			
2932	2967	2967		2940
2961				
3742	3395	3742	3620	
3852		3852	3688	

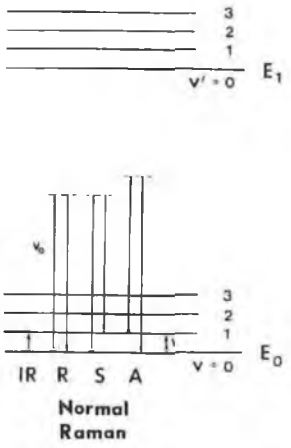

Figure 39: Diagram of Raman and IR signals showing the path in which the electrons move when excited in different states. Modified from ref. 1.

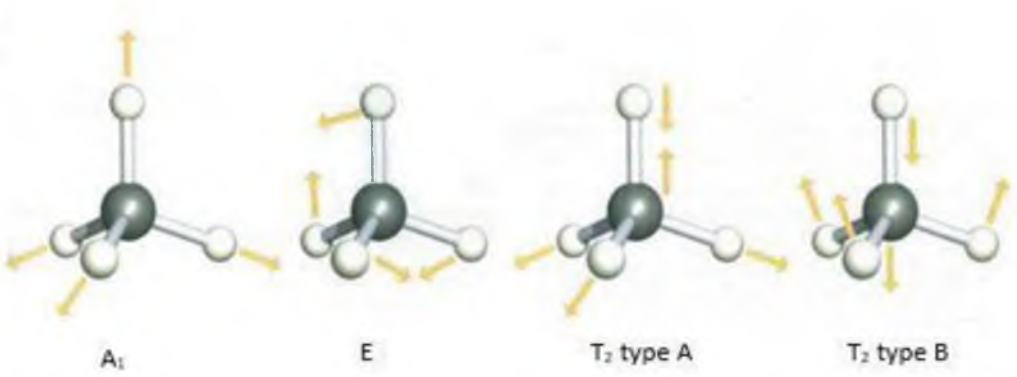

Figure 40: Model of vibrational modes that can be seen in tetrahedral bonding. Modified from ref. 2.

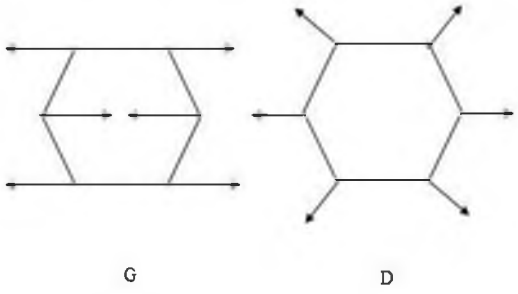

Figure 41: Vibrational modes of carbon ring structures. Modified from ref. 1.

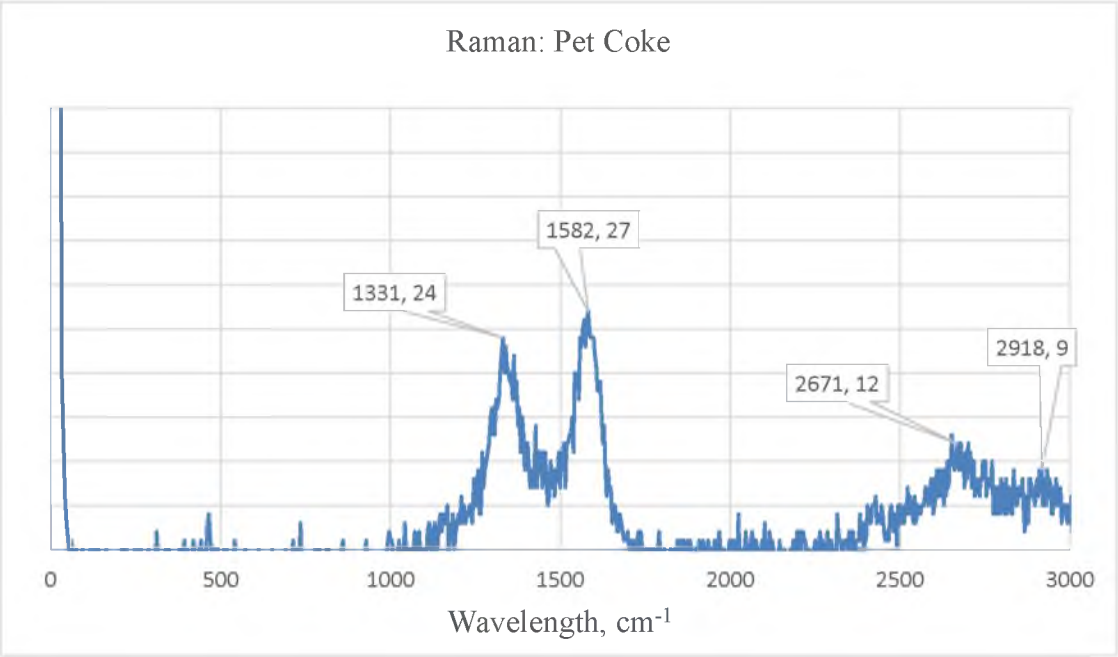

Figure 42: Raman spectra of pet coke.

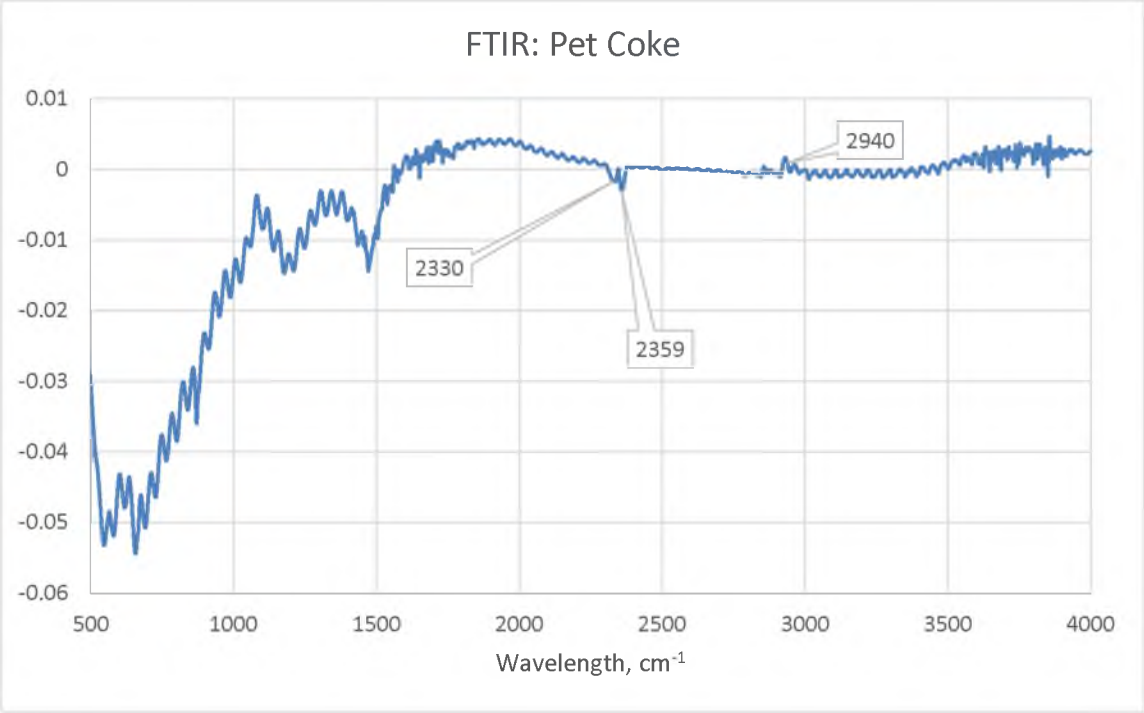

Figure 43: FTIR spectra of pet coke.

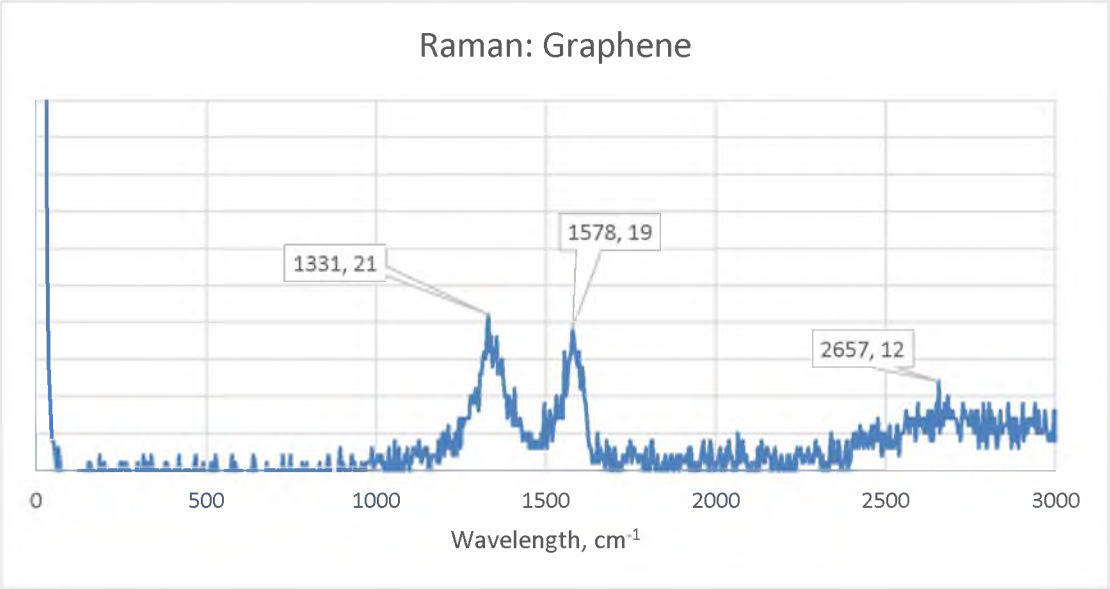

Figure 44: Raman spectra of graphene.

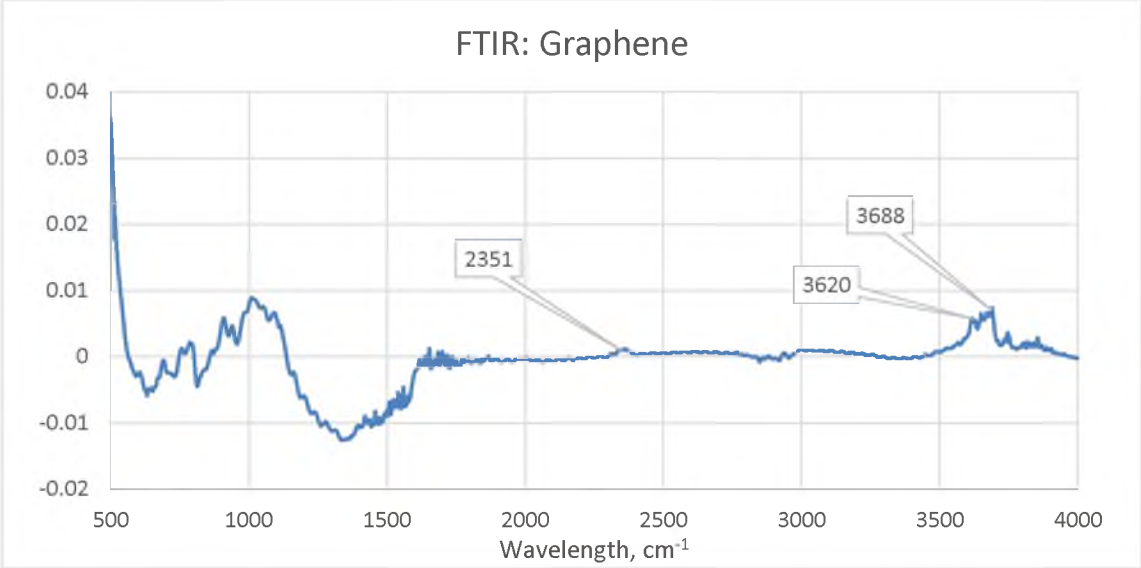

Figure 45: FTIR spectra of graphene.

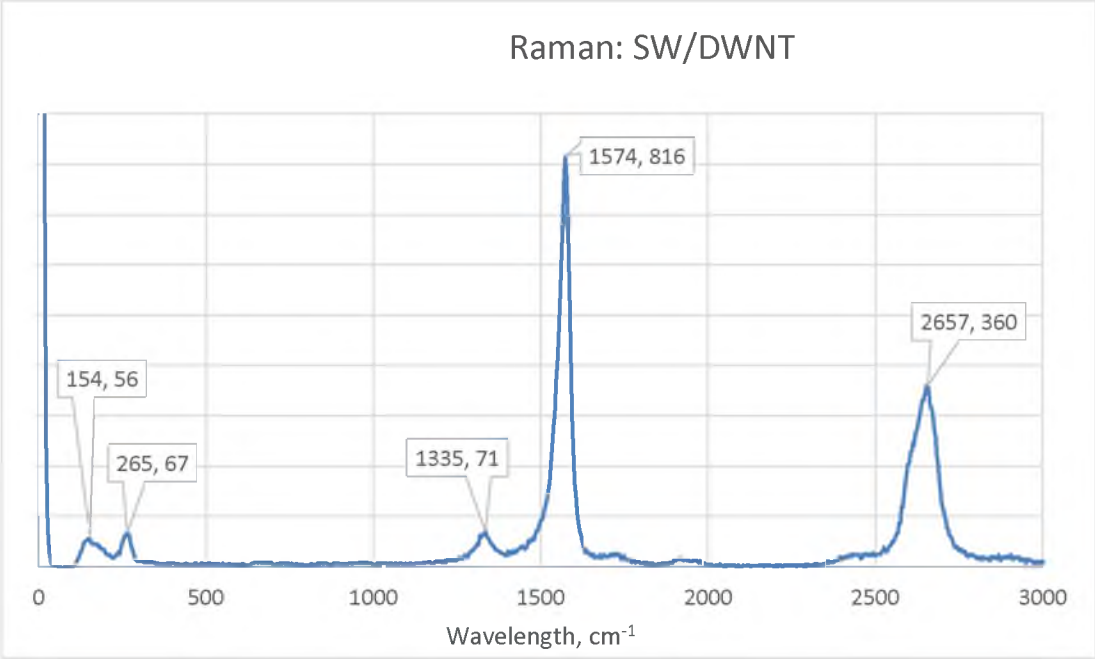

Figure 46: Raman spectra of SW/DWNT.

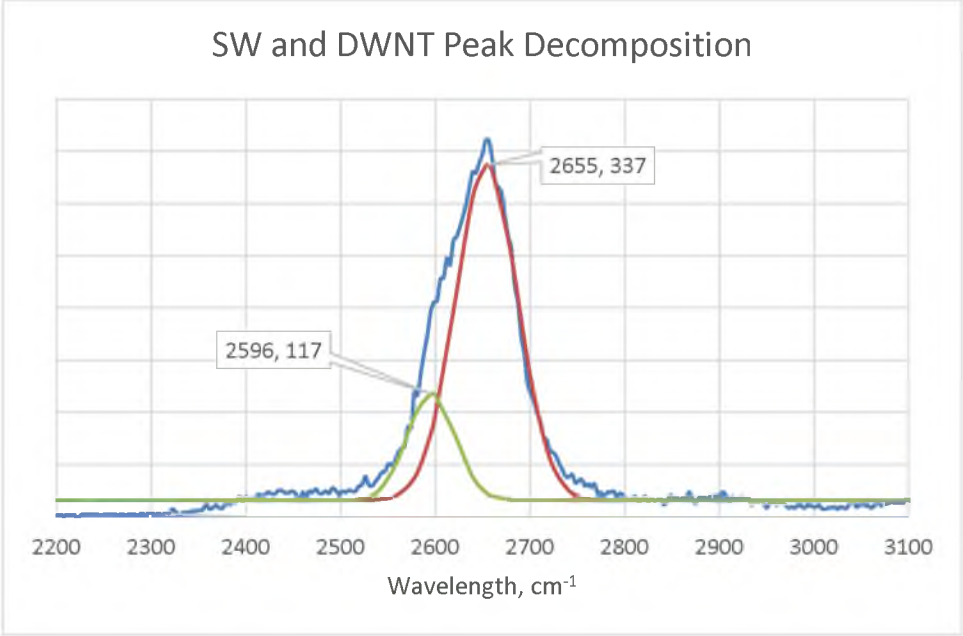

Figure 47: Peak decomposition of the last Raman peak on the SW/DWNT sample.

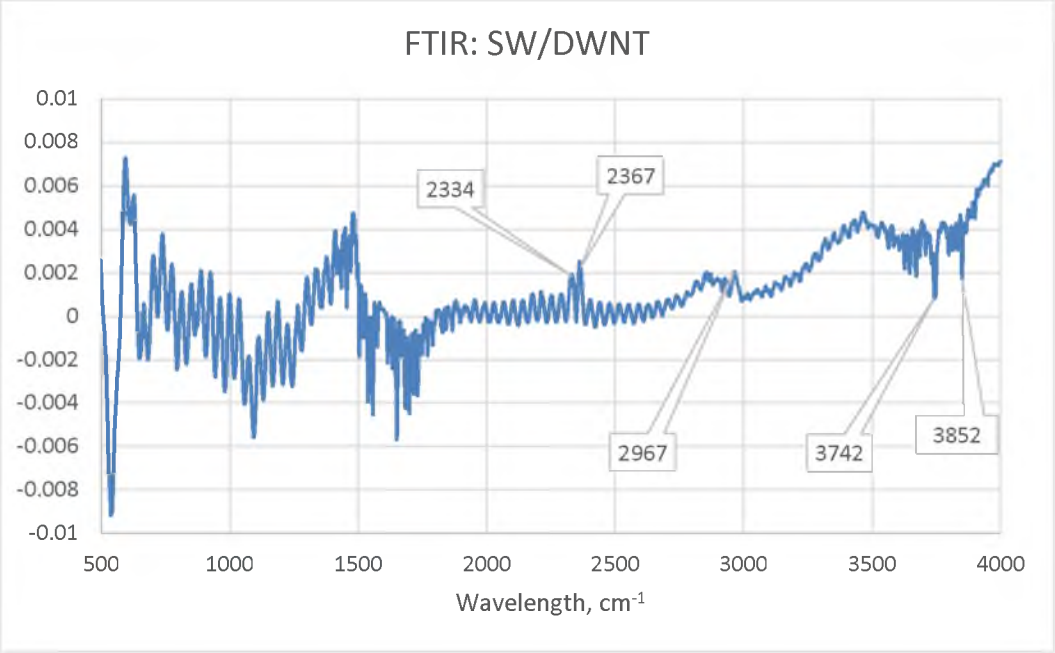

Figure 48: FTIR spectra of SW/DWNT.

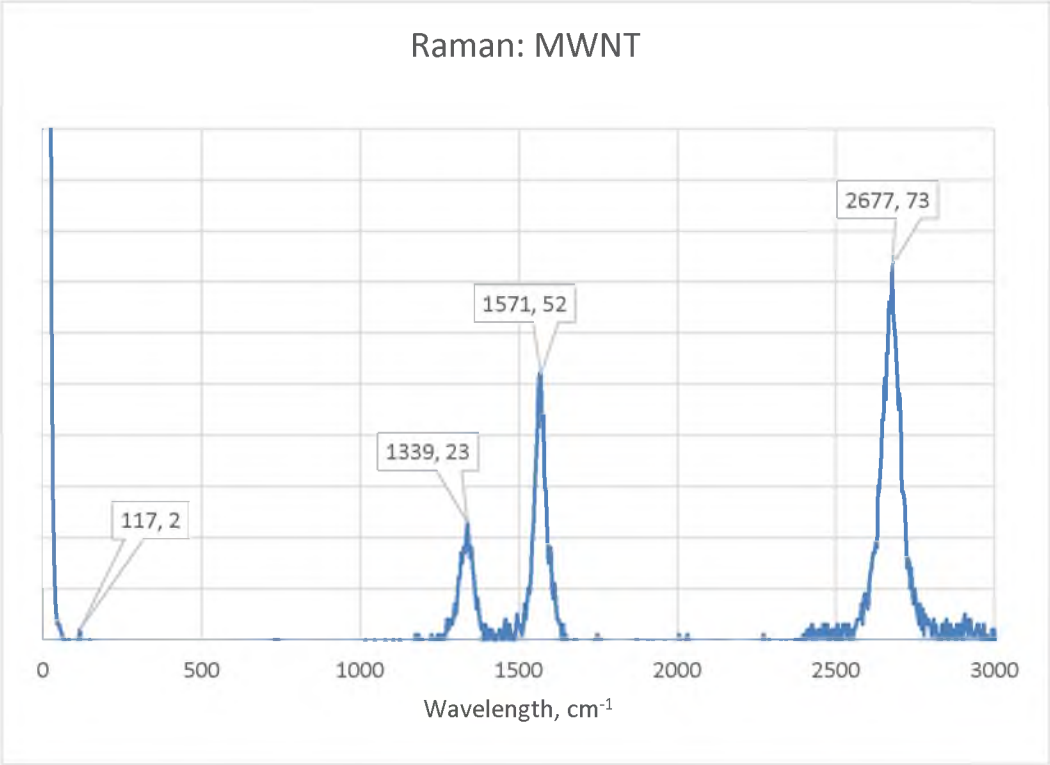

Figure 49: Raman spectra of MWNT.

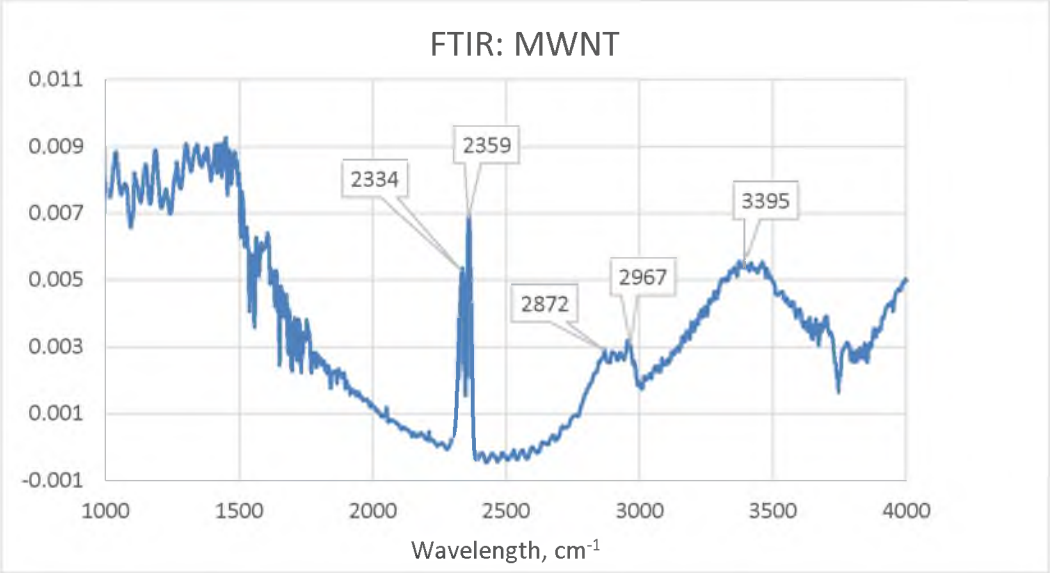

Figure 50: FTIR spectra of MWNT.

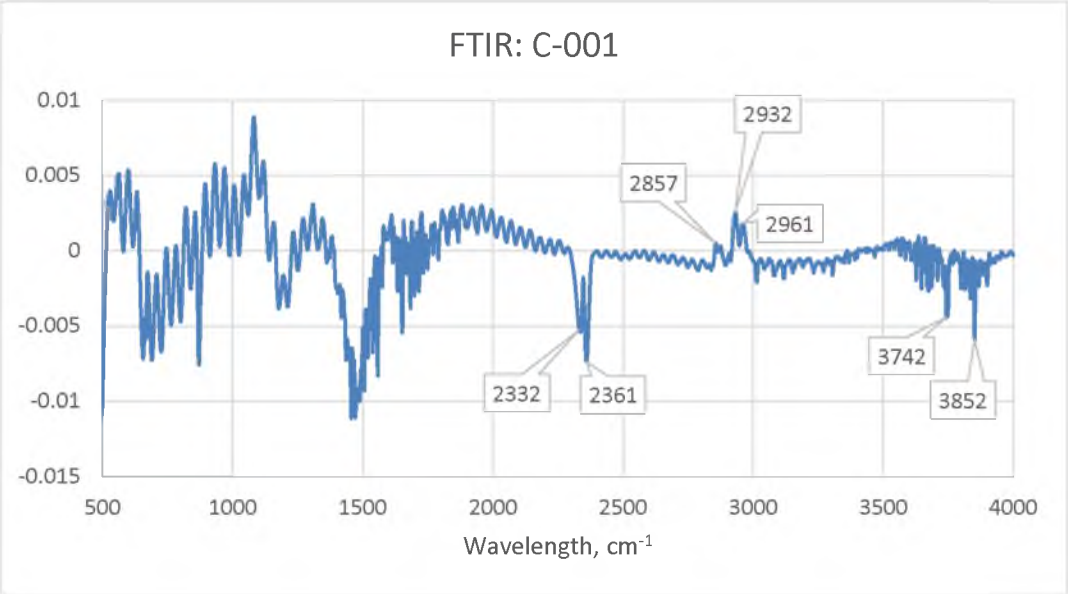

Figure 51: FTIR spectra of pilot plant sample C-001.

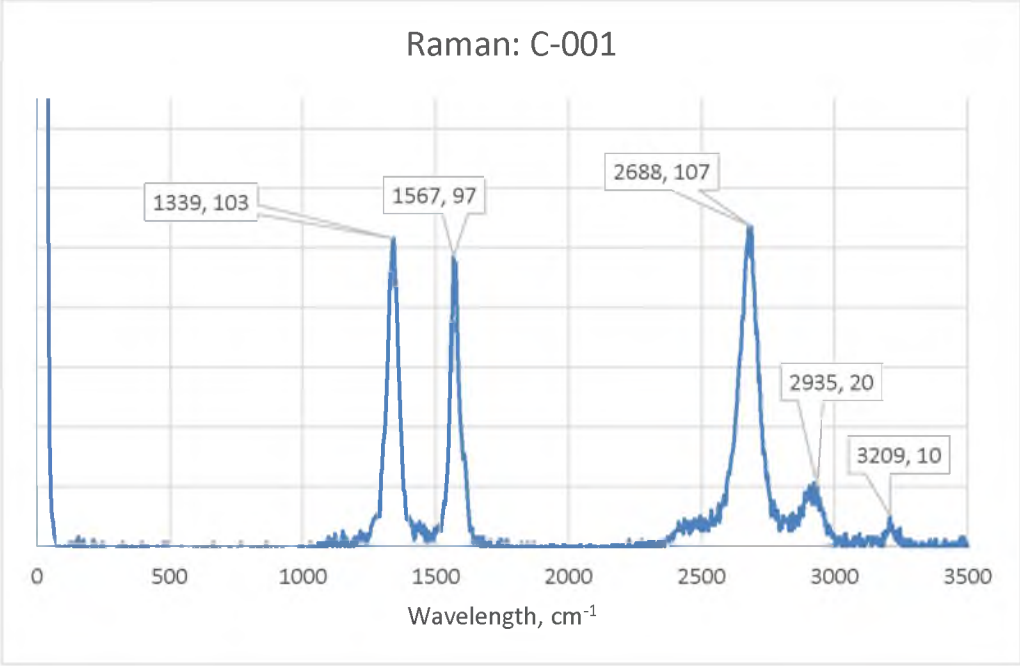

Figure 52: Raman spectra of pilot plant sample C-001.

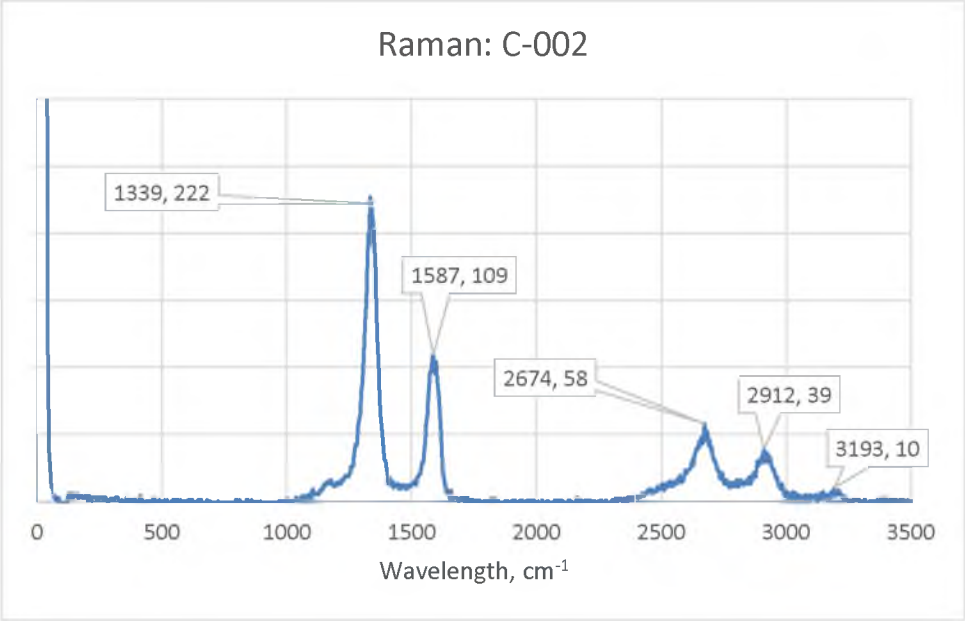

Figure 53: Raman spectra of pilot plant sample C-002.

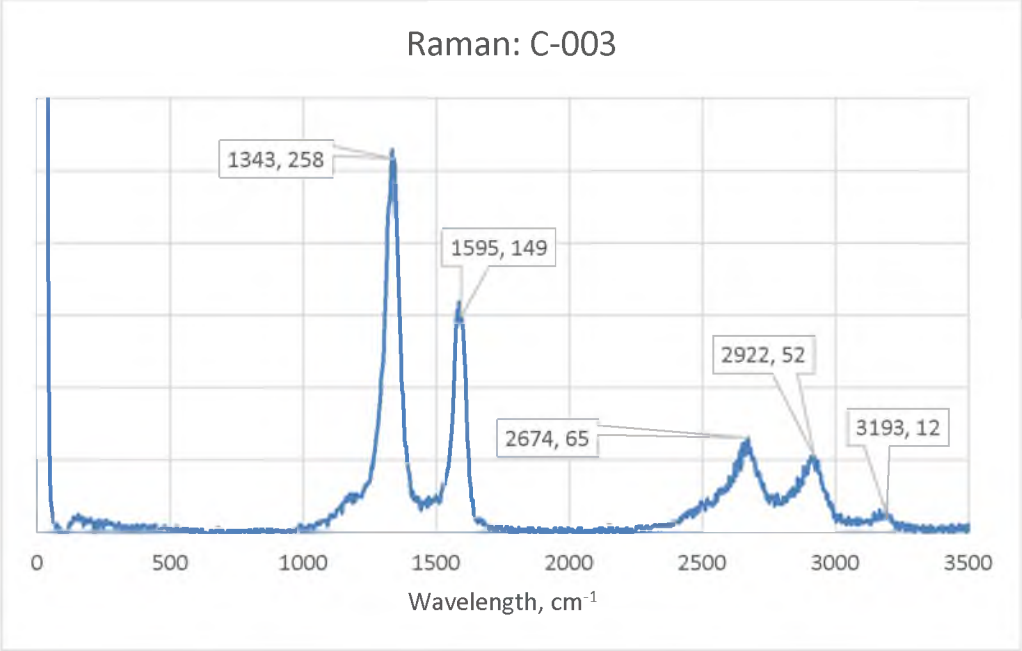

Figure 54: Raman spectra of pilot plant sample C-003.

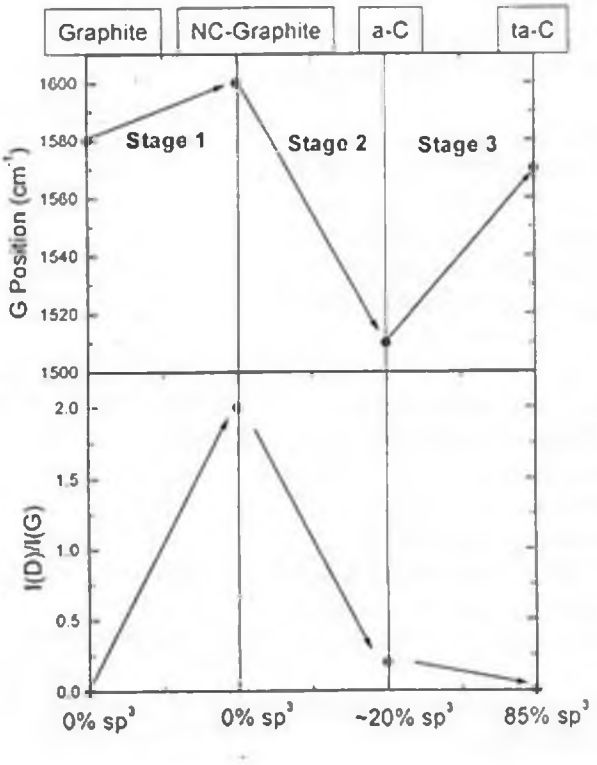

Figure 55: Bonding structures of carbon material and their relationship to the position of the G peak and the ratio of the intensity of the D and G bands, I(D)/I(G), modified from ref. 1.

References

[1] A. Ferrari and S. Prawer, "Raman spectroscopy of a-C," in *Amorphous Carbon*, London, INSPEC, 2001, pp. 46-55.

[2] C. E. H. a. A. G. Sharpe, Inorganic Chemistry, Essex: Pearson Education Limited, 2008.

[3] D. Skoog, F. Holler and T. Nieman, Principles of Instrumental Analysis, New York: Saunders College Publishing, 1997.

[4] T. Engel, Quantum Chemistry and Spectroscopy, San Francisco: Pearson Education Inc., 2006.

[5] P. R. Griffiths and J. A. de Haseth, Fourier Transform Infrared Spectrometry, Hoboken: John Wiley & Sons, Inc, 2007. T. Engel, Quantum Chemistry and Spectroscopy, San Francisco: Pearson Education Inc., 2006.

CHAPTER VII

CONCLUSIONS

Overview

The purpose of this project was to establish a set of tests that can be performed on a production site that tell us properties of carbon nanotubes that can be used for quality control and analysis. Along with these tests a set of standard samples was to be established that would allow for a basis that we can compare results from an industrial process and determine where they sit on the scale.

Standards

This study used pet coke, graphene, graphite, multiwalled carbon nanotubes and single walled carbon nanotubes. This basis allows us to judge the quality of industrial production MWNT on different scales, primarily the amount of sp^3 and sp^2 carbon bonding that is present. These standards allow us to make comparisons in order to draw conclusions about the industrial production samples. As the testing continues more standards could be added to refine the acceptable range of these products.

Test Results

Surface Area and Volume

The density and surface area of the carbon nanotubes provides data that are essential in many kinetic and transport calculations. These data were found using helium pyncometry to find the skeletal density and BET analysis to find the surface area. The skeletal density shows a how tightly the carbon atoms are bound together. This gives a measurement of the ratio of sp^3 and sp^2 bonds since the bond length for sp^2 carbon bonds is 0.142 nm while the length of sp^3 bonds are 0.154 nm. As the density increases so does the amount of sp^3 bonding. This theory is substantiated by comparing the values to those of graphene, sp^2 bonded, and diamond, sp^3 bonded. Table 12 summarizes the density and surface area data found from these experiments. This table shows that the pilot plant samples are in the same range as figures for MWNT.

The thermogravimetric analyzer from TA instruments provides a method of testing the temperature programmed oxidation of the species and the specific heat capacity of the carbon samples. The temperature of oxidation shows the bonding strength of the carbons and the peak decomposition shows us further information about the types of carbon species in the sample. This temperature is found by finding the temperature at which the maximum weight loss occurs. A compilation of the TPO data is shown in Figure 56. This test also provides us with a measurement of the unreacted catalyst and other non-carbon residues. This residual number is a very important measurement of purity. The specific heat capacity is a useful test. It is very sensitive and has repeatability and sampling variability.

Spectroscopy

Both Raman and FTIR spectroscopy show promise for quality control of CNT material. Raman spectroscopy clearly shows whether single walled nanotubes are present with the radial breathing modes, RBM, in the low wavelengths. RBM peaks are distinctive to the SWNT because the stretching and contracting of the tube diameter is stifled when there are multiple walls. The peaks at 1580 cm^{-1} and 1330 cm^{-1}, the G and D band, respectively, show the degree to which the carbon rings are attached. This can signify the level of disorder in the CNT which helps determine the amount of damage in the sample. The FTIR data are also instructive, however, establishing a baseline for the FTIR is subjective and can lead to troubles in the analysis. Also the equipment used for the spectra seen in in this work is highly specialized. Other equipment is simpler to operate but required the particles to be in a solution that is not Raman or FTIR active. The bands shown from the pilot plant samples are in the same range as other MWNT in both the Raman and FTIR spectroscopy. However, the Raman bands are also consistent with the graphene peaks. The FTIR peaks show more promise in giving distinctive MWNT peaks. The noise needs to be improved before a standard can be developed. The summary of peaks is shown in Tables 13 and 14.

Developing Tests

The viscosity of a CNT suspension has the potential to give the aspect ratio of the particle. A high ratio of length to diameter is desired for CNT polymer composites. The ratio can be found when the concentration of CNT material causes the viscosity measurement to diverge. This was not seen in this study. The solution's capacity for

holding CNT material in suspension is not high enough to obtain the needed volume fraction. Figure 57 shows the results with the suspension developed in this thesis, while Figure 58 shows an epoxy/CNT suspension which provides the trends that were expected.

Further Work

Although the testing protocols studied in this work show promise in developing standards for quality control of carbon nanotubes, for a complete grading system more testing in needed for a comprehensive assessment. The top priority for further study is obtaining a suspension of carbon nanotubes. This suspension is needed for further viscosity studies that will help determine the aspect ratio of the particles and for better spectroscopy. The surfactant micelles are not formed in high enough concentrations for the viscosity to diverge. Using a nonpolar solvent could lead to more successful dispersion results. There have been successful suspension with similar particles in silicone oil and epoxy resins. [1] [2] These solvent options also are fairly inexpensive which is necessary for large scale industrial production.

The electrical properties of carbon nanotubes were not tested in this work. Often modified to include functional groups around the perimeter of the tubes to enhance dispersion, polymer/nanotube composites are used to add electrical conductivity. [3] Testing the electrical conductivity of the raw powder can be done by loading a cell and monitoring the pressure given to the powder. [4] An image of a suitable device is seen in Figure 59.

Table 12: Summary of density and surface area data.

	Skeletal Density	SA/V
	g/ml	m^2/mL
Rex MWNT	0.84	77.85
Graphene	0.80	19.81
Pet Coke	1.73	1.40
C-001	2.25	
C-002	1.97	56.73
C-003	1.81	90.44
Amorphous C	1.95	
Diamond	3.51	
Graphite	2.27	
SW/DW/MWNT	2.1	

Table 13: Summary of Raman spectra.

Sample	RBM	D Band	G band	G' Band	D' Band	Overtone
Pet Coke		1331	1582	2671		
Graphene		1331	1578	2657		
SW/DWNT	154 (265)	1335	1574	2596 (2655)		
REX MWNT		1339	1571	2677		
C-001		1339	1567	2688	2935	3209
C-002		1339	1587	2674	2912	3193
C-003		1343	1595	2674	2922	3193

Table 14: Summary of FTIR spectra.

C-001	MWNT	SW/DWNT	Graphene	Pet Coke
2332	2334	2334	2351	2330
2361	2359	2367		2359
2857	2872			
2932	2967	2967		2940
2961				
3742	3395	3742	3620	
3852		3852	3688	

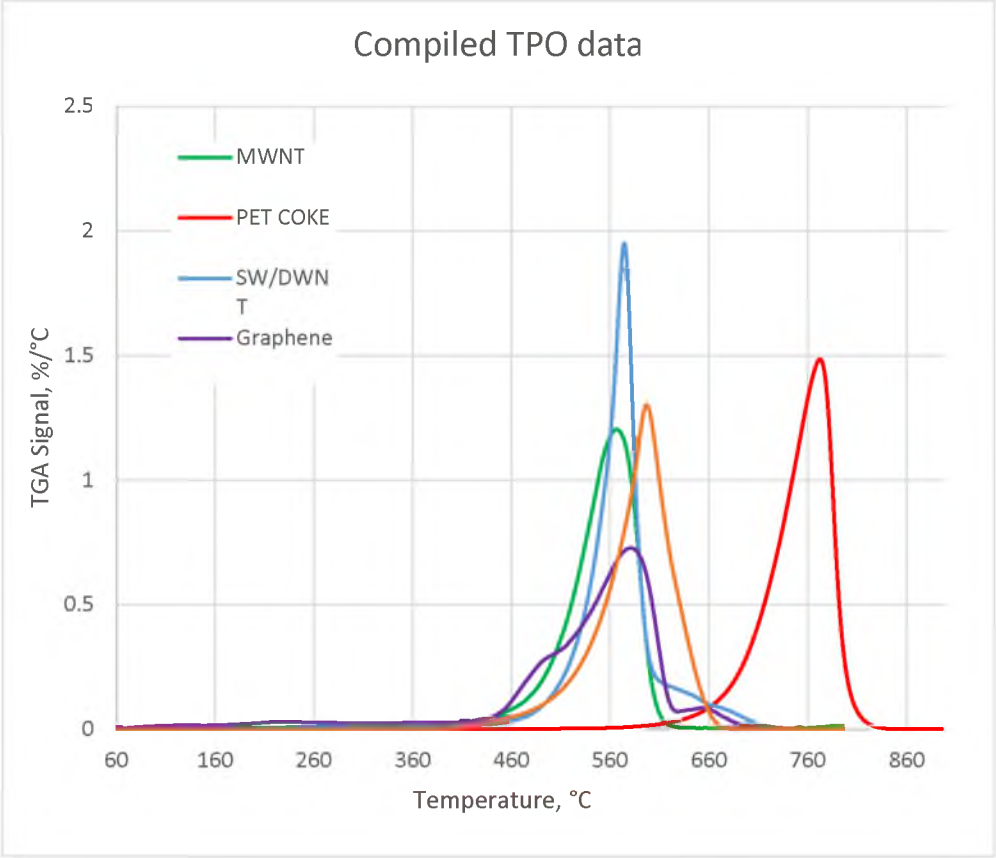

Figure 56: Compilation of TPO data.

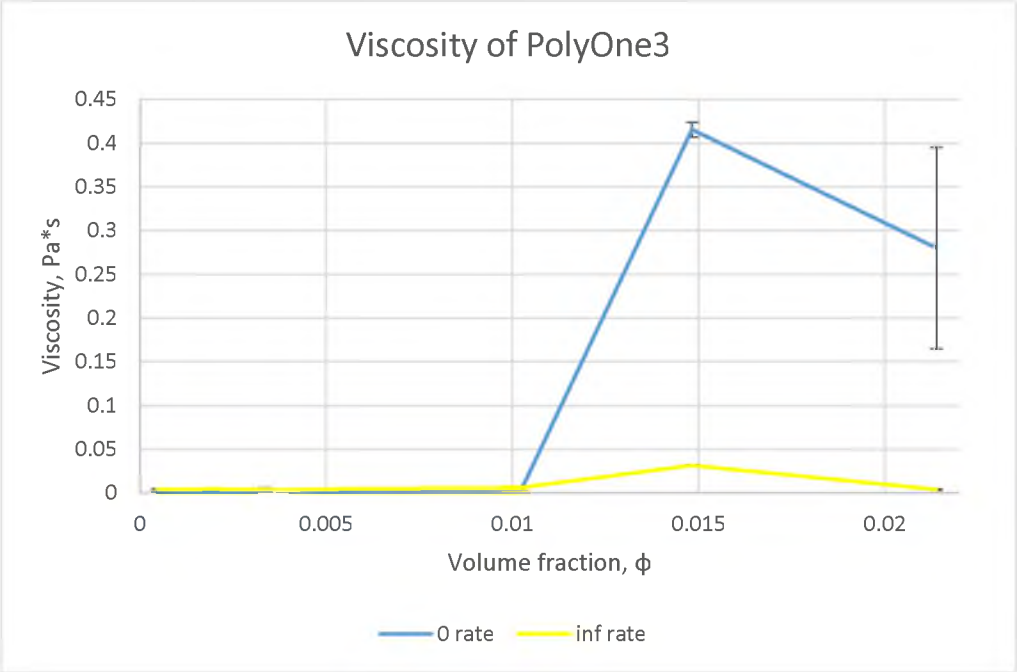

Figure 57: Viscosity as a function of volume fraction.

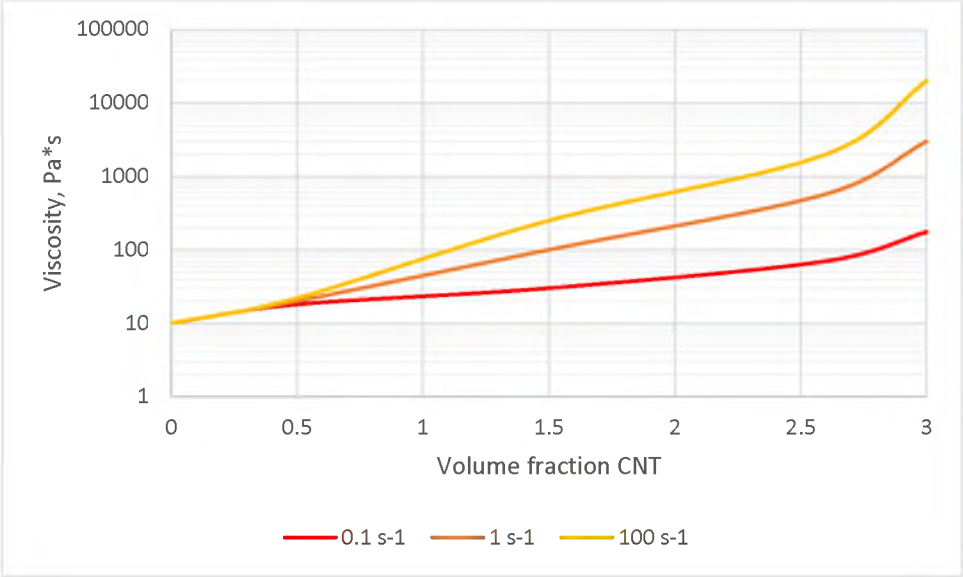

Figure 58: Viscosity versus CNT volume fraction in an epoxy resin. Data from ref. 2.

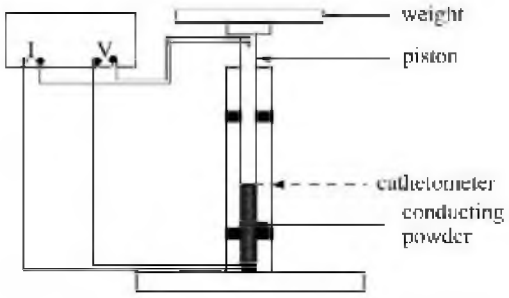

Figure 59: Experimental device for the measurement of the conductivity of moderately compressed powder columns. Modified from ref. 4.

References

[1] M. Kawaguchi, M. Okuno and T. Kato, "Rheological properties of carbon black suspensions in a silicone Oil," *Langmuir,* vol. 17, no. 20, pp. 6041-6044, 2001.

[2] M. Chapartegui, N. Markaide, S. Florez, C. Elizetxea, M. Fernandez and A. Santamaria, "Specific rheological and electrical features of carbon nanotube dispersions in an epoxy matrix," *Composites Science and Technology,* vol. 70, pp. 879-884, 2010.

[3] H. H. So, J. W. Cho and N. G. Sahoo, "Effect of carbon nanotubes on mechanical and electrical properties of polyimide/carbon nanotubes nanocomposites," *European Polymer Journal,* vol. 43, no. 9, pp. 3750-3756, 2007.

[4] A. Celzard, J. F. Mareche, F. Payor and G. Furdin, "Electrical conductivity of carbaceous powders," *Carbon,* vol. 40, pp. 2801-2815, 2002.